Calibration of Active Phased Array Antennas in Constrained Scenarios

ET4300: Master Thesis EE

Muhammad Rizqi

Delft University of Technology

Calibration of Active Phased Array Antennas in Constrained Scenarios

by

Muhammad Rizqi

to obtain the degree of Master of Science

at the Delft University of Technology,

to be defended publicly on Tuesday, August 25, 2026 at 13:00.

Student number:	6147224	
Project duration:	Nov 10, 2025 – August 25, 2026	
Thesis committee:	Yanki Aslan, Ph.D.,	MS3, TU Delft, supervisor
	Prof. Dr. Olexander Yarovyi,	MS3, TU Delft
	Guilherme Theis,	Robin Radar Systems
	Marco Spirito, Ph.D.,	ELCA, TU Delft

Cover:	Illustration of Phased Arrays by Muhammad Rizqi
Style:	TU Delft Report Style, with modifications by Daan Zwaneveld

An electronic version of this thesis is available at `http://repository.tudelft.nl/`.

Acknowledgements

All praise and gratitude be to God for the completion of this thesis project.

It has been two years since I departed for the Netherlands to pursue this academic journey. In that time, I have had the privilege of not only study at a renowned academic institution, but also to live an incredible chapter of my life abroad. And for this very journey, I would like to express my gratitude towards all those who have supported me.

First, I would like to express my gratitude to my supervisors, Yanki Aslan, Ph.D. and Guilherme Theis. Week in, week out, their guidance allowed me to make progress on my work. I would also like to thank Jonas Heylen, who was my daily supervisor for a brief period, for his support in kick-starting this project. The measurements conducted in this report would not have been possible for the helping hand of Pascal Aubry, who I owe a great deal of. I would like to thank Prof. Dr. Olexandr Yarovyi and Marco Spirito, Ph.D. for taking time from their busy schedules to take part on the Thesis Committee. Lastly, I acknowledge the important contribution of Analog Devices and Robin Radar Systems for providing parts needed to conduct the experiments done in this project. This thesis project also recognize the Indonesia Endowment Fund for Education (LPDP), who has funded my master's education through a fully-funded scholarship.

Furthermore, the completion of this thesis project would not have materialized without "the village" I have been graced in my day-to-day life. Dear parents, I would be nowhere without your love and support from the start. Thank you for teaching me honesty, perseverance, and care for others. To my brother Linggar and my sister-in-law Vania, thank you for bringing into life one of my biggest motivations in the form of a new-born niece, Asha, who I cannot wait to meet. I would like to thank my extended family, especially *Enin* and *Mbahti*, for their ever-whispering prayers for their grandchildren. To all my friends who have supported me, back home and in Delft, I thank you.

Muhammad Rizqi
Delft, August 2026

Abstract

The literature on calibration of active phased array antennas (APAAs) lacks a consistent, bias-free framework for evaluating and comparing calibration techniques. Existing approaches typically validate a proposed technique against another calibration method rather than against the ideal array response. To address this, a new set of pattern-derived figures-of-merit is proposed, using the ideal array factor (AF) pattern as ground truth. These metrics, including pattern root mean square error (RMSE), steering angle error, and maximum side lobe level (SLL), provide a direct measure of calibration performance in terms of beamforming quality.

The framework is applied to calibration in constrained scenarios, where full anechoic control of the measurement environment is unavailable, as can occur when APAAs are calibrated after deployment. Three constraints are investigated: finite calibration-angle sampling, reduced measurement signal-to-noise ratio (SNR), and multipath. Three phaseless calibration techniques: rotating electric-field vector (REV), single-channel sequential null steering (SCSNS), and single-channel sequential lobe steering (SCSLS), are evaluated using the CN0566 ADALM-PHASER phased array platform.

Finite calibration-angle sampling produces consistent degradation across all techniques: every $10°$ increase in the difference between calibration and steering angle increases steering angle error by at least $0.3°$ and pattern RMSE by approximately 1.4%, with REV and SCSNS outperforming SCSLS. Below technique-dependent SNR thresholds, calibration fails, while further SNR provides little benefit; the thresholds are -13.45 dB (SCSNS), -10.42 dB (SCSLS), and -8.87 dB (REV).

For echoic environments, two novel echo-aware calibration methods are proposed: frequency-domain averaging (FDA), which isolates the line-of-sight component through solely frequency diversity, and geometry-informed echo de-embedding (GIED), which uses ray-tracing to model and compensate for multipath. Both substantially outperform conventional calibration, which exhibits 2.088 dB and $9.85°$ magnitude/phase calibration error standard deviation under multipath. With fully known scatterer geometry, GIED (0.363 dB, $3.19°$) outperforms the FDA (0.989 dB, $3.36°$). However, FDA demonstrates more robustness to incomplete geometry information.

This work provides the first ground-truth-based framework for comparing APAA calibration techniques under constrained scenarios and the first demonstration of active multipath compensation for calibration in echoic environments.

Keywords: calibration, active phased array antennas, constrained scenario, multipath.

Table of Contents

Nomenclature

Abbreviations

Abbreviation	Expansion	First Mention
AF	array factor	7
AoA	angle-of-arrival	11
APAA	active phased array antenna	1
AUT	antenna-under-test	2
CUT	channel-under-test	4
DNN	deep neural network	5
DUCAT	Delft University Chamber for Antenna Tests	74
DUT	device-under-test	2
EEMCS	Electrical Engineering, Mathematics and Computer Science	73
EIRP	effective isotropic radiated power	1
EM	electromagnetic	1
FDA	frequency-domain averaging	9
FF	far field	2
FT	Fourier transform	39
GIED	geometry-informed echo de-embedding	9
HPBW	half power beam width	21
IF	intermediate frequency	20
IFT	inverse Fourier transform	39
IQ	in-phase and quadrature	10
LoS	line-of-sight	3
LSA	least-square approximation	14
MSE	mean square error	7
NF	near field	4
P&P	park-and-probe	4
PDP	power-delay profile	22
RC	reverberation chamber	5
RCS	radar cross section	38
REV	rotating electric-field vector	5
RF	radio frequency	1
RMSE	root mean square error	7
SCSLS	single-channel sequential lobe steering	10
SCSNS	single-channel sequential null steering	10
SD	standard deviation	7
SDR	software-defined radio	20
SLL	side lobe level	1

Abbreviation	Expansion	First Mention
SNR	signal-to-noise ratio	2
SQP	sequential quadratic programming	47
ULA	uniform linear array	7
VNA	vector network analyzer	8

1

Introduction

1.1. Motivation

In recent decades, active phased array antenna (APAA) has emerged as an integral part of current and next-generation wireless systems. In large part, this is due to their ability to manipulate how it directs radiation dynamically electronically [1]. Through precise control of the magnitude and phase response radiated by each antenna element, APAAs are able to shape the radiation pattern of the overall array.

In practice, precise control of each radio frequency (RF) channel connected to each antenna element is not trivial. While a set of *desired* excitation weights can be analytically drawn up for each channel to ideally produce a specific beam shape, non-ideal effects exists throughout the signal path. These non-ideal effects impact the *true* excitation weights at the antenna elements and distort the resulting radiation pattern [2]. Overall, non-ideal effects can be categorized into static and dynamic effects. Static effects typically emerge from design and manufacturing tolerances. For example, manufacturing tolerances cause unequal losses and propagation delay that affect channel responses. Additionally, many components in the RF path are non-linear devices, e.g. mixers, and amplifiers. While these non-linear behaviors are usually well modeled in the system design, imperfect approximations will still aggregate and manifest. Similarly, unaccounted electromagnetic (EM) interactions, such as mutual coupling or near-field loading with nearby objects, will also have an effect. Furthermore, true excitation weights may also be affected by the dynamic effects of aging and environmental conditions, such as humidity, temperature, vibration, etc. Temperature in particular can cause many problems, both mechanically and electrically [3]. All-in-all, without intentional care, significant distortion in the radiation pattern will occur. On an application level, mobile connection services, satellite communications, military radars, or any other utilization of APAAs would have degraded performance – some with the possibility of complete failure.

Within the context of APAAs, calibration refers to the effort to compensate for those non-ideal effects, thereby approximating the initially intended beam shape. While it has been demonstrated that it is possible to design an APAA which yields acceptable non-complex beamforming results without any calibration in [4], authors in [5] has shown that proceeding with calibration will still obtain non-negligible results, whether in effective isotropic radiated power (EIRP) or side lobe level (SLL). To this end, the optimal calibration process would account and compensate for all non-ideal effects. However, in practice, these effects are often unique for each specific scenario. Changing a single parameter will change how the non-ideal effect behaves:

different frequencies; different excitations/beam shapes; different ambient temperatures; etc. In fact, study [5] demonstrated significant gain-phase coupling in their device-under-test (DUT) to emphasize this – that is to say that changes in the magnitude and phase setting will also cause changes in the phase and magnitude responses. The same study also found considerable frequency dependency of the RF channel response. Naturally, compensating for each and every scenario is impossible, since that would require characterization of the APAA for each scenario. A single RF channel alone can have multiple thousands of excitation weight settings. So, instead of trying to account for countless number of different scenarios, calibration is typically done only for only a set of scenarios-of-interest. For example, calibrations are done only for a handful of intentionally selected frequencies, for beam shapes or excitations of interest, at standard ambient temperature, etc.

To obtain accurate and precise results, any measurement should be done in a controlled environment. Measurements for the purpose of calibration are not different. Ideally, it is done in an anechoic environment with strict requirements: with ample signal-to-noise ratio (SNR), with correct antenna-under-test (AUT)-probe distances and orientations, in a specified ambient temperature, etc. In doing so, the variance of the measurement is reduced, resulting in accurate and precise calibration results. However, facilitating such rigorous measurement is not always possible. Often, these APAAs need to be calibrated after they have been deployed. While static, non-ideal effects can be compensated through calibration as they are rolled out of the manufacturing plant, dynamic effects will build up over time. However, anechoic chambers are expensive to build, so there is only a limited number of them. Measurement facilities might be inaccessible, e.g. far or isolated from the APAA system's location. There might be queues, also preventing access. Furthermore, if the electrical or physical size of the APAA is too large, far field (FF)-based calibration methods will not fit inside existing anechoic chambers. As such, calibration in scenarios where the amount of environment control is constrained, *constrained scenarios*, becomes an interesting possibility.

Moreover, as shall be seen in the following sections, the literature on calibration techniques are plenty. Despite this, the literature disagrees on how a fair comparison between different techniques be made. In fact, the literature tend to focus only on how their proposed technique fair against an existing/conventional technique, rather than providing a fair comparison of techniques. In doing so, these techniques, which should act only as a kind of "gold standard", are then mistakenly applied as "ground truths". This, in turn, misinform the selection of metrics.

This work aim to tackle multiple problems in the same swoop. Not only are multiple calibration techniques are being compared, these comparisons are made in different practical, constrained scenarios. Importantly, a suitable set of metrics are chosen to make these comparisons. Based on the resulting measurements, insights on the viability of calibration under different constrained scenarios can be concluded. Furthermore, the possibility of compensating for one of the environmental constraint is of considerable interest, namely the presence of echo or scattered paths. Such a possibility would suggest that calibration done in an echoic environment would have similar performance to that done in a controlled environment. In that case, calibration processes that are traditionally done inside of anechoic chambers can now be done elsewhere. From an industrial perspective, circumventing the reliance on anechoic chambers eliminates a significant bottleneck of the production pipeline, since it provides a scalable, cost-effective alternative. Moreover, the spatial limitations of large APAA measurements in conventional test chambers can also be avoided. In conclusion, research in this topic can have wide ranging implications.

1.2. Problem formulation

Calibration in any non-controlled environment is unpredictable. Not only because the environment itself is affecting the measurement process, but also because it is not a particularly well documented in an academic sense. The following list outlines three overarching problems recognized with regard to calibration in constrained scenarios.

1. To the author's knowledge, no literature have focused in proposing an approach to evaluate calibration performance within the context of making a fair comparison between different calibrations. In this respect, two things must be redefined. First, a new reference point of comparison, i.e. the ground truth, needs to be pointed out. Secondly, suitable performance metrics need to be formulated. While APAA calibration has existed for many years as a field of research, the typical metrics for quantifying the calibration performance have not evolved accordingly. New metrics must account for the modern emphasis of APAA's capability for beamforming, which are highly adaptable. A more comprehensive explanation on this is presented in Subsection 1.4.2. When both things are well defined, then fair comparison between two calibration, whether done in controlled or constrained scenarios, can be made;
2. Until now, the feasibility of calibration in constrained scenarios – without additional treatment – are unknown. Experiments need to be done to provide suggestion on the feasibility of each scenario. Namely, three constraints will be considered separately in this work: finite sampling of calibration angle; decreased measurement SNR; the presence of echo.
   - When utilizing phaseless calibration techniques, further discussed in Section 1.4 and 2.1, it is recommended to calibrate for each steering angle. Due to time or space constraints, the calibration angles will only be a finite subset of all possible steering angles. With increasingly sparse sampling, calibration performance are traded-off for calibration speed/number of measurements needed.;
   - Outside of a controlled environment, there is the possibility of decreased calibration SNR, whether due to the presence of interferers, increased equivalent antenna temperature, or limited signal power. Naturally, this decrease will have an impact on calibration performance;
   - Through the use of RF absorbers and strict control of the measurement setup, measurements in anechoic chambers allow the assumption of only a single signal path between the reference device and the APAA. However, such assumption cannot be made when calibration is done outside of anechoic chambers where significant scattered paths exist. Signals propagating through different paths, including line-of-sight (LoS) and scattered paths, will arrive at the antenna elements and combine as a vector sum. Without any additional treatment, the scattered path signal component will interfere with the intended LoS component and cause the calibration performance to deteriorate.
3. To the knowledge of the author, no echo-aware calibration techniques have been described in the literature. Echo-aware calibration refers to calibration techniques which is designed to intentionally compensate for multipath effects present in echoic environments.

1.3. Thesis objectives

Considering the problems presented in Section 1.2, a number of objectives can be derived.

1. Derive new metrics to quantify calibration performance, emphasizing their compatibility with the adaptive nature of beamforming;
2. Propose an empirical approach to manage the trade-off between finite sampling of calibration angles;
3. Compare and motivate the selection of the best phaseless technique under SNR constraints;

4. Propose methods to achieve echo-aware calibration, complete with analytical and experimental supporting arguments.

1.4. Literature study

1.4.1. Overview of Calibration Techniques

The literature regarding the calibration of APAAs is vast. Here, some of it has been summarized. Conventionally, calibration is done through complex measurements – meaning both amplitude and phase responses are directly measured. The park-and-probe (P&P) method utilizes precise mechanical movement of a *probing* antenna to *park* it in precise locations in reference to the antenna elements, usually in the near field (NF), achieving identical coupling response for each channel-under-test (CUT) measurement. Complex measurements of each CUT's channel response is then made sequentially, with only one channel active at a time. Studies [5], [6] augments the P&P method with intelligent strategies to achieve calibration of the APAA. While study [6] describes a heuristic approach to quickly arrive at a set of calibration weights the P&P method, study [5] proposes the use of sampling and interpolation techniques to completely characterize each RF channel. Such an approach introduces interpolation error, although it allows derivation of calibration weights for any possible desired excitation weight, providing excellent flexibility. The major drawback of the P&P method is how only a single channel is active during the calibration process. Such methods are referred to as the "on-off" calibration methods. These calibration methods are disadvantaged because they do not represent a realistic application of APAA, which are generally used with all elements active, in other words, "all-on". In contrast to P&P and other on-off methods, all-on calibration methods better emulate working conditions of APAAs, such as temperature gradients and voltage drops across the array, as well as various associated EM behavior, such as mutual coupling between channels and antenna elements.

Study [7] proposes the use Fourier techniques to project precise NF measurements of the APAA in all-on mode to the array plane. In doing so, the true excitation weights delivered at each antenna element can be inferred. Through an iterative process, calibration is then achieved by modifying the excitation weights until the desired excitation weights are inferred from the back-projection. The result is a set of calibration weights highly optimized for a set of beam shapes. Since this method also utilizes NF measurements, it will not be constrained by lack of space which is often associated with FF measurements. Conversely, calibration methods which is done through NF measurements are highly prone the probe itself imparting some distortion to the measured EM fields. Additionally, NF measurements are also highly sensitive to any mechanical positioning error of the probe.

Another approach proposes utilizing the predictable nature of mutual-coupling, particularly symmetrical mutual-coupling effects, to achieve calibration [8]–[10]. In combination with built-in probing functionality on the array plane, this approach practically allows calibration anywhere without any additional measurement equipments. This is a major advantage when considering systems that are highly susceptible to dynamic effects, therefore needing regular calibration to keep beamforming performance up. The major drawback of the mutual-coupling approach is its architecture complexity requirements, necessitating additional calibration-dedicated components on an already tightly integrated APAA hardware. Additionally, these methods would fall under the on-off calibration methods, since mutual coupling measurements are done sequentially.

Through clever manipulation of phase shifts at each RF channel, it has been shown that all-on mode calibration can be achieved. These methods can generally be grouped into two categories based on the measurement technique used. Studies [11]–[16] rely on complex measurements, while studies [17]–[27] do not require any phase information to achieve calibration. Although complex measurement-based methods are generally more efficient in terms of the number of measurements needed, direct measurement of the phase response introduce added complexity to the measurement setup. This is due to the need to have phase coherence between the probe and the DUT on top of having carrier frequency lock. On the other hand, phaseless techniques, sometimes also referred to as amplitude-only or power-based techniques, eliminate this added complexity.

By implementing orthogonal codes in the form of phase shifts, the authors in [11] showed that simultaneous calibration of all APAA channels can be achieved. An improvement was introduced in [12], which proposed additional characterization of phase shifter errors to de-embed them from the calibration through post-coding. Significant improvements were achieved in [13], which organizes the calibration problem into a set of linear equations. An optimum coefficient matrix, which dictates the RF channel phase shifts needed for measurements, is then used to solve the linear equations and arrive at the calibration weights. The authors in [14] add a single measurement needed to resolve accumulated error found in [13], adding a single additional measurement needed to achieve calibration from N to $N+1$, where N is the number of channels in the APAA. In [15], the use of multiple probes is proposed to further increase the measurement efficiency. Meanwhile, authors in [16] focus on cases whereby the APAA is operating in beam-steering mode only.

Similarly, phaseless calibration methods have seen improvements. The work in [17] is the primary reference of phaseless calibration techniques. It describes the rotating electric-field vector (REV) technique, whereby the APAA is in all-on mode with a single CUT has its phase rotated over 360°. Meanwhile, by evaluating the resulting curvature of the measured vector sum of the array power, dubbed the "REV" curve, the calibration weight of the CUT can be solved. The major drawback of the REV technique is its measurement efficiency. A large number of measurements, once for each phase shift increment, is needed to characterize and calibrate for a single channel. The authors in [18] argue that only four orthogonal phase settings are needed to obtain calibration weights for each channel: 0°, 90°, 180°, and 270°. Meanwhile, in [19] further argued that only three phase settings are needed to achieve calibration, 0°, 90°, 180°. The work in [20] posit the 180° phase setting measurement can instead be replaced by turning off the channel instead. Overall, the measurement efficiency was increased by decreasing the number of measurements needed to achieve calibration from $N(2^p - 1) + 1$ where p is the phase shifter bit-number [17], to $3N + 1$ [18], to $2N + 1$ [19], [20]. Also to increase efficiency, [21] proposes the rotation of phase shifts of multiple CUTs at the same time by utilizing Fourier techniques. It achieved some gain in efficiency, but at the cost of additional calibration error. Authors in [22] propose improvements in another way, whereby additional information on phase shifter behavior is utilized to enable calibration for each and every phase shifter setting. Previously, calibration weights were only provided for each channel, not for *every* phase shifter setting of each channel. Meanwhile, [23] proposes a method to solve the solution ambiguity for the conventional REV technique by recording an additional REV curve. Lastly, to improve on the conventional REV's performance for APAA with large number of elements a multitude of references are available. For example, [24], [25] propose splitting up the array into groups and REV calibration is done in groups. In doing so, larger fluctuations in the REV curve can be observed, yielding better results especially in higher SNR situations. Meanwhile, [26] introduces the use of deep neural network (DNN) to obtain calibration weights from phaseless measurements. It is demonstrated that this method is more robust than conventional REV in low SNR. Lastly, authors in [27] were able to isolate the signal contribution of the CUT from signals from other channels in the frequency domain through time-delay modulation. In doing so, the calibration performance is no longer directly affected by the size of the array. By evaluating the power level of harmonics appearing in the spectrum, calibration of the CUTs can be achieved.

More recently, the reverberation chamber (RC) has also appeared as an interesting prospect for APAA calibration, especially due to its compact form factor. Study [28] has provided a proof-of-concept of this approach, although it is currently limited to the circular antenna array case for now.

Table 1.1: Overview of calibration techniques mentioned. Key features are presented: utilizes NF/FF measurements; requires complex/phaseless information; categorized as all-on/on-off methods. Key advantages and limitations are also shown.

Lit.	Feature			Advantage	Limitation
	NF/FF	Complex/ Phaseless	All-on/ On-off		
[5], [6]	NF	Complex	On-off	Quickens P&P procedure.	Adds uncertainty to calibration.
[7]	NF	Complex	All-on	Maximizes beamforming control.	Require high precision excitation control and high resolution NF measurements.
[8]–[10]	Mutual coupling	Complex	On-off	No external instruments needed.	Array edge-effects; require dedicated supporting hardware architecture.
[11]–[16]	FF	Complex	All-on	Increasingly efficient in terms of num. of measurements needed.	Requires phase information.
[17]	FF	Phaseless	All-on	First to propose calibration without phase.	Extremely inefficient.
[18]–[20]	FF	Phaseless	All-on	No phase information needed, increasingly efficienct.	Sensitive to noise in large arrays.
[21]	FF	Phaseless	All-on	Small increase in measurement efficiency.	Linear increase in measurement error.
[22]	FF	Phaseless	All-on	Provides calibration for all phase settings.	Sensitive to noise in large arrays.
[23]	FF	Phaseless	All-on	Allows de-ambiguation of REV solutions.	Increased number of measurements needed.
[24]–[26]	FF	Phaseless	All-on	Better performance in larger arrays	Increased number of measurements needed.
[27]	FF	Phaseless	All-on	Better performance in larger arrays	Requires fast switching response times on the phase shifters.
[28]	Reverb. chamber	Phaseless	On-off	Avoids need for anechoic chambers.	Is only proof-of-concept with highly specific DUT.

1.4.2. Relevance on Formulated Problems and Gaps in the Literature

Recalling the problems formulated in Section 1.2, here, the existing literature is reevaluated. First, how the literature deals with evaluating calibration performance shall be discussed. Based on what metrics are used to evaluate their proposed calibration technique, the literature on APAA calibration can be organized into several categories, shown in Table 1.3. As can be seen from the table, a large portion of the literature utilizes statistical descriptions of the calibration weight error, whether it be in terms of maximum span, standard deviation (SD), root mean square error (RMSE), mean square error (MSE), or mean. Similarly, literature on APAA calibration can be organized based on what that comparison reference is. This categorization is presented in Table 1.2. By observing both tables, it can be seen that, the literature evaluates calibration performance largely by assessing how little their proposed calibration technique differs to an existing calibration technique. The line of thinking is as follows: if the proposed technique yields similar results to an existing, widely accepted technique – the "gold standard" – then the proposed technique must be valid. Of course, this is a perfectly reasonable rationale when the literature is simply arguing for the validity of the proposed technique.

On the other hand, with the focus on proving the validity of the proposed technique, the literature have provided little guidance on how to go about making a fair comparison between calibrations. Although intuitive, the "gold standard" line of thinking should not be extended to the evaluation of calibration performance in this context. Doing so risks favoring techniques most closely resembling the "gold standard". Instead, assessment reference should ideally be based on the "ground truth". In the calibration context, the ground truth would correspond to "perfect calibration". However, it is impossible to measure the ideal calibration weights – it is the exact purpose of this field of study. On the other hand, the *outcome* of ideal calibration *is* known. In phased array theory, it is known as the the array factor (AF) pattern, which represents the ideal pattern given the excitation of an array. Therefore, this work proposes that the ideal/AF pattern be used as the comparison reference when assessing and comparing between APAA calibration performance. In any case, using AF pattern to derive metrics is advantageous, especially in terms of contextualizing calibration performance. It would not be directly obvious to an antenna or a wireless engineer what statistical description of calibration weights error would constitute acceptable calibration performance. On the other hand, when calibration metrics are pattern-derived, such as beam shape, or SLL, these descriptions are instantly actionable.

Another observation on the existing literature can be made with regards to the exact scenario the calibrations are performed. Table 1.4 summarizes the categorization of calibration scenarios found in the literature. It is shown that, by and large, calibration performance in the literature is described in ideally controlled environments. In fact, a number of references has no mention of the calibration scenario, owing the automatic assumption of calibration restricted to controlled environments. Meanwhile, only a handful of studies consider constrained scenarios. The fact that calibration in constrained scenarios is hardly considered in the literature constitutes a literature gap, especially when considering the advantages of such possibility. As such, this work aims to have calibration in constrained scenarios among the center of its focus.

1.5. Thesis scope and approach

In this work, calibration of APAAs in constrained scenarios are considered. To be more specific, only calibration techniques applicable to analog phased array architures shall be evaluated. This is because they represent the vast majority of existing APAAs. Also, analog phased array architectures are generally more constrained, meaning they can more easily be adapted for calibration of digital phased array architectures. Moreover, analysis shall be limited to only APAAs on receive-mode with uniform linear array (ULA) architectures. This is done simplify and tailor the overall analysis to the designated DUT, further described in

Table 1.2: Summary of comparison reference used in the literature when assessing performance of calibration techniques.

Literature	Comparison Reference
[16], [22], [25]–[27]	Conventional REV.
[5], [7]–[10], [12], [17], [20]–[22], [27]	P&P or similar.
[11], [14], [15], [18], [20], [23], [25]–[27]	Any other calibration technique besides REV or P&P.
[13], [19], [28]	Cable-based vector network analyzer (VNA) measurements.
[13], [20], [24]	Applied true excitation in simulation.
[5], [6], [11], [23], [24], [27]	Radiation pattern without calibration.
[9]–[11], [13], [23]	Ideal pattern or AF.

Table 1.3: Summary of metrics used in the literature when assessing performance of calibration techniques.

Literature	Metrics Used
[13]–[16], [19], [25], [27]	Maximum error of calibration weights.
[5], [8]–[14], [18]–[24], [26]–[28]	SD, RMSE, or MSE, or mean error of calibration weights.
[11], [13], [15], [16], [23], [24], [27]	Visual evaluation of the calibrated radiation pattern (without quantitative evaluation).
[6], [7], [10], [17]	Evaluation of the calibrated radiation pattern, e.g. SLL, etc.

Table 1.4: Summary of calibration scenarios found in the literature.

Literature	Calibration Scenario
[5]–[8], [12], [14], [15], [23]–[25]	Measured in an anechoic facility.
[11], [13], [16], [19]	Measurements with use of RF absorbers, but generally not considered nominally anechoic.
[8]–[10]	Measurement *in situ*, in the field.
[17], [18], [20]–[22]	Measurement scenario not mentioned.
[28]	Measured in a RC.
[20], [26], [27]	Simulated for varied SNR.

Section 2.3.

Three constrained scenarios in reference to calibration are assessed: finite sampling of calibration angles, decreased SNR, and the presence of echo. In the evaluation of these scenarios, calibration performances are evaluated through pattern-derived metrics, further elaborated in Subsection 3.1.2. In this process, due to time constraints, evaluation are limited to only steered beam patterns. At first, a purely experiment based approach is employed. Measurements are done to evaluate the effect of these constrained scenarios in calibration performance. From the results, observations and inference is made. Specifically for the calibration in echoic environment case, methods to achieve echo-aware calibration are also proposed. Here, the echoic environment is assumed to be static. To this end, the multipath problem of echoic environments are described analytically. Furthermore, the multipath problem is modeled through MATLAB. There, a ray-tracing-based simulation is built, which is then used to evaluate different approaches to echo-aware calibration. If an approach shows signs of success in compensating for the multipath effects, proof-of-concept experiments are done to validate the simulated results.

1.6. Novelties of this research

In this thesis project, the following aspects is novel.

1. First time comparison of multiple calibration techniques through comprehensive pattern-derived quantitative metrics;
2. Quantification of the effect of finite calibration angle and decreased SNR to APAA calibration performance;
3. Novel development of two different methods to achieve echo-aware calibration: the frequency-domain averaging (FDA) and geometry-informed echo de-embedding (GIED).

1.7. Thesis outline

The structure of this thesis report is as follows. Chapter 2 describes the algorithm followed by the phaseless techniques applied in this work. Additionally, the DUT and instruments used in this work will be described. In Chapter 3, the calibration performance of different phaseless calibration techniques are compared under different constrained scenarios. In Chapter 4, further discussion is presented on the problem of calibration in echoic environments. There, analytical description is provided and two methods are proposed to be able to compensate for the multipath effects. Lastly, in Chapter 5, conclusions are gathered from the content of this work and recommendations for future work are provided.

2

Calibration algorithms and measurement instruments

As discussed in Section 1.1, non-ideal effects found throughout the signal path will cause errors in the excitation of the antenna array. These non-ideal effects can be lumped into a column vector with N elements, the excitation error $\mathbf{w}_{\text{err}}$, with N being the number of channels in the array. This term represents the complex coefficient that causes the actual excitation of the n-th antenna element, $\mathbf{w}_{\text{true}}$, to deviate from the intended excitation weight, $\mathbf{w}_{\text{exc}}$. To compensate for the aforementioned error, an additional calibration weight, $\mathbf{w}_{\text{cal}}$, is applied. Ideally, this calibration weight should be the exact inverse of the excitation error. The mathematical notations of these variables are shown in Equations 2.1 - 2.4.

$$\mathbf{w}_{\text{true}} = \mathbf{w}_{\text{err}} \odot \mathbf{w}_{\text{exc}} \tag{2.1}$$

$$w_{\text{err},n} = A_{\text{err},n} e^{j\Phi_{\text{err},n}}, \quad n = 1, 2, \ldots, N \tag{2.2}$$

$$\mathbf{w}_{\text{cal}}\big|_{\text{ideal}} = \mathbf{w}_{\text{err}}^{\circ -1} \tag{2.3}$$

$$\mathbf{w}_{\text{true}}\big|_{\text{calibrated}} = \mathbf{w}_{\text{err}} \odot \mathbf{w}_{\text{cal}} \odot \mathbf{w}_{\text{exc}} \approx \mathbf{w}_{\text{exc}} \tag{2.4}$$

In this thesis project, only phaseless calibration techniques are considered. This is due to their advantage of low complexity, which aligns well with the theme of calibration in constrained scenarios. These techniques, which rely only on the measurement of the signal's magnitude or power, do not require the complex system requirements needed to facilitate direct phase measurements. In contrast, phaseless measurement requirements are very lenient. No phase coherency nor frequency lock is needed. It only requires that the frequency of the signal is within the bandwidth of the signal detector. Moreover, since no phase information is required, simple power detectors can be used to make measurements instead of the more complex in-phase and quadrature (IQ) receivers.

Although many different phaseless techniques exist, in this thesis project, only three are used throughout: REV, single-channel sequential null steering (SCSNS), and single-channel sequential lobe steering (SCSLS) techniques. The REV represents the conventional phaseless calibration technique. Meanwhile, the SCSNS is the default calibration technique implemented by Analog Devices as the provider of the DUT. Lastly, the SCSLS is implemented through a straightforward tweak in the the SCSNS algorithm. In this chapter, they will be described in detail.

2.1. Phaseless techniques

The typical measurement setup involving phaseless techniques can be observed in Figure 2.1. In the figure, naturally, DUT refers to the APAA being measured and calibrated. Meanwhile, the reference device is the device used to complete the transmit-receive scenario of the measurement setup. If the DUT is a transmit-mode APAA, then the reference device is a probe, i.e. receiver/detector. Conversely, if the DUT is a receive-mode APAA, the reference device is a beacon, i.e. transmitter. Since only the calibration receive-mode APAA is considered in this thesis project, the reference device shall henceforth be referred to as the calibration beacon, or simply beacon.

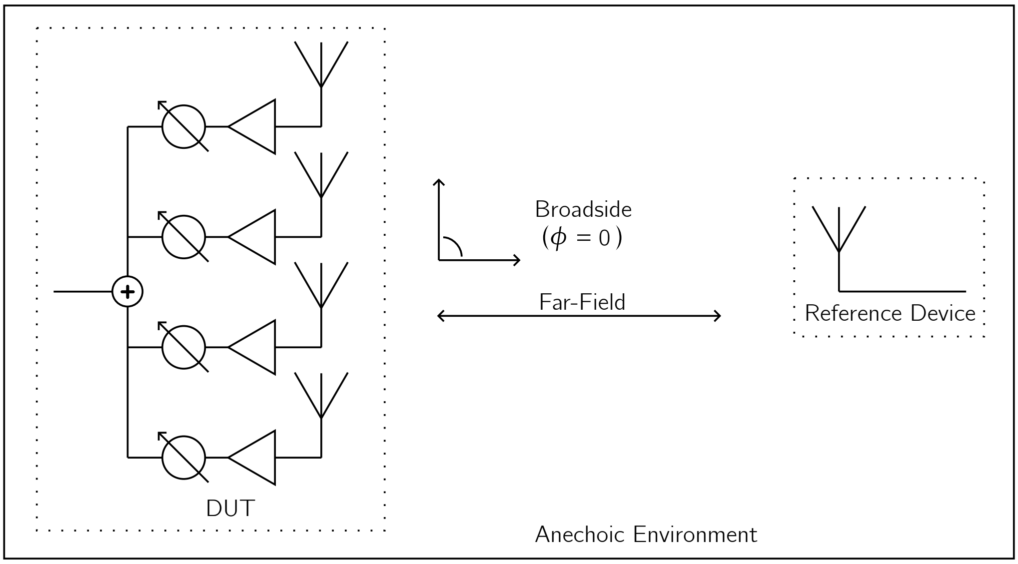

Figure 2.1: A typical calibration setup using phaseless technique.

From the measurement setup shown in Figure 2.1, the wireless channel behaviour can be easily derived. The anechoic setup ensures that only the LoS signal path will arrive at the array aperture. Since the calibration beacon and the DUT are assumed to be in FF distance of each other, it can be assumed that the there is negligible difference in both the amplitude attenuation and the angle-of-arrival (AoA) of the signals arriving at each antenna elements. In principle, this is the plane wave approximation. This assumption, in combination with the position of the beacon in the broadside of the array aperture, means no phase offset shall exist among the signals arriving at each antenna element. In effect, the propagation response for each channel is identical and is simply the free-space propagation response.

These assumptions are formalized in Equation 2.5, where the complex response vector for all N channels $\mathbf{h}_{\text{propagation}}$ is defined as a uniform vector with its components equal to the free-space propagation response h_{fs}. Following standard free-space propagation theory, h_{fs} is defined in Equation 2.6, where r, c, and f respectively denotes the distance, speed of light, and signal wavelength. The exact value of h_{fs} is not typically known, although it must be identical for all channels.

$$\mathbf{h}_{\text{propagation}} = h_{\text{fs}} \mathbf{1}_N \tag{2.5}$$

$$h_{\text{fs}} = \frac{c}{f} \frac{1}{4\pi r} e^{-\mathrm{j}\frac{2\pi f r}{c}} \tag{2.6}$$

With the assumptions made, derivation of the calibration weights can be done more easily. The field vector present on the n-th channel is the product of the signal radiated by the beacon, propagation channel, and excitation error, shown in Equation 2.7. However, since the radiated signal and the propagation channel response is identical for all channels, their effects can be easily normalized out of relevance. As such, any discrepancies between the measured field vector of different channels can be attributed only to excitation errors.

$$\begin{aligned} \mathbf{E} &= s_{\text{tx}}(\mathbf{h}_{\text{propagation}} \odot \mathbf{w}_{\text{err}}) \\ &= s_{\text{tx}} h_{\text{fs}} \mathbf{w}_{\text{err}} \end{aligned} \tag{2.7}$$

2.1.1. REV technique

In the conventional REV technique, the composite field vector of all channels of the array is evaluated. As depicted in Figure 2.2, it can be observed that the composite field vector is the superposition of field vectors of all channels. Moreover, when the field vector of the n-th element is phase shifted, then the composite field vector will rotate in a circle referred to as the REV circle. With the phase shifted over 360°, the REV technique solves the excitation error of the n-th channel by recording the amplitude variation of the composite vector. Since the REV technique is already well described in the literature [17], the step-by-step derivation of the solution will not be shown here. However, relevant details on the procedure and modifications shall be provided. Overall, the flow diagram of the REV technique can be seen in Figure 2.3.

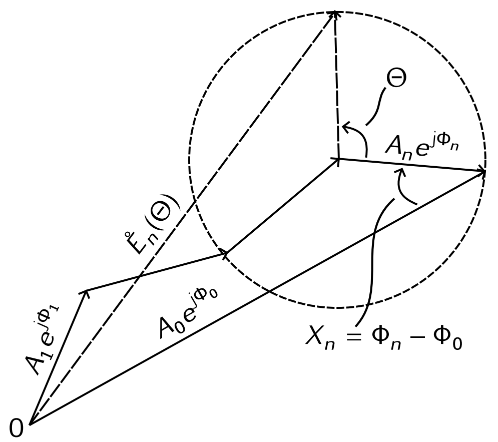

Figure 2.2: Illustration of the composite field vector and the REV circle. Redrawn from [17].

In Figure 2.2, A_0 and Φ_0 denotes the magnitude and phase of the composite field vector in the initial state. Meanwhile, A_n and Φ_n denotes the magnitude and phase of the n-th channel's field vector. As the n-th channel has its phase shifted, the composite field vector can be formulated as follows, with Θ denoting the applied phase shift.

$$\begin{aligned} \mathring{E}_n(\Theta) &= E_0 - E_n + E_n e^{j\Theta} \\ &= A_0 e^{j\Phi_0} - A_n e^{j\Phi_n} + A_n e^{j(\Phi_n + \Theta)} \end{aligned} \tag{2.8}$$

In conventional REV notation, k_n and X_n are introduced as the relative magnitude and phase of the n-th channel's field vector to that of the composite field vector.

$$k_n = \frac{A_n}{A_0} \tag{2.9}$$

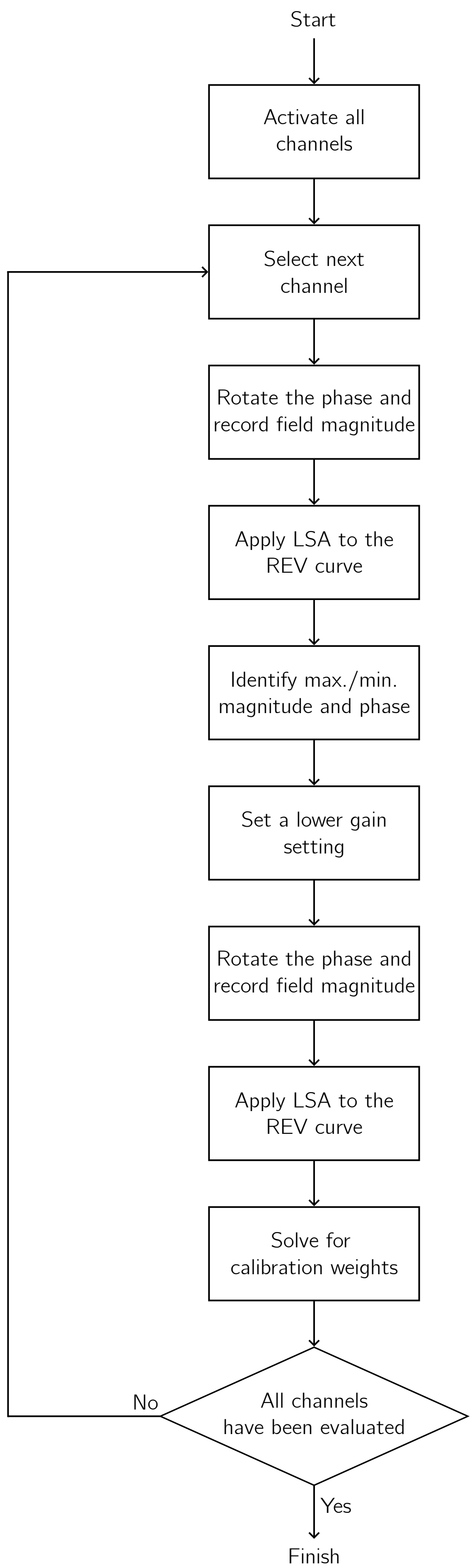

Figure 2.3: Flow diagram of the REV technique. Additional steps proposed by [23] are added to solve ambiguity of solutions.

$$X_n = \Phi_n - \Phi_0 \tag{2.10}$$

Since these values are defined normalized to the static terms, A_0 and Φ_0, then these values must be proportional to the excitation error defined previously.

$$k_n e^{jX_n} \propto E_n \propto w_{\text{err},n} \tag{2.11}$$

While the composite vector field $\mathring{E}_n(\Theta)$ contain both magnitude and phase components, the REV is a phaseless technique and relies only on magnitude – equivalently, power – information to obtain the solution to k_n and X_n. As the n-th channel is phase shifted, the composite field power is measured to produce the REV curve, described in Equations 2.12 and illustrated in Figure 2.4. Ideally, the REV curve will take a sinusoidal shape, as can be identified in the last term of the equation

$$Q_n(\Theta) \propto |\mathring{E}_n(\Theta)|^2 = (A_0 e^{j\Phi_0} - A_n e^{j\Phi_n})^2 + A_n^2 + 2(A_0 e^{j\Phi_0} - A_n e^{j\Phi_n}) A_n \cos(\Phi_n + \Theta) \tag{2.12}$$

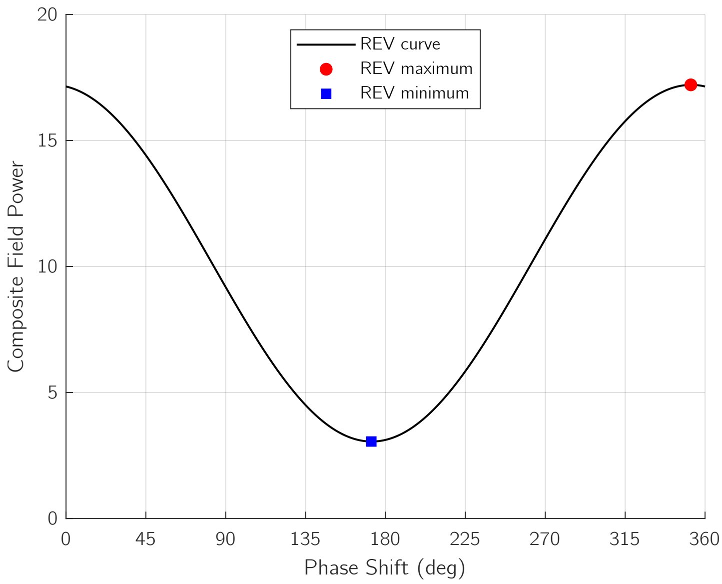

Figure 2.4: Illustration of a REV curve. Here, $Q_{\text{max},n}$, $Q_{\text{min},n}$, and Θ_0 are 17.2, 3.05, and -172°.

That being said, in practice, the REV curve will be subject to distortions, whether it be due to component nonlinearity, mutual coupling, or noise. In the conventional REV literature, it is proposed to use least-square approximation (LSA) to approximate the measured curves in order to recover the best sinusoidal fit. From the fitted REV curve, two important informations are retrieved: the ratio of its maximum and minimum, $r = Q_{\text{max},n}/Q_{\text{min},n}$, and the phase shift associated with the curve's maximum, $-\Theta_0$. These values are key to deriving the calibration weights.

Based on REV literature, it is known the solution to k_n and X_n is ambiguous due to the two possible scenarios given a REV curve, shown in 2.5. In the case of the origin point being outside of the REV circle, the solutions to k_n and X_n are presented in Equations 2.13 and 2.14. On the other hand, if the origin is contained within the REV circle, then the solutions are defined in Equations 2.15 and 2.16.

$$k_n = \frac{\Gamma}{\sqrt{1 + 2\Gamma \cos\Theta_0 + \Gamma^2}} \tag{2.13}$$

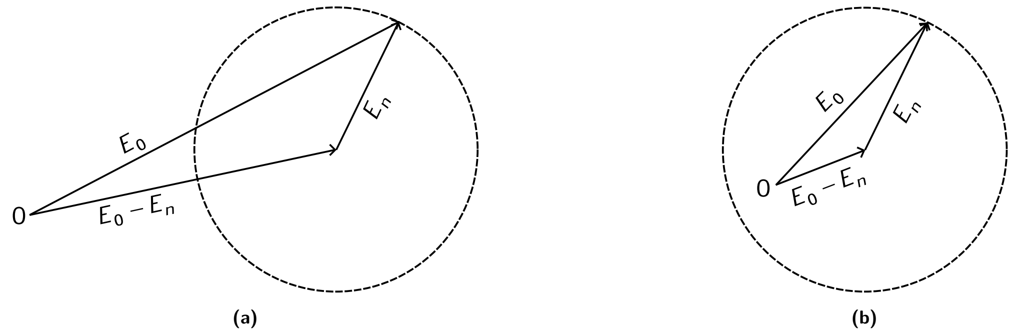

Figure 2.5: Illustration of the two ambiguous cases of REV measurement: (a) origin outside and (b) inside the REV circle.

$$X_n = \tan^{-1}\left(\frac{\sin\Theta_0}{\cos\Theta_0 + \Gamma}\right) \tag{2.14}$$

$$k_n = \frac{1}{\sqrt{1 + 2\Gamma\cos\Theta_0 + \Gamma^2}} \tag{2.15}$$

$$X_n = \tan^{-1}\left(\frac{\sin\Theta_0}{\cos\Theta_0 + 1/\Gamma}\right) \tag{2.16}$$

$$\Gamma = \frac{r-1}{r+1} \tag{2.17}$$

In order to solve the ambiguity of the REV solution, the method proposed in [23] is applied. In principle, this method proposes the generation of an additional REV circle. Specifically, the magnitude of the n-th channel is attenuated prior to the application of phase shifts and composite field power measurements. The resulting new REV circle can be observed in Figure 2.6. By observing whether the measured minimum field magnitude $\Delta|\mathring{E}_{\mathrm{min}}|$ increases or decreases, the correct solution of the REV technique can be chosen. In reality, only the composite field power is measured in this process. In Figure 2.7, an example of the measured REV curves are shown.

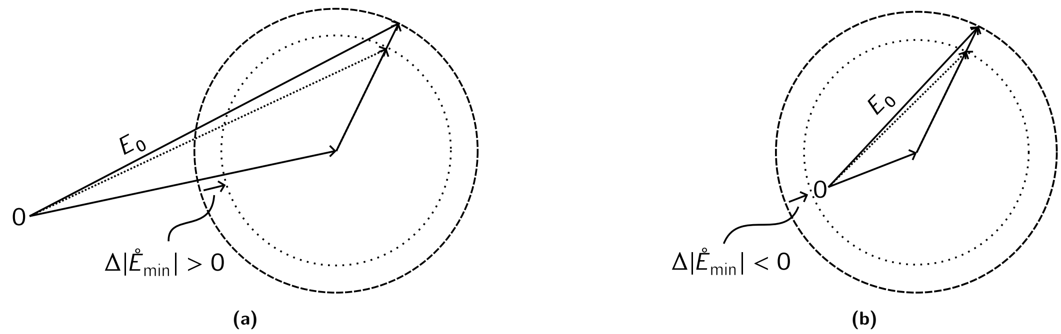

Figure 2.6: Illustration of how the introduction of a second, attenuated REV circle (dotted-lines circle) in addition to the initial REV circle (dashed-lines circle) can solve the ambiguity of the REV measurement: (a) $\Delta|\mathring{E}_{\mathrm{min}}|$ is positive, since the point in the REV circle closest to the origin moves away from the origin; (b) $\Delta|\mathring{E}_{\mathrm{min}}|$ is negative, since the point in the REV circle closest to the origin moves closer to the origin.

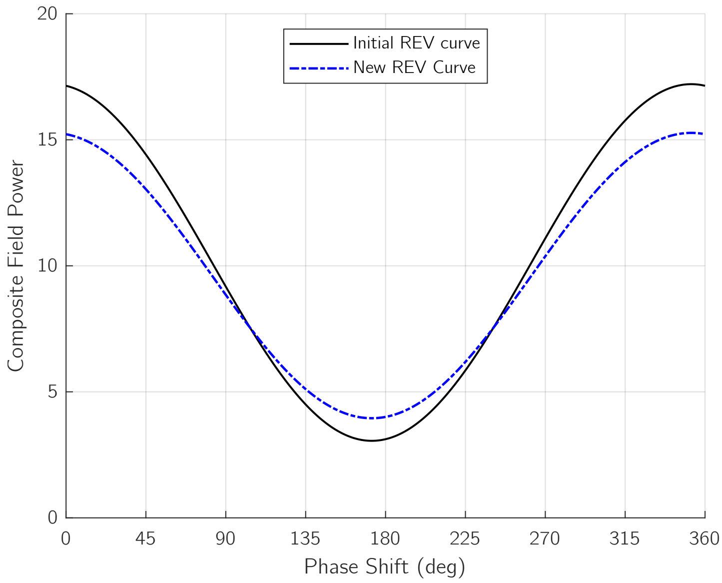

Figure 2.7: Illustration of the two generated REV curves. Here, the new REV curve has a larger composite field power $|\mathring{E}_n(\Theta)|^2$ minimum, so this REV measurement must be related to the "origin outside the REV circle" case.

2.1.2. SCSNS and SCSLS techniques

The technique referred to as SCSNS is described in [29], which provides scripts and functions for the chosen DUT of this thesis project – further described in Section 2.3. Unlike many other phaseless techniques, the SCSNS does not constitute an all-on calibration technique. However, as an advantage, implementation and the underlying principle of this technique is very simple. As seen in 2.8, the calibration routine is divided into three parts. First, it is the coarse measurement of the channels' excitation error magnitude, followed by the phase offset measurement, and finished by the fine measurement of the excitation error magnitude.

To obtain the excitation error magnitude of each channel, a measurement of the field magnitude of each individual channel is made. This is performed by sequentially activating only a single channel at a time, the n-the channel, and deactivating all other channels. Because all other channels are deactivated, the measured "composite" field magnitude in this case is contributed by only the n-th channel's. In other words, it is equivalent to measuring the vector field magnitude of the n-th channel, A_n. Furthermore, since the calibration beacon being at a FF distance and in the broadside angle is the assumption, then it is concluded that the channel's measured field magnitude, A_n, is proportional to the magnitude of the excitation error $E_{\mathrm{err},n}$.

$$A_{\mathrm{err},n} \propto A_n \tag{2.18}$$

After obtaining the coarse measurement of the channel excitation error magnitude, an intermediate magnitude calibration is performed by applying A_{min}/A_n to the n-th channel as weights, where A_{min} denotes the minimum recorded A_n across all channels. By normalizing to A_{min}, the applied weights are restricted to a range of 0 to 1. After applying the intermediate calibration to the magnitude response of the array, measurements of the excitation error phase component can then follow.

To obtain the excitation error phase component, the SCSNS assigns a reference channel, with a zero phase offset, $\Phi_{\mathrm{ref}} = 0$. To obtain the phase offset of all other channels, a sequential approach is again used. This time, the reference channel is activated in addition to the n-th channel, with all other channels deactivated.

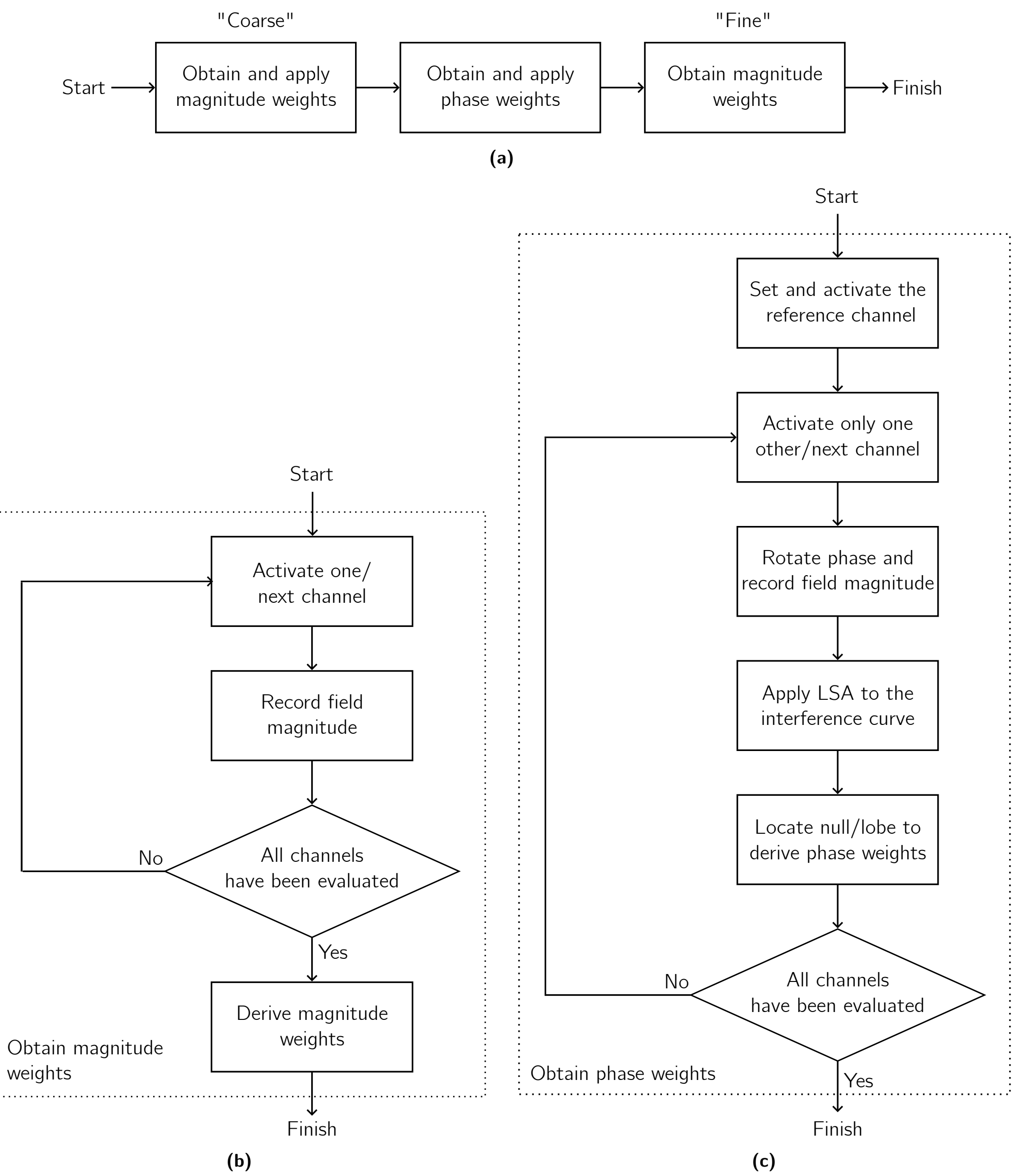

Figure 2.8: Flow diagram of the SCSNS/SCSLS technique: (a) overall main flow: (b) procedure to obtain magnitude weights; (c) procedure to obtain phase weights.

With only the two channels active, the n-th channel is phase shifted over 360° and the composite field magnitude is recorded for all phase settings. The interaction of the field vectors is illustrated in Equation 2.19 and Figure 2.9. Measuring only the composite field magnitude yields the "interference curve", shown in Figure 2.10. To ensure apple-to-apple comparison with the REV technique, LSA is also applied here to obtain the sinusoid-fitted interference curve. This represents a modification to the procedure compared to the reference implementation of this technique.

$$\begin{aligned} \mathring{E}_n(\Theta) &= E_{\mathbf{ref}} + E_n e^{j\Theta} \\ &= A_{\mathbf{ref}} + A_n e^{j(\Phi_n+\Theta)} \end{aligned} \tag{2.19}$$

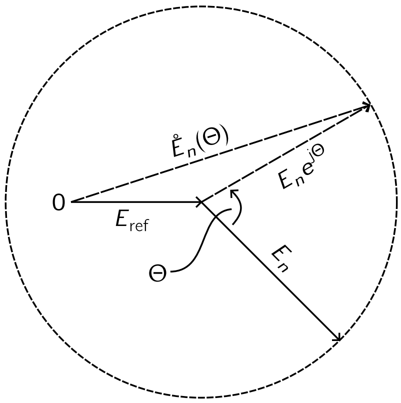

Figure 2.9: Illustration of the interaction between the field vectors of the reference and the n-th channels. Here, the reference channel is assumed to have no excitation error, while the n-th element has 50% larger amplitude with 45° phase offset.

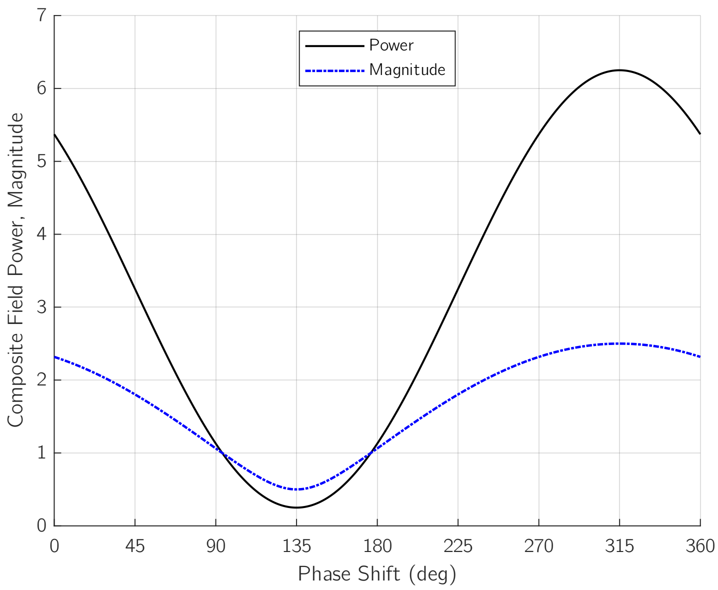

Figure 2.10: Illustration of an SCSNS/SCSLS interference curve. Here, the composite field power is defined simply as the composite field magnitude squared.

Next, by noting the location of the minimum in the interference curve, the phase offset of the n-th channel can be determined, since the associated phase shift must be exactly 180° out-of-phase with the reference channel. This process is then extended to all channels.

$$\Phi_{\mathrm{err},n} = \Phi_n = -180^\circ + \arg\min_{\Theta} |\mathring{E}_n(\Theta)| \tag{2.20}$$

As seen in Figure 2.9 and 2.10, inference of the n-th channel's phase offset can also be obtained by noting the location of the curve's maximum point. This is the exact difference of the SCSLS to the SCSNS. The phase offset associated with the maximum directly translates to the phase offset of the n-th channel.

$$\Phi_{\mathrm{err},n} = \Phi_n = \arg\max_{\Theta} |\mathring{E}_n(\Theta)| \tag{2.21}$$

After the excitation error phase component $\Phi_{\mathrm{err},n}$ is measured, the corresponding phase calibration weight $e^{\mathrm{j}\Phi_{\mathrm{err},n}}$ is applied. Next, the last step of the SCSNS and SCSLS calibration technique is the fine excitation error magnitude measurement. This *fine* measurement follow the exact procedure of its *coarse* counterpart. The only difference being the now applied phase correction.

From a procedural point-of-view, it can be concluded that the SCSNS/SCSLS methods is the faster calibration technique, since they require the generation of one interference curve, compared to the implemented REV's two curves. This is despite the former having separate calibration procedure to obtain the magnitude component of the calibration weights. To be specific, the amount of measurements needed to achieve calibrations are $2N + (N-1)(2^p - 1)$ and $N(2^p - 1) + 1$ for the SCSNS/SCSLS and REV techniques, respectively.

2.2. Off-broadside calibration

In the reference literature [17], it is suggested that a single REV measurement is unique to the "specific observation direction", which in this case refers to the calibration beacon direction. This is because the measured field vectors are the product of both non-ideal effects inherent to the individual signal path and the radiated fields in that specific direction. Meanwhile, through the concept of embedded element pattern, it is known that each individual antenna elements radiates differently in different directions. That is to say, to obtain optimum calibration across all steering angles, in REV or any phaseless calibration, measurements should be done for every steering angle. This is done by placing the calibration beacon in the direction of the intended steering angle when conducting phaseless measurements. To that end, the propagation channel, which until now had been assumed to have positioned the beacon in the broadside angle, shall now also consider placement in arbitrary angles.

Now, the response of the propagation channel is no longer identical for all channels. Instead, it is modified by progressive phase shifts due to the wavefront hitting the array elements at an angle. Since the DUT considered in this thesis project is only a ULA, the steering vector $\mathbf{a}(\phi)$ of this progressive phase shift effect is defined as in Equations 2.22 and 2.23, where ϕ, β, and d are the azimuth angle from broadside, the propagation phase constant, and the inter-element distance of the antenna array respectively.

$$a_n(\phi) = e^{-\mathrm{j}n\psi(\phi)}, n = 1, 2, ..., N \tag{2.22}$$

$$\psi(\phi) = \beta d \sin\phi \tag{2.23}$$

Since the beacon is now placed in arbitrary azimuth direction ϕ, the field vector present on the array is also naturally a function of ϕ.

$$\begin{aligned} \mathbf{E}(\phi) &= s_{\mathrm{tx}}(\mathbf{h}_{\mathrm{propagation}}(\phi) \odot \mathbf{w}_{\mathrm{err}}(\phi)) \\ &= s_{\mathrm{tx}} h_{\mathrm{fs}}(\mathbf{a}(\phi) \odot \mathbf{w}_{\mathrm{err}}(\phi)) \end{aligned} \tag{2.24}$$

Consequently, to extract information of the excitation error, which is now also assumed to be a function of ϕ, the inverse of the progressive phase shift vector $\mathbf{a}^{\circ -1}(\phi)$ must be applied as an additional step.

$$\mathbf{w}_{\text{err}}(\phi) = \frac{1}{s_{\text{tx}} h_{\text{fs}}} (\mathbf{E}(\phi) \odot \mathbf{a}^{\circ -1}(\phi)) \tag{2.25}$$

2.3. Device-under-test (DUT)

To obtain insights on the topic of calibration in constrained scenarios, a suitable DUT is needed. Chosen for its availability and ease-of-use, the CN0566 phased array development platform is used as the DUT throughout this project [30], [31]. The platform can be programmed using MATLAB, a programming language the author is familiar with. Additionally, there are plenty of example scripts and functions available [29].

In terms of hardware, this low-cost APAA platform operates on receive-mode at 10.0 - 10.5 GHz. It hosts a hybrid phased array architecture, containing an 8-channel horizontal ULA connected to two digital channels. On the radiating aperture, each analog channel is connected to a fixed 4-element vertical antenna array, therefore achieving a narrower beam horizontally. Overall, the radiating aperture is made up of 8×4 patch antennas, with beamforming capabilities along the azimuth (ϕ) directions. With 14 mm in horizontal and vertical spacing of elements, the overall size of the aperture is around 112 mm × 56 mm. Following Equation 2.26, where D is the aperture largest span and λ is the operating frequency, the Fraunhofer distance r_{FF} such that FF behavior can be approximated is around 1.088 m. It should be noted that the CN0566 is also equipped with a single transmit channel. However, it has no beamforming capability and must be connected to an external antenna through the use of coaxial cables.

$$r_{\text{FF}} = \frac{2D^2}{\lambda} \tag{2.26}$$

The CN0566 board is designed to be mounted on a Raspberry Pi. Additionally, it utilizes the PlutoSDR software-defined radio (SDR) module to further down-convert and digitize the intermediate frequency (IF) signal paths through its two digital receive channels. In combination, the CN0566 board, the Raspberry Pi and PlutoSDR module, will henceforth be referred to as the "Phaser Kit". Photograph of the Phaser Kit is shown in Figure 2.11.

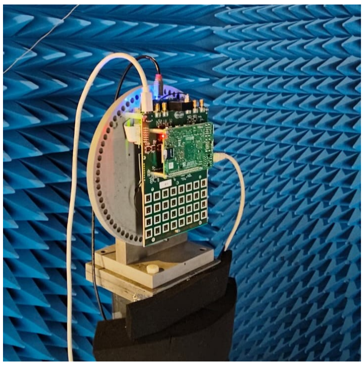

Figure 2.11: Photograph of the Phaser Kit.

A closer look at the array architecture of the DUT will reveal a two-tiered hybrid array. The lower tier is the analog arrays, which consist of four analog channels each. The digital array, which consists for two channels, occupy the higher tier. This tiered perspective is presented in Figure 2.12.

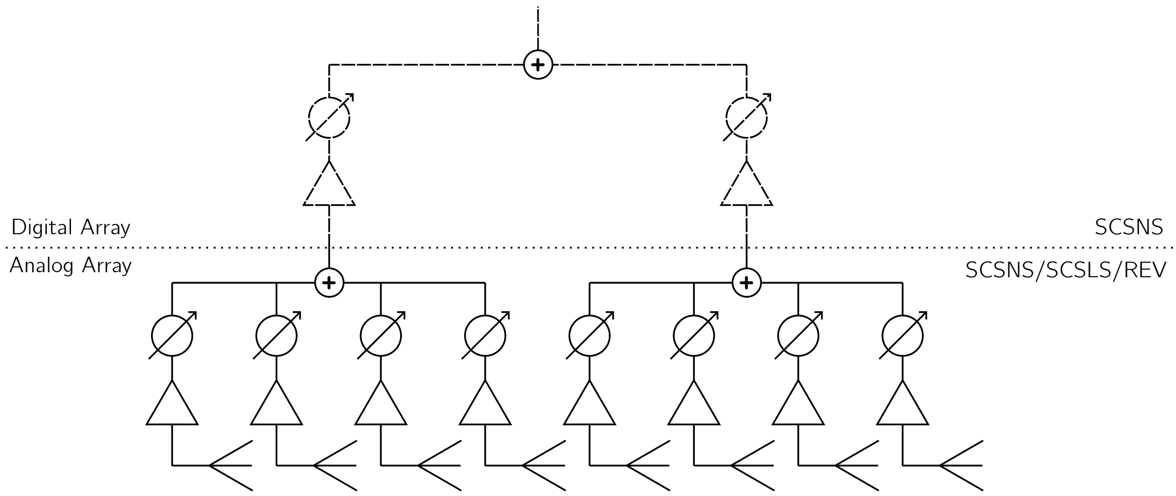

Figure 2.12: Array architecture of the CN0566. Solid- and dashed-lines are used to signify the analog and digital domains respectively.

Due to the hybrid architecture of the DUT, implementation of the calibration procedure is not straightforward, but require step-by-step approach. More specifically, calibration must be done at the analog array tier prior to the digital array tier. Only after calibration at both level is done can the whole DUT be considered calibrated. In this thesis project, when different calibration techniques are mentioned, their implementation refers only to the implementation done at the analog array level. Meanwhile, implementation of the digital array calibration is kept common for all, that is using the SCSNS technique. This approach is taken because the digital array consists of only two channels, therefore implementation of the SCSNS/SCSLS and REV would be very similar. Ultimately, this was done to avoid unnecessary complexity of the implementation.

2.4. Measurement instruments

In this work, a number of different experiments are done, each with their own measurement setup. Over the course of the thesis project, different instruments are used to best fit the needs and convenience at a given time. Here, some additional details on the instruments used for those measurements are provided.

The HB100, shown in Figure 2.13, is the device provided by Analog Device to act as the calibration beacon for its default SCSNS technique. Consequently, this module is used heavily, particularly early on in experiments covered in Chapter 3. Despite its marketed use as a low-cost Doppler radar module, here, the HB100 is utilized as a single-tone, fixed-power calibration beacon. Its compact nature especially allows for ease of setup. As antennas, the board utilizes a pair of patch antennas, radiating with 40° half power beam width (HPBW) on its broadside. Due to its low-cost, the frequency at which it radiates often vary device-to-device. The HB100 used in this thesis project radiates at around 10.4 GHz. To ensure consistency, all measurements of Chapter 3 are done at this frequency.

Still in Chapter 3, the effect of measurement SNR to calibration performance are evaluated. To achieve a varied measurement SNR, the transmit power of the calibration beacon is varied. Since the HB100 is fixed in power, an alternative device is needed. As such, the transmit channel of the phaser kit – which allowed programmability of the transmit power – was utilized. To ensure wide dynamic range of the applied SNR, a horn antenna with large gain is used, shown in Figure 2.14.

Figure 2.13: Photograph of the HB100.

Figure 2.14: Photograph of the large horn antenna.

Figure 2.15: Photograph of the horn antenna provided by Robin Radar Systems.

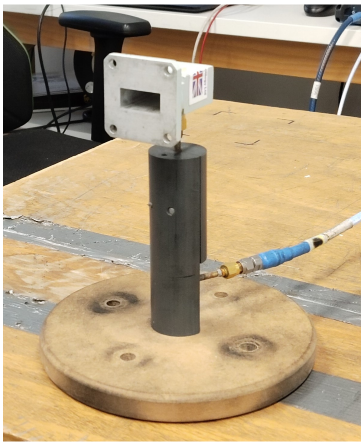

Figure 2.16: Photograph of the open-ended waveguide antenna.

Experiments in Chapter 4 required different features. First, the calibration beacon needed to allow transmit frequency programmability. Additionally, the antenna needed to have a wider beam to allow significant scattered paths to appear. As such, next, a VNA is used to generate the calibration signal, replacing the Phaser Kit's transmit channel. At the time, the Phaser Kit appear to have signal leakage from the transmit to receive channel. Meanwhile, the antenna used for the calibration beacon is changed to that shown in Figure 2.15. This multi octave horn antenna by A-Info has a frequency of operation between 7.5 - 18 GHz with 10 dB in nominal gain. The antenna was provided by Robin Radar Systems.

Lastly, in Chapter 4, a surrogate antenna was needed to allow power-delay profile (PDP) measurements of the echoic environments. Ideally, a patch antenna should be used to mimic the radiation pattern of the DUT's antenna elements. However, due to lack of availability, an open-ended waveguide – which have a wide beamwidth – is used instead. The antenna is shown in Figure 2.16. The wide beam width is important to be able to pick-up scatterd path signal components from wide angular directions.

2.5. Chapter summary

This chapter mainly provides background information for the following chapters. In particular, elaboration on the algorithm of the phaseless techniques used in this thesis project is provided. Furthermore, description on the APAA used as the DUT is also given. The key points are as follows.

1. Calibration weights $\mathbf{w}_{\text{cal}}$ are intended to compensate for the non-ideal effects of the signal path, represented by the excitation error $\mathbf{w}_{\text{err}}$. Ultimately, calibration performance is dictated by how accurately characterization of the channel's excitation errors are, since $\mathbf{w}_{\text{cal}}|_{\text{ideal}} = \mathbf{w}_{\text{err}}^{\circ -1}$;
2. In the REV calibration, measurements are made to the composite field vector from all channels. The REV curve is obtained by plotting the measured composite field power against the phase shift applied to the n-th channel over 360°. Solution to the REV measurement can be obtained by noting information of the curve's maximum and minimum;
3. In the SCSNS and SCSLS, the overall procedure is split into three parts: magnitude (coarse), phase offset, and magnitude (fine). To characterize the excitation error magnitude, both techniques rely on sequential measurement of the field magnitude present at each channel. To characterize the phase offset, the reference and the n-th channel is activated. The n-th channel is phase shifted over 360° and the measured composite field power is plotted. The phase offset of each channel can be obtained by noting the phase shift associated with the minimum (SCSNS) or maximum (SCSLS) points in the obtained curve;
4. Obtaining calibration weights for each intended steering angle is needed to achieve the best calibration performance. To do so, the calibration beacon is placed in the direction of the steered angles. This spatial information of the beacon must be taken into consideration through the steering vector $\mathbf{a}(\phi)$;
5. In this thesis project, the CN0566 receive-mode phased array development board is chosen as the DUT for its availability and ease-of-use. To do beamforming, the CN0566 utilizes the 8 RF channels at its disposal, which is split to two 4-channel analog subarrays connected to a 2-channel digital array, representing a hybrid architecture APAA.

3

Comparison of calibration techniques and impact of constrained scenarios

In this chapter, the calibration performance of different phaseless techniques are evaluated for different constrained scenarios, namely limited angle of the calibration beacon, decreased SNR, and the presence of scattered path(s). Before any measurement setups are presented, first, a new set of metrics must be defined. Then, for each scenario, the measurement procedure and results are shown before analysis is given.

3.1. Approach

As discussed previously in Subsection 1.4.2, evaluation of calibration performance typically made in the existing literature retains some problems. Here, ideal patterns, i.e. AF patterns, are used as the comparison reference, since they most closely represent ideal calibration. As such, radiation patterns need to be generated to enable comparison to the ideal patterns. From then on, pattern-derived metrics are defined to evaluate calibration performance. This section discuss how these processes are done.

3.1.1. Generating the patterns

Typically, measurement of radiation patterns is done through thorough measurement of the field vector at all directions of interest. Unfortunately, such measurements are notoriously time-consuming, since they require many cumbersome mechanical movements. In this project, since only steered beams are considered, the measurement of beam patterns can be substituted with the much quicker measurement of their mathematically-equivalent patterns, henceforth referred to as "EQ patterns". In this work, EQ pattern of a steered beam at ϕ_0 is obtained by electronically steering the beam across azimuth angles while recording the field power received from a fixed source located at a FF distance and angular position ϕ_0. Figure 3.1 shows the setup used to measure EQ patterns.

Relating to the context of calibration, mathematically, the EQ pattern is defined as expressed in Equation 3.1. There, the vector dot product with the all-ones vector simply implies summation of the vector elements and m represents the m-th index of all M number of evaluated directions.

$$A_{\mathrm{EQ},m} = |\mathbf{1}^T(\mathbf{E} \odot \mathbf{w}_{\mathrm{cal}} \odot \mathbf{w}_{\mathrm{exc,m}})| \tag{3.1}$$

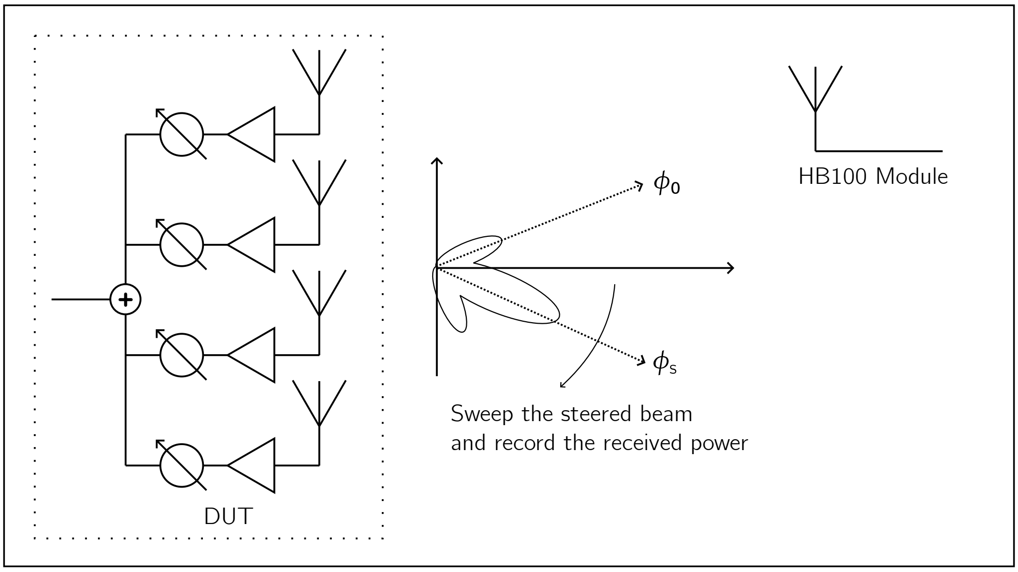

Figure 3.1: The measurement setup to generate the EQ pattern of a steered beam. The HB100, acting as the reference source, is placed at a FF distance from the DUT.

Strictly speaking, the patterns measured through this method is not *exactly* equivalent to patterns measured through conventional procedures. Crucially, EQ patterns do not take into account scanning loss, since the reference beacon is at a fixed location, ϕ_0. Coincidentally, scanning loss is not accounted in AF patterns either, allowing direct comparison between the two.

3.1.2. Pattern-derived metrics

Moving forward, pattern-derived metrics will be used as an alternative to the statistical quantities of calibration weights error typically used in the literature, especially within the context of making a fair comparison between two calibrations. Since only steered beams are considered, traditional beam steering metrics can be used: steering angle error; HPBW broadening; maximum SLL. These parameters quantify some specific quality from the entire synthesized beam.

Alternatively, a more thorough quantitative approach can also be used to obtain quantities more flexibly and relevant to the beam pattern being synthesized. For example, when the accuracy of the beam pattern over the entire radiation direction is important, then the RMSE of the calibrated beam pattern can used as the calibration performance metric. Formulation of the pattern RMSE is shown in Equation 3.2, where A is the magnitude response of a radiation pattern, M refers to the number of angles evaluated, m is the angle index, and the meas and ideal subscripts refer to the measured calibrated and ideal pattern data. This metric represents the overall fitting of the measured pattern to the ideal, with a lower RMSE portraying a better beam forming performance.

$$\mathrm{RMSE}_{\mathrm{pattern}} = \frac{\sqrt{\sum_{m=1}^{M} |A_{\mathrm{ideal},m} - A_{\mathrm{meas},m}|^2}}{\sqrt{\sum_{m=1}^{M} A_{\mathrm{ideal},m}^2}} \tag{3.2}$$

In this case, since nulls are not generally important in steered beams, the minimum values of $A_{\mathrm{ideal},m}$ and $A_{\mathrm{meas},m}$ are limited to -25 dB to avoid division by small number. Conversely, when only a range of directions are relevant or more important, then the RMSE can be calculated for only the relevant directions, or be weighted accordingly. In this approach, derivation of the metrics can be highly customized to the intended beam pattern.

As discussed previously, in this work, EQ patterns are used instead of the conventional radiation patterns. As such, $A_{\mathrm{meas},m}$ can be substituted for $A_{\mathrm{EQ},m}$. On the other hand, typically, the ideal pattern will have already been derived from the system requirements, in the form of an analytical AF pattern or alternatively using simulated pattern from an EM solver. Figures 3.2 and 3.3 illustrates the pattern-derived metrics collected in this chapter.

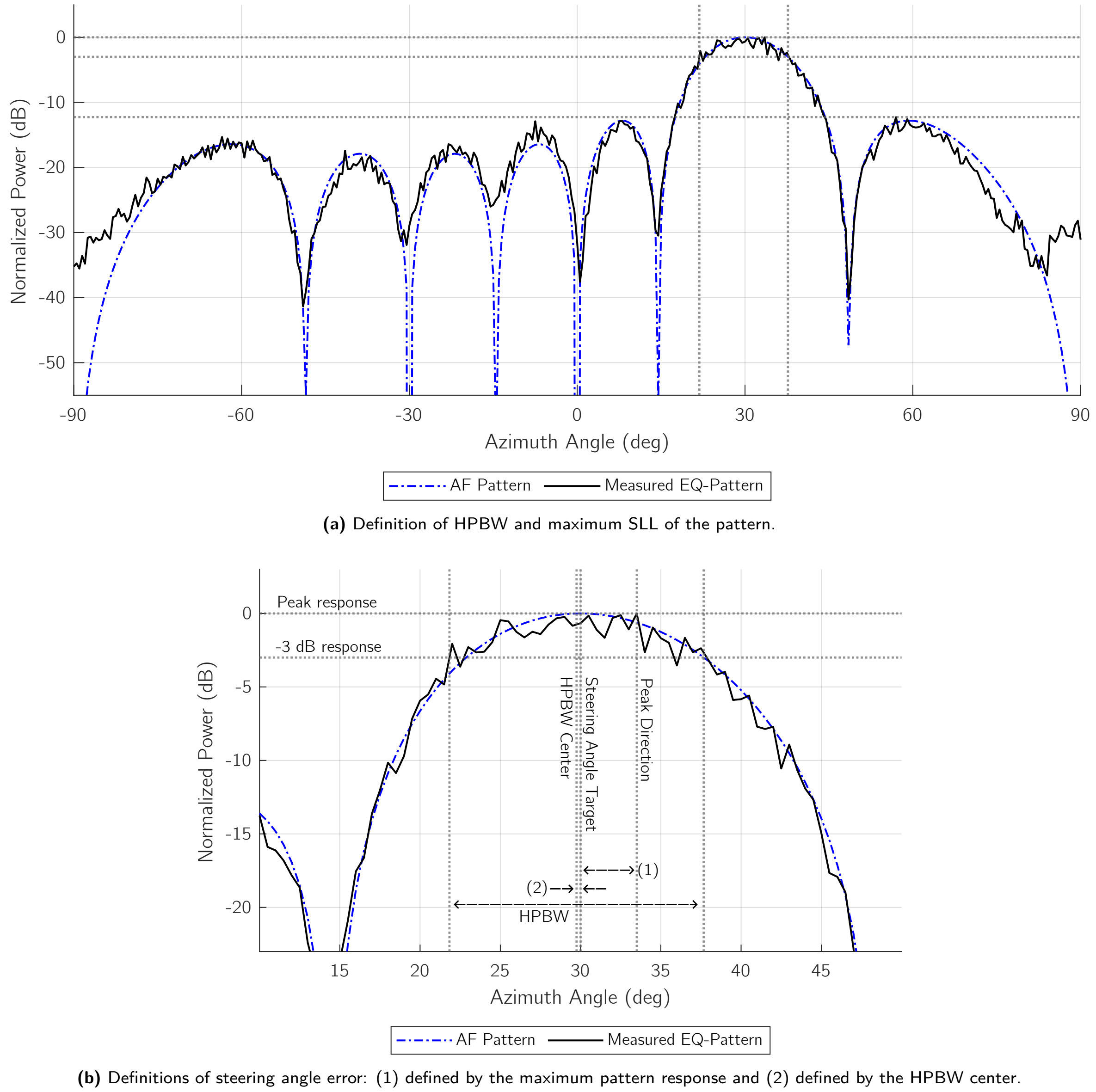

(a) Definition of HPBW and maximum SLL of the pattern.

(b) Definitions of steering angle error: (1) defined by the maximum pattern response and (2) defined by the HPBW center.

Figure 3.2: Illustration of the different calibration performance metrics derived from by comparing the measured EQ pattern to the ideal AF pattern.

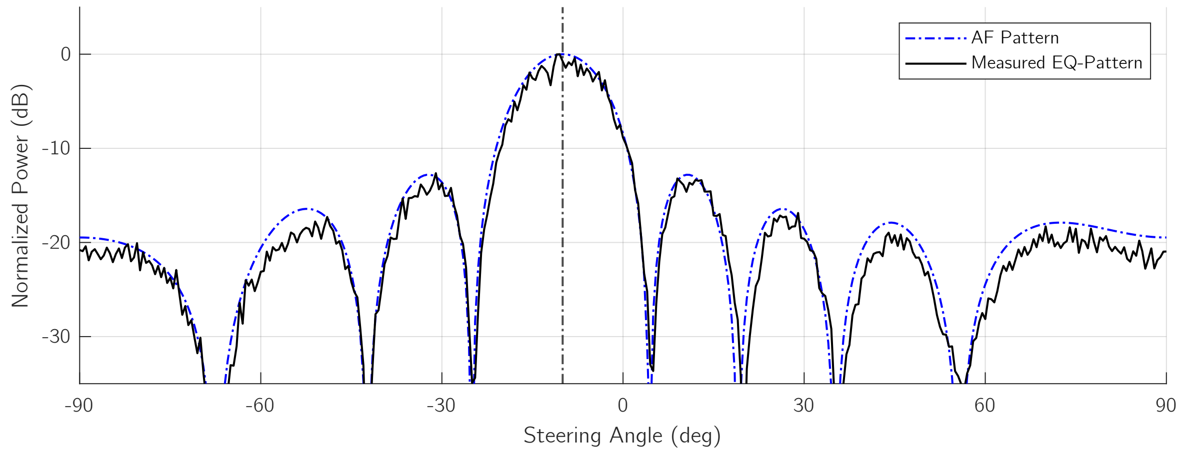

(a) EQ pattern corresponding to 11.52% pattern RMSE..

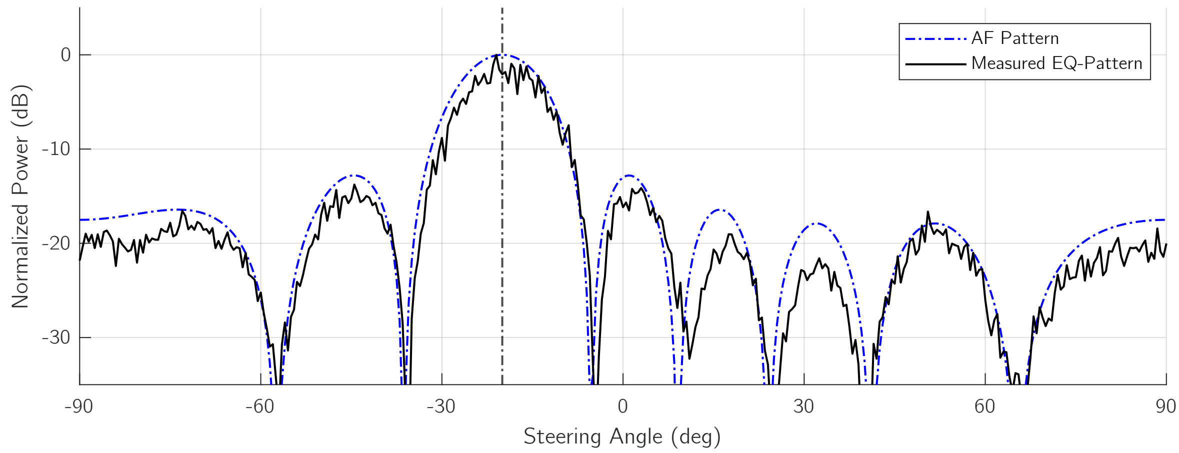

(b) EQ pattern corresponding to 18.97% pattern RMSE.

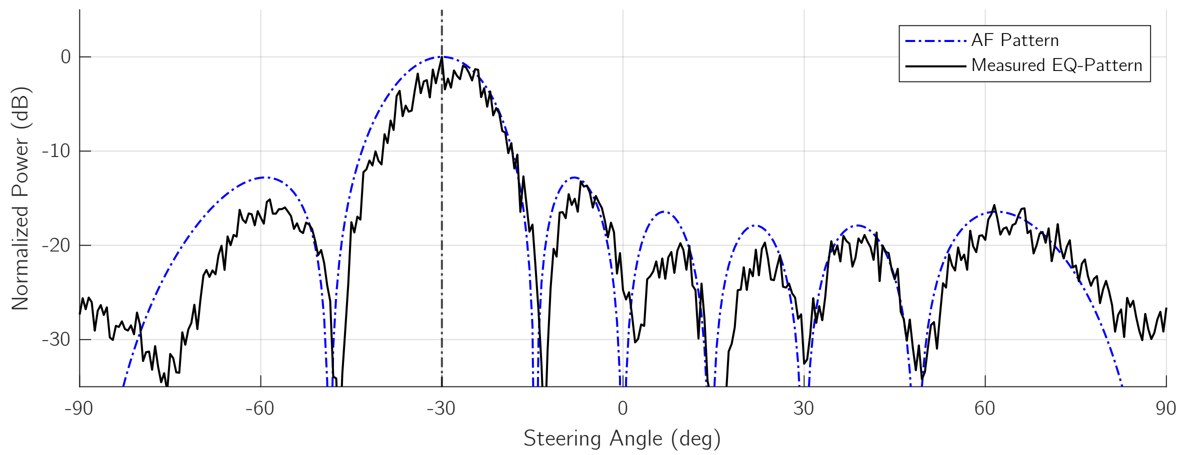

(c) EQ pattern corresponding to 23.73% pattern RMSE.

Figure 3.3: Illustration of the different EQ patterns corresponding to different pattern RMSE values.

3.2. Calibration performance for finite sampling of calibration angles

In Section 2.2, it was presented that optimum calibration weights can be obtained by calibration for each steering angle. In this first part of evaluating the calibration performance in constrained scenarios, the effect of finite sampling of calibration angles is evaluated. The measurement setup for this calibration scenario can be seen in Figure 3.4. As seen from the setup, calibration weights are collected for various beacon angles: from -50° to 50° in azimuth, with 10° steps. In total, there will be 33 sets of calibration weights, with 11 for each phaseless technique. Next, these calibration weights are used to generate steered beam EQ patterns with the same set of angles as the steering angles: from -50° to 50° in azimuth, with 10° steps. Then, metrics can be extracted from all 121 generated EQ patterns, or 363 when considering all three phaseless techniques.

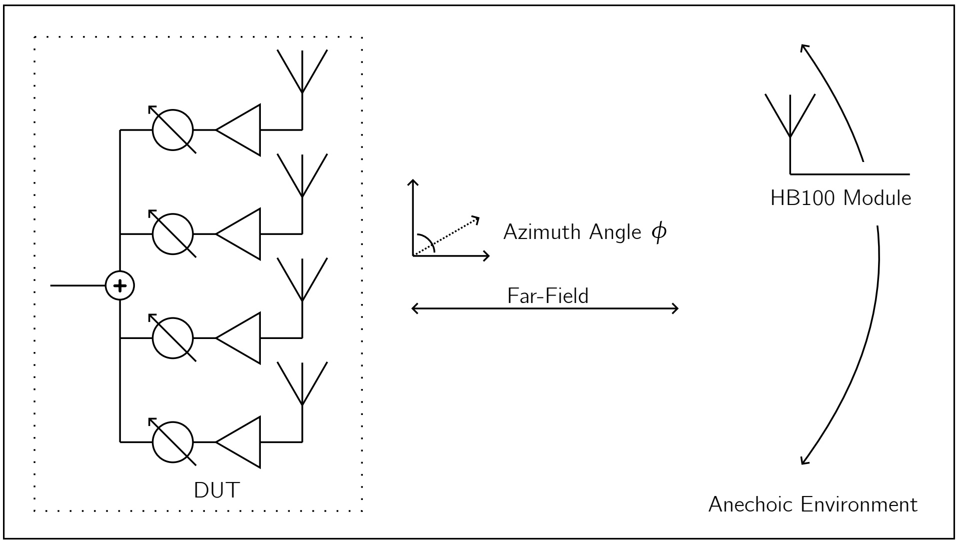

Figure 3.4: The measurement setup to perform calibration of steered beams at an arbitrary azimuth angle.

To make analyses on these metrics, they are reorganized based on how these EQ patterns were obtained. More specifically, they are reorganized based on the absolute difference between the azimuth angle of the beacon when the calibration weights were obtained ϕ_{cal}, and the intended azimuth angle of the steered beam pattern ϕ_{steer}. That is to say, a small angle difference $|\phi_{\text{cal}} - \phi_{\text{steer}}|$ would represent a finer sampling of calibrations of the steering angles, whereas a larger angle difference represents sparser sampling. The number of measurements associated to each case of absolute angle difference can be observed in Figure 3.5. Unfortunately, invalid results were observed for EQ patterns generated using calibration with ϕ_{cal} at 30° due to measurement error, therefore that leaves only 110 EQ pattern data in total.

Although multiple different metrics were collected, the two most relevant plots are shown: steering angle error and beam pattern RMSE. Figure 3.6 presents the pattern RMSE when comparing between the obtained EQ pattern to the ideal AF pattern. Additionally, Figure 3.7 shows the change of steering angle error with variation of the absolute angle difference. For both plots – and other similar plots throughout this chapter – a slight horizontal offset for each phaseless technique is introduced avoid overlap of the different traces. Despite the visual trick, these plots overlap on the same absolute angle differences: 0°, 10°, 20°, ..., 100°.

As seen in Figure 3.7 and 3.6, across metrics, it can be concluded that the REV and SCSNS techniques outperforms the SCSLS technique, with very little difference between the two. Moreover, **the calibration**

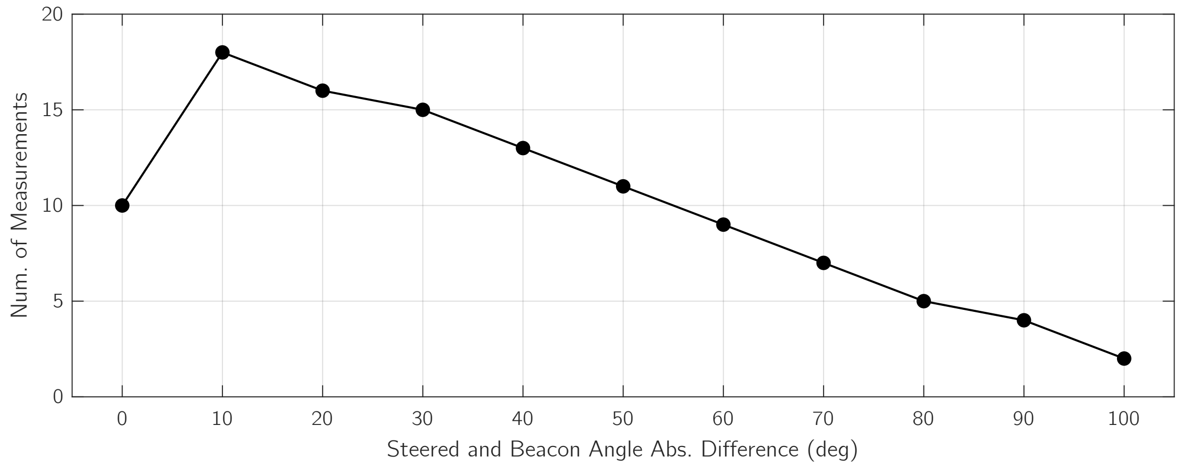

Figure 3.5: Number of measurements associated to each case of absolute angle difference, $|\phi_{\text{cal}} - \phi_{\text{steer}}|$.

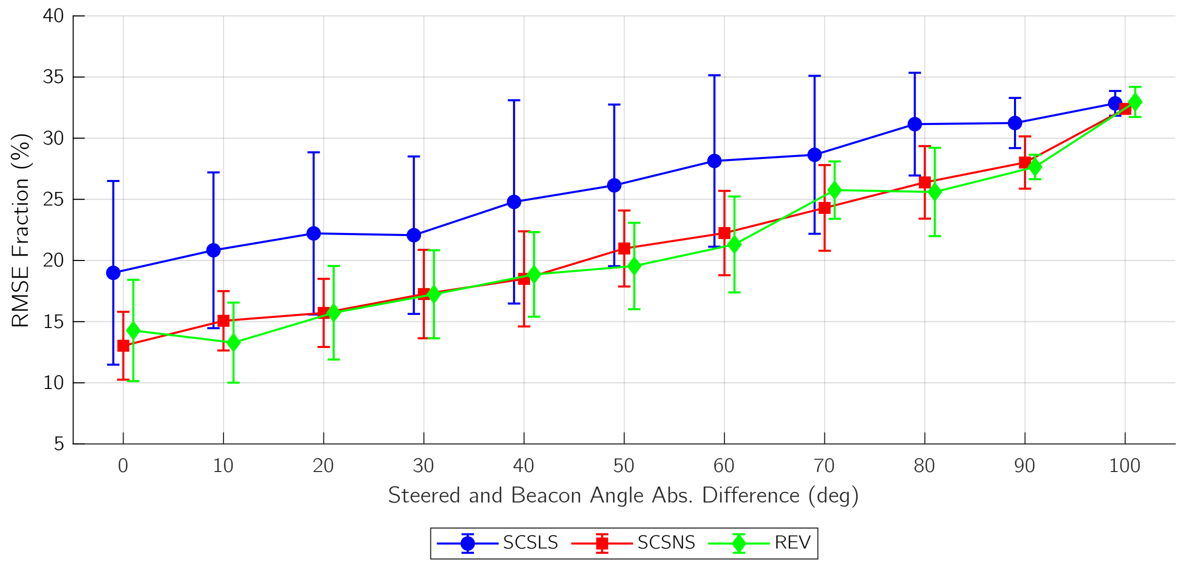

Figure 3.6: The mean and SD of pattern RMSE as the absolute angle difference widens for various phaseless calibration techniques.

performance clearly deteriorates as the absolute angle difference is raised: increased steering angle error and pattern RMSE. To quantify this phenomena, linear regression is be applied to summarize its effect on calibration performance. On average, an increment of 10° angle difference increases the steering angle error (HPBW center) by 0.360°, 0.341°, and 0.305° and the the pattern RMSE by 1.41%, 1.67%, and 1.69% for calibration using SCSLS, SCSNS, and REV techniques, respectively. Meanwhile, other calculated metrics – HPBW, maximum SLL – remain stable with change of the absolute angle difference.

While these numbers may seem small, in reality, calibration is often done only at a single direction, at broadside. In other words, in many cases, the absolute angle difference $|\phi_{\text{cal}} - \phi_{\text{steer}}|$ regularly reach high numbers. Assuming a steering angle of 50°, up to 1.5° of steering error are expected on average, with outlier cases possibly yielding larger errors. Depending on the application of the APAA, this amount of steering

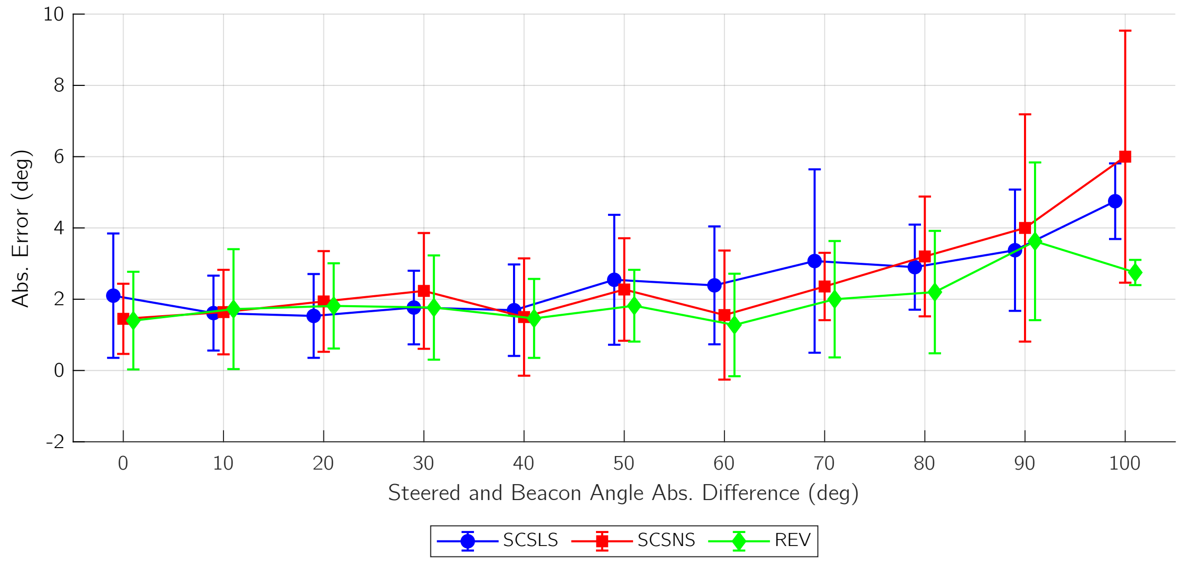

(a) Based on maximum pattern response.

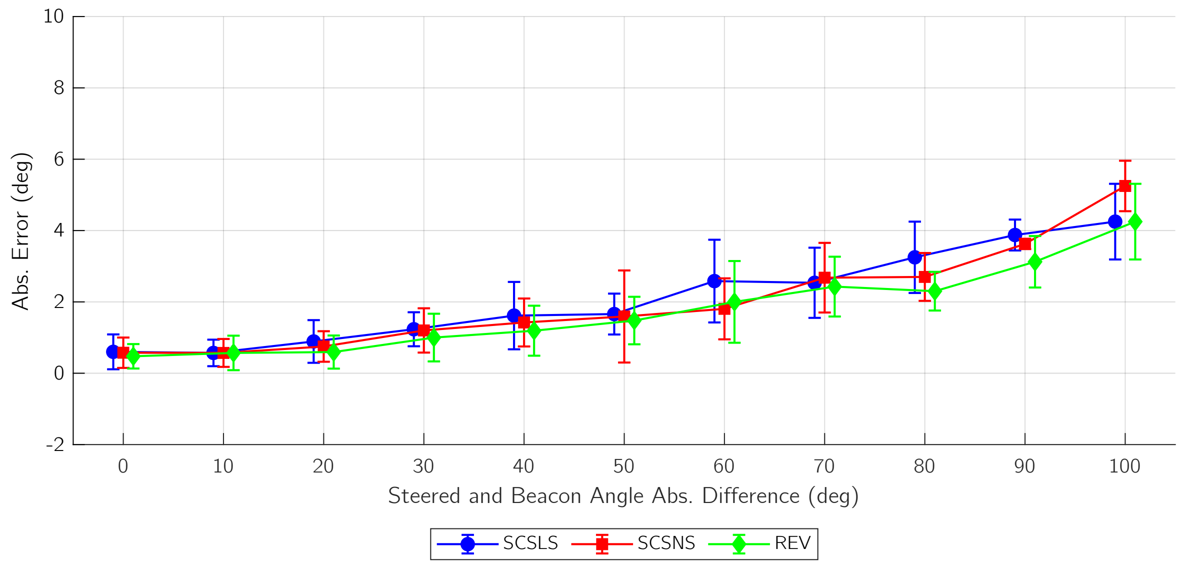

(b) Based on the angle center of the 3 dB beam width of the pattern.

Figure 3.7: The mean and SD of steering angle error as the absolute angle difference widens for various phaseless calibration techniques.

error can cause non-negligible effect to performance. As such, **the sampling of steering angles used as calibration angles should be set with these trade-offs in mind and contextualized with the system requirements**, whether it be in terms of steering error, pattern RMSE, or other pattern-derived metrics of choice.

To do so, the following empirical method can be implemented. First, given a set of system requirements, define the pattern-derived metrics of importance. Next, a similar set of measurements to those done in this section should be done. In doing so, a trade-off curve between the selected metrics against the absolute angle difference can be drawn. Based on this curve, the sampling requirements for calibration angles can be decided, and future calibrations can be done according to this policy. For example, from Figure 3.7, if an average steering angle error of less than 1° is desired, then the sampling requirements must ensure that the absolute angle difference be less than 20°. All-in-all, such empirical method ensure the calibration performance for wide-angled steered beams fulfill the criteria given by system requirements.

3.3. Calibration performance in varied SNR scenarios

Finally, measurements are also done to evaluate calibration performance when SNR is reduced. The measurement setup is shown in Figure 3.8. Here, the transmit channel on board the Phaser Kit is used as the calibration beacon to allow programmability of the transmit power. In doing so, variability of the measurement SNR can be achieved, though indirectly. Moreover, the positioning of the beacon is kept at the broadside angle of the DUT throughout this experiment as the focus is kept only on the effect of the SNR.

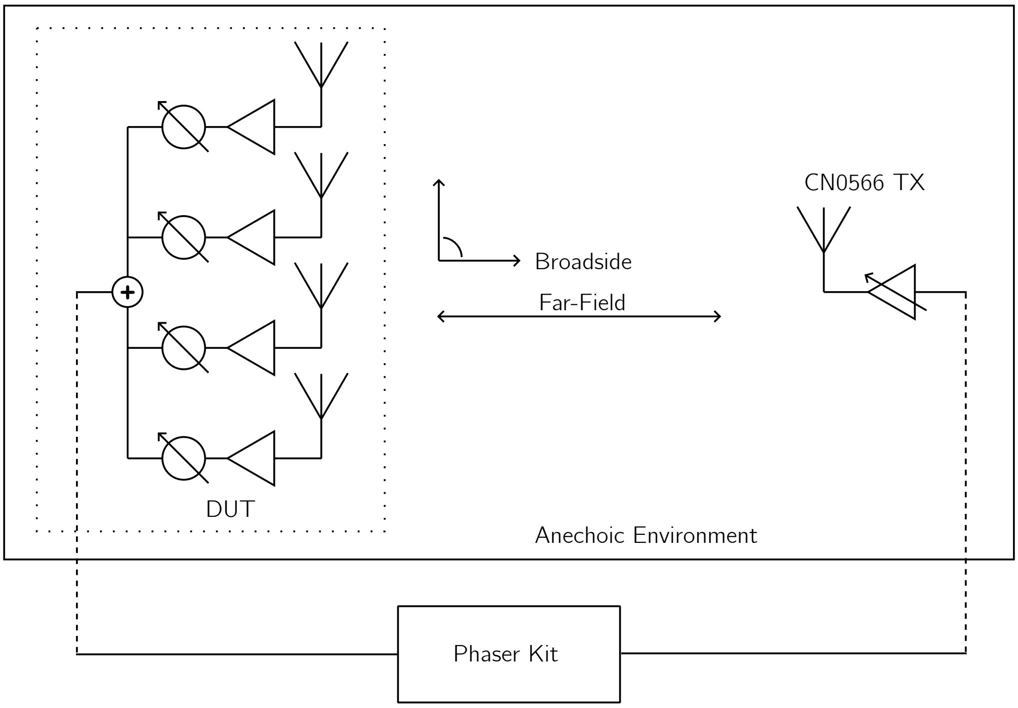

Figure 3.8: The measurement setup to evaluate the effect of decreased SNR to calibration performance.

In this experiment, the transmit power setting is varied to observe change to the measurement SNR. To do so, a coefficient to the transmitted waveform $c_{\text{TX-mod}}$ is varied from 0 dB to -25 dB with 5 dB increments, followed by -25 dB to -55 dB with 1 dB increments. To measure the corresponding SNR for each increment, the following procedure is done. First, the signal spectrum present at each channel is recorded sequentially. This is done by activating only one channel at-a-time, whilst all other channels are deactivated. From each spectrum, the frequency bin at which maximum power is located is noted. In addition to some neighboring bins, these frequency bins and their corresponding power are then defined as the beacon signal's spectrum. Next, the SNR can be calculated through Equation 3.3, where ΣP_{signal} refers to the total power of the beacon signal's spectrum, and ΣP_{noise} refers to the total power of every other frequency bin. The SNR average of the 8 channels are used to summarize the overall SNR of the measurement for the corresponding $c_{\text{TX-mod}}$ coefficient.

$$\text{SNR} = \frac{\Sigma P_{\text{signal}}}{\Sigma P_{\text{noise}}} \tag{3.3}$$

With the transmit power coefficient $c_{\text{TX-mod}}$ changed, calibration procedure is done to obtain calibration weights. EQ patterns can then be recorded and pattern-derived metrics can be calculated. Figure 3.9 and 3.10 shows the pattern RMSE and maximum SLL metric as the measurement SNR is varied. Several interesting findings can be noted from the figures. First, that there exist SNR cut-off thresholds which varies for each phaseless technique, denoted by the vertical dashed lines. **When the SNR is above this cut-off, good calibration performance is observed**. They are -10.42, -13.45, and -8.87 dB for SCSLS, SCSNS, and REV respectively. Based on these numbers, in order of robustness to SNR, the SCSNS outperforms the SCSLS and REV techniques. The observed pattern RMSE is stably around 20% or lower and the EQ pattern's maximum SLL is not far from around -12.8 dB, which is the expected value for an 8-channel array with no amplitude tapering. **In fact, there appears no indication that any excess SNR beyond the threshold corresponds to further improvement of calibration performance**. This opens up the possibility of trading-off the excess SNR for other advantages, such as calibration speed. Meanwhile, below this threshold, both metrics vary wildly, indicating calibration is no longer reliable.

3.4. Calibration performance in echoic environment

Next, experiments are done to compare the calibration performance obtained in an environment with scattered paths, i.e. an echoic environment. To do so, a very simple change to the previous measurement setup is made. Whereas in Section 3.2, calibration was done in the anechoic chamber, here, it is done in a typical echoic environment. The measurement setup is shown in Figure 3.11. Due to practical limitations of this approach, the evaluated azimuth angles are limited to from 0° to 50°, with 10° increments. Photograph of the measurement setup is shown in Figure A.1. From Section 3.2, the REV and SCSNS are known to yield similar calibration performance. For brevity, this experiment was applied only for calibration using the REV technique.

In Figure 3.12, the number of measurements associated to each absolute angle difference can be observed. Since less azimuth angles are evaluated, both the number of measurements and the span of angle differences gathered in the echoic case is less compared to those found in the prior experiment.

In general, the calibration performance obtained from the echoic scenario shows mixed results. Take the pattern RMSE and maximum SLL metrics, shown in Figure 3.13 and 3.14. In the former figure, similar level of performances is indicated. Meanwhile, the echoic scenario clearly produces worse results in the latter. The combination of the two suggests the EQ patterns obtained from both scenarios maintain similar likeness levels to the ideal pattern, but with differences in magnitude of the SLL. Additionally, the trend between the absolute angle difference to the evaluated metrics are more obfuscated in the echoic scenario compared to that found in the anechoic scenario. The author hypothesizes that this is caused by distortions caused by the scattered path in the echoic channel, an effect that is highly geometry-dependent.

Ultimately, insufficient evidence has been collected in this experiment to draw conclusions when comparing the calibration performance in echoic and anechoic scenarios. The lack of results here is the main driver to continue to investigate the topic of calibration in echoic scenarios, further discussed in Chapter 4.

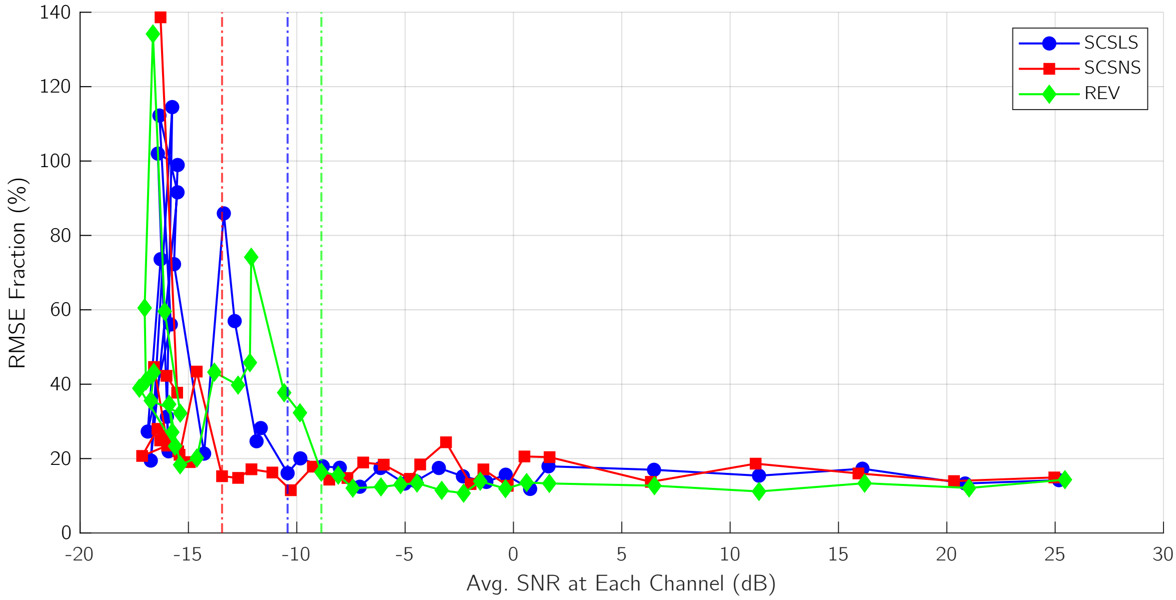

Figure 3.9: The pattern RMSE of the EQ patterns as the measurement SNR is varied.

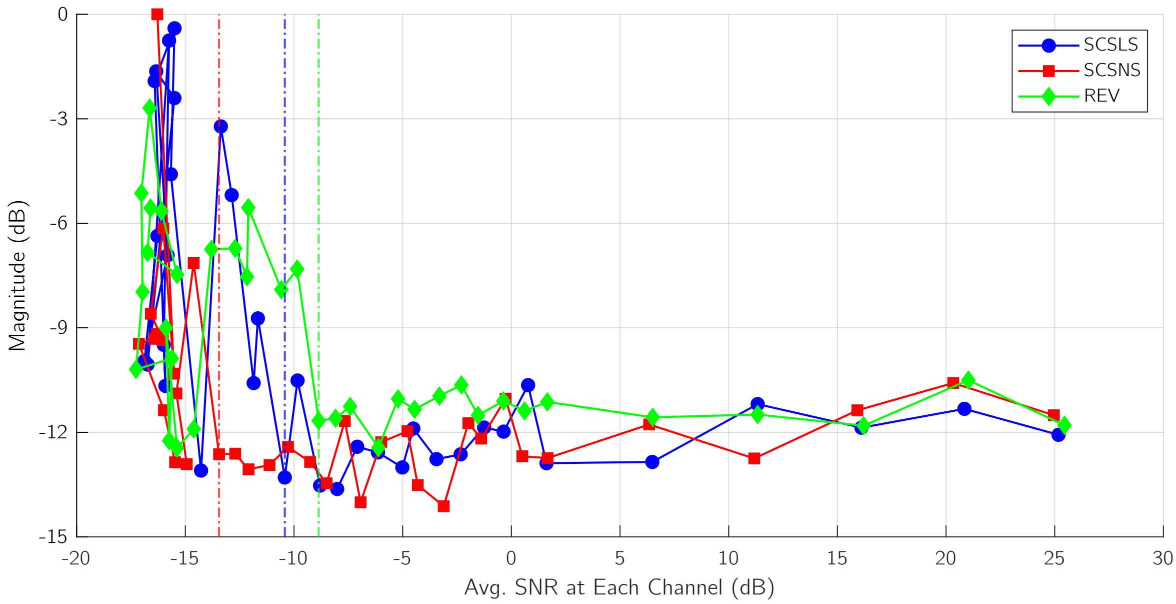

Figure 3.10: The maximum SLL of the EQ patterns as the measurement SNR is varied.

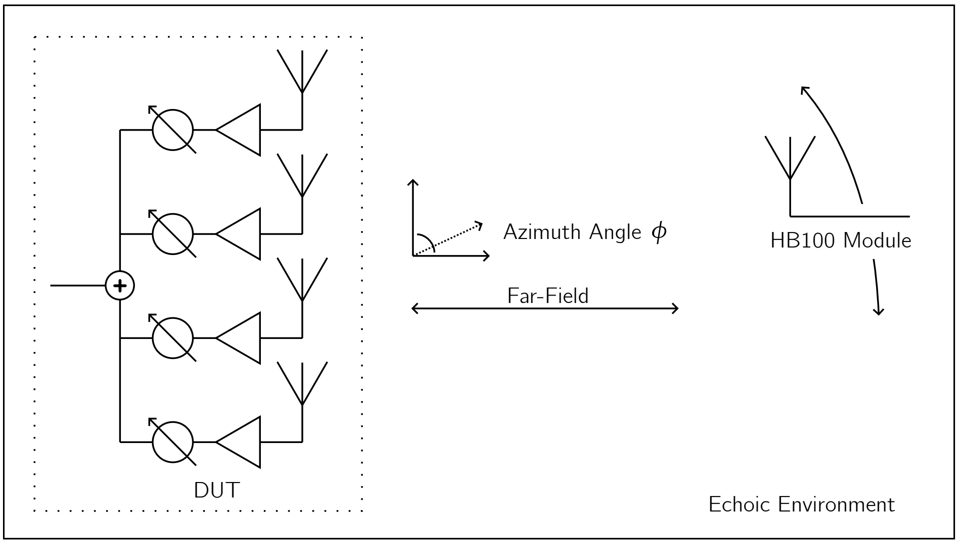

Figure 3.11: The measurement setup to perform calibration in an echoic environment. Unlike in Figure 3.4, the set of azimuth angles ϕ to be evaluated are limited due to practical constraints.

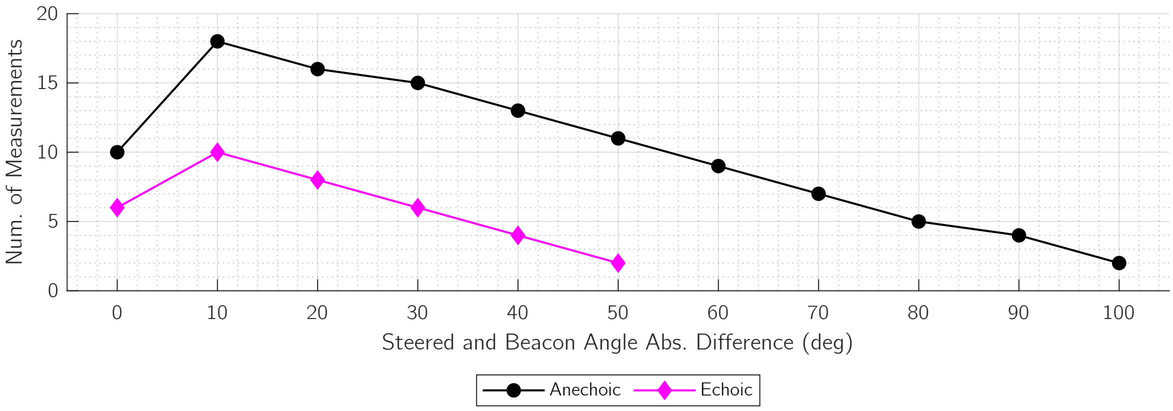

Figure 3.12: Number of measurements associated to each case of absolute angle difference, $\phi_{\text{cal}} - \phi_{\text{steer}}$. Now, added trace for the echoic case measurement.

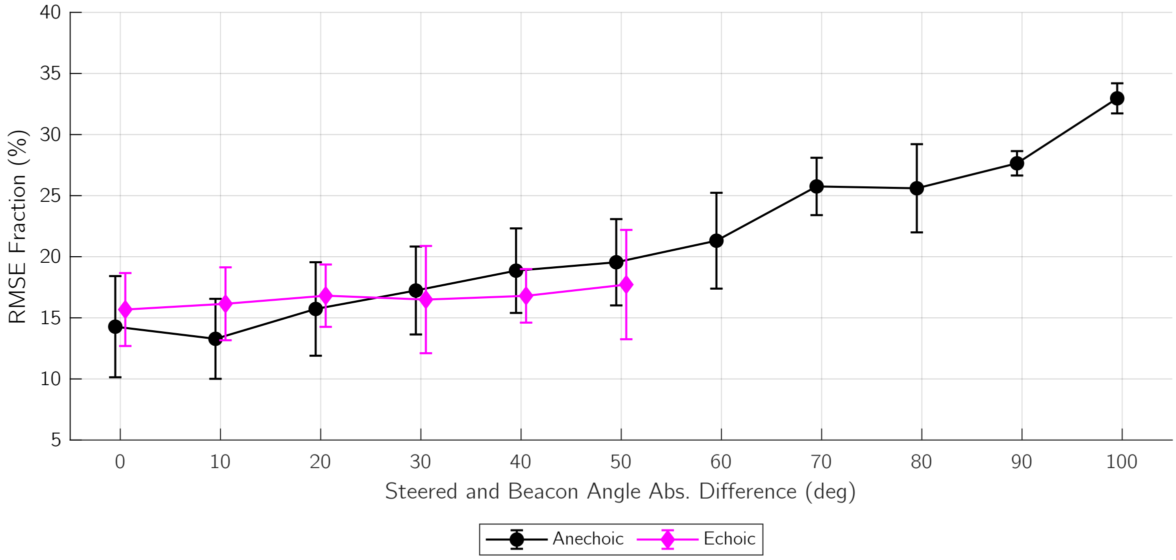

Figure 3.13: The mean and SD of pattern RMSE as the absolute angle difference widens for the anechoic and echoic scenarios.

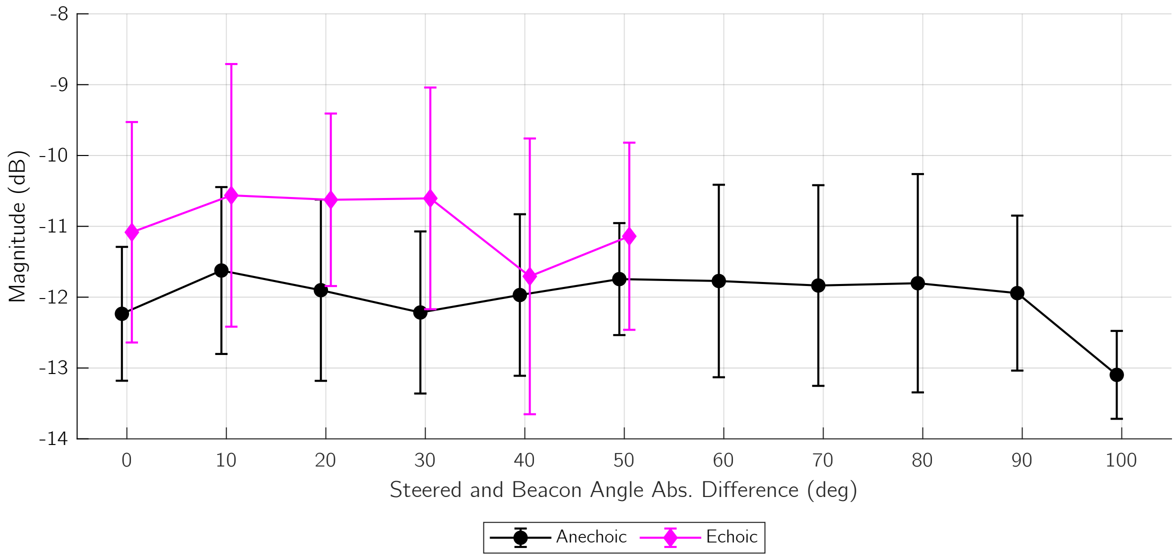

Figure 3.14: The mean and SD of maximum SLL as the absolute angle difference widens for the anechoic and echoic scenarios.

3.5. Chapter conclusions

1. In this chapter, for the first time, comparison of calibration techniques through comprehensive pattern-derived quantitative metrics are done;
2. Quantification of the effect of finite calibration angle and decreased measurement SNR to APAA calibration performance is done for the first time;
3. When subjected to different angle difference $|\phi_{\mathrm{cal}} - \phi_{\mathrm{steer}}|$, the REV and SCSNS outperforms the SCSLS techniques in the selected metrics, steering angle error and especially pattern RMSE. This was concluded from Figures 3.7 and 3.6, respectively.
4. On average, an increment of 10° absolute angle difference $|\phi_{\mathrm{cal}} - \phi_{\mathrm{steer}}|$ increases the steering angle error by 0.360°, 0.341°, and 0.305° and the the pattern RMSE by 1.41%, 1.67%, and 1.69% for calibration using SCSLS, SCSNS, and REV techniques respectively. While these numbers may seem small, their values will build up for wide steering angles, e.g. 1.5 $^{\circ}$ steering errors for beam steering at 50°. Moreover, these values represent only the *on average* trends, with outliers possibly yielding higher errors on occasions. As such, the sampling of steering angles used as calibration angles should be set with these trade-offs in mind and contextualized metrics derived from the system requirements,
5. When subjected to varied measurement SNR, a threshold-like phenomena are observed. With SNR above these values, similar calibration performance was achieved but without further improvement with excess SNR. To be specific, when above the threshold, the observed pattern RMSE is stably around 20% or lower and the pseudo-pattern's maximum SLL is around -13 dB, which is the expected value for arrays with no amplitude tapering. Meanwhile, calibration fails at SNR lower than the threshold.
6. Each phaseless technique demonstrated different threshold SNR values, which points to the robustness of each technique when subjected to noise. The SCSNS shows the highest robustness, with an SNR threshold of -13.45 dB. The SCSLS and REV techniques trail with -10.42 dB and -8.87 dB respectively.
7. Experiment with calibration in echoic scenario found inconclusive results, which motivated the work and discussions in Chapter 4.

4

Echo-aware calibration

As seen in Section 3.4, unsurprisingly, the presence of scattered signal components in echoic environment deteriorates the reliability of APAA calibration. In this chapter, analytical description of the multipath behavior in echoic environments is presented. Based on this description, two approaches leveraging frequency diversity information is proposed: FDA and GIED, or echo de-embedding for short. Some proof-of-concept experiments are then done to prove the validity of the proposed methods.

4.1. Multipath channel model

It has been established that the field vectors present at the array depend not only on the excitation errors of each channel, but also the channel response experienced by each channel. This is formulated in Equation 4.1. However, since the environment is echoic, the signal that arrives at the array aperture consists not only of components that have propagated through the LoS path, but also through scattered paths. In the following analysis, scatterers and reflectors are assumed to be in FF distance of the antenna array. This is illustrated in Figure 4.1. As such, the propagation response is of a multipath channel.

$$\mathbf{E} = s_{\mathrm{tx}}(\mathbf{h}_{\mathrm{propagation}} \odot \mathbf{w}_{\mathrm{err}}) \tag{4.1}$$

Equation 4.2 describes the multipath channel response of the signal present at the array aperture, with narrowband assumption and static environment. All terms are are described through a path-specific common complex response h, and a phase shift vector $\mathbf{a}$ which accounts for the signal phase difference arriving at each channel due to the AoA.

$$\mathbf{h}_{\mathrm{propagation}} = h_{\mathrm{LoS}}\mathbf{a}_{\mathrm{LoS}} + \sum_{p=1}^{P} h_{\mathrm{refl},p}\mathbf{a}_{\mathrm{refl},p} + \sum_{q=1}^{Q} h_{\mathrm{scat},q}\mathbf{a}_{\mathrm{scat},q} \tag{4.2}$$

As seen in Equation 4.2, the first term relates to the LoS signal component of the channel, which experiences free-space-like propagation. As formulated in Equation 4.3, $r_{\mathrm{rx,tx}}$, f, and c represent the beacon-array distance, signal frequency, and the speed of light constant.

$$h_{\mathrm{LoS}} = h_{\mathrm{fs}} = \frac{c}{f}\frac{1}{4\pi r_{\mathrm{rx,tx}}} e^{-\mathrm{j}\frac{2\pi f r_{\mathrm{rx,tx}}}{c}} \tag{4.3}$$

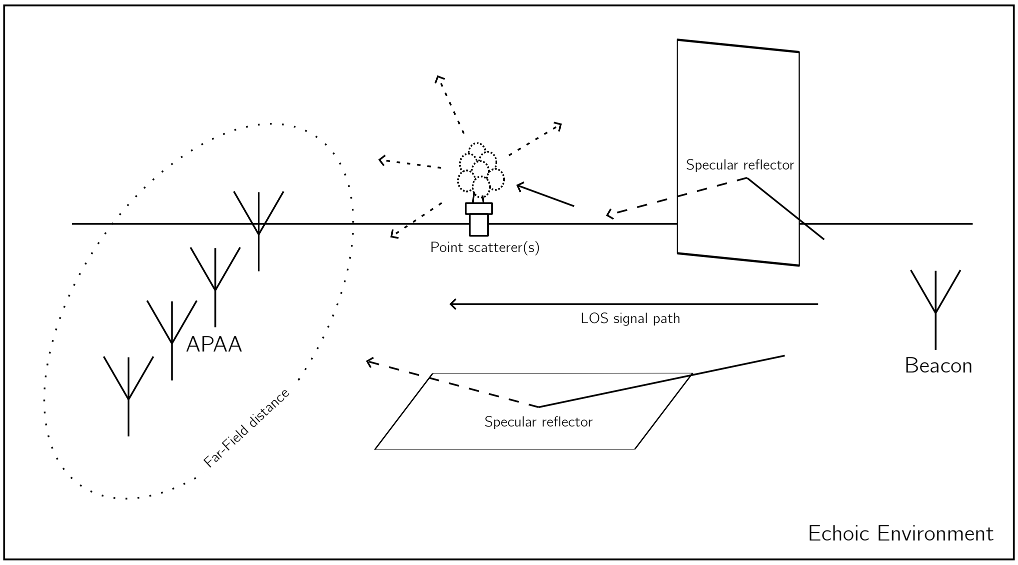

Figure 4.1: Illustration of the radiation path of the different signal components: LoS and scattered path components.

Meanwhile, the second and third term represent the contribution of all scattered paths, which are modelled as either specular reflectors or point scatterers. In Equation 4.4, the response of the former is described. Leveraging image theory, the specular reflector path response is simply the free-space propagation response over the combined beacon-p-th reflector-array path, with the addition of a correction coefficient $c_{\text{refl},p}$. This coefficient accounts for the reflection coefficient of the p-th reflecting surface.

$$h_{\text{refl},p} = c_{\text{refl},p} \left(\frac{c}{f} \frac{1}{4\pi r_{\text{refl},p}} e^{-\mathrm{j}\frac{2\pi f r_{\text{refl},p}}{c}} \right) \tag{4.4}$$

$$r_{\text{refl},p} = r_{\text{refl-}p,\text{tx}} + r_{\text{rx,refl-}p} \tag{4.5}$$

For the last term, the bistatic radar equation is used to model the scattered path response due to point scatterers, as shown in Equation 4.6. Here, the correction coefficient $c_{\text{scat},q}$ accounts for the radar cross section (RCS) and phase response of the point scatterer.

$$h_{\text{scat},q} = c_{\text{scat},q} \left(\frac{c}{f} \frac{1}{(4\pi)^{\frac{3}{2}} r_{\text{scat-}q,\text{tx}} r_{\text{rx,scat-}q}} e^{-\mathrm{j}\frac{2\pi f r_{\text{scat},q}}{c}} \right) \tag{4.6}$$

$$r_{\text{scat},q} = r_{\text{scat-}q,\text{tx}} + r_{\text{rx,scat-}q} \tag{4.7}$$

With the assumption that the beacon, specular reflectors and point scatterers being in FF distance of the antenna array, the phase shift vector $\mathbf{a}$ can be approximated to simply a *progressive* phase shift vector $\mathbf{a}(\phi)$, which depends only on the AoA of corresponding signal path ϕ. Elements of vector $\mathbf{a}(\phi)$ is defined as in Equation 4.8 - 4.9.

$$a_n|_{\text{FF}} = a_n(\phi) = e^{-\mathrm{j}n\psi(\phi)}, n = 1, 2, ..., N \tag{4.8}$$

$$\psi(\phi) = \beta d \sin\phi \tag{4.9}$$

The use of frequency diversity to resolve multipath problems are well documented. However, to the knowledge of the author, the use of frequency diversity to allow calibration in echoic environments is not found in the literature. Here, some methods are proposed to make use of frequency diversity information to allow calibration in echoic environments.

4.2. Frequency-domain averaging (FDA)

The most straightforward interpretation of frequency diversity information is through the use of Fourier transform (FT) and its inverse, the inverse Fourier transform (IFT). Equation 4.10 - 4.11 show the well-known discrete expressions of FT and IFT for an arbitrary frequency domain and time domain signal pairs $X[k]$ and $x[d]$. In the following discussion, it shall become clear that the FDA aims to recover LoS signal component by evaluating the 0-th time bin of the time-domain by taking the average of the frequency domain information. Figure 4.2 shows the procedure of the FDA method.

$$X[k] = \sum_{d=0}^{L-1} x[k] e^{-\mathrm{j}\frac{2\pi}{L}2kd} \tag{4.10}$$

$$x[d] = \frac{1}{L} \sum_{k=1}^{L-1} Y[k] e^{\mathrm{j}\frac{2\pi}{L}2kd} \tag{4.11}$$

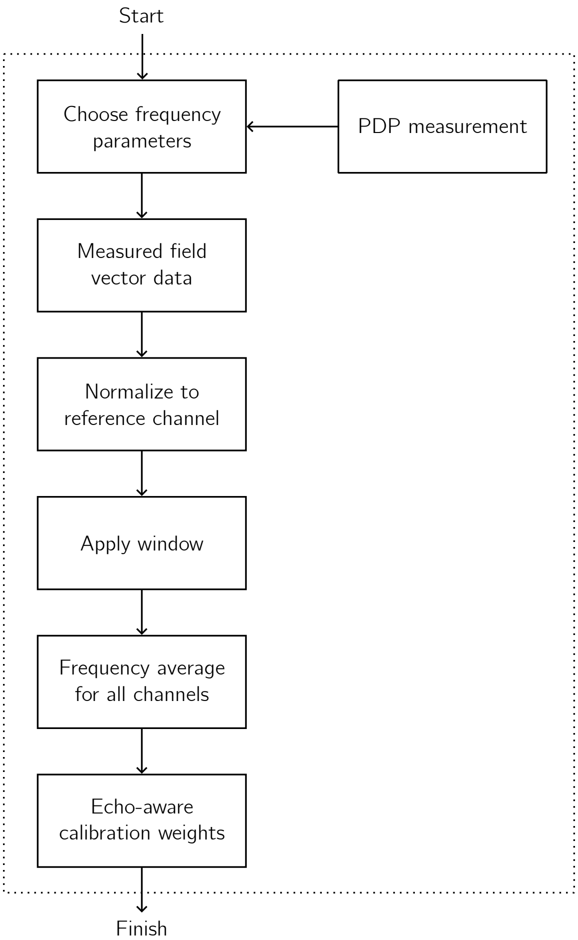

Figure 4.2: Step-by-step procedure of the proposed FDA method.

Now, the multipath propagation channel can be defined explicitly in terms of the time delays τ_{LoS}, $\tau_{\mathrm{refl},p}$

$\tau_{\text{scat},q}$ by applying the relation $\tau = r/c$. The resulting expression is shown in Equation 4.12.

$$\mathbf{h}_{\text{propagation}} = C_{\text{LoS}} e^{-\text{j}2\pi f \tau_{\text{LoS}}} \mathbf{a}_{\text{LoS}} + \sum_{p=1}^{P} C_{\text{refl},p} \mathbf{a}_{\text{refl},p} e^{-\text{j}2\pi f t_{\text{refl},p}} + \sum_{q=1}^{Q} C_{\text{scat},q} \mathbf{a}_{\text{scat},q} e^{-\text{j}2\pi f t_{\text{scat},p}} \tag{4.12}$$

Additionally, in Equation 4.12, the coefficients $c_{\text{refl},p}$, $c_{\text{scat},q}$ and attenuations due to propagation, whether free-space or bistatic scattering, are lumped into new coefficients C_{LoS}, $C_{\text{refl},p}$, and $C_{\text{scat},q}$. This is done not only for notational brevity, but also to explicitly separate the highly frequency-sensitive phase rotation variables $e^{-\text{j}2\pi f[...]}$ from other variables.

$$C_{\text{LoS}} = \frac{h_{\text{LoS}}}{e^{-\text{j}2\pi f \tau_{\text{LoS}}}} \tag{4.13}$$

$$C_{\text{refl},p} = \frac{h_{\text{refl},p}}{e^{-\text{j}2\pi f r_{\text{refl},p}}} \tag{4.14}$$

$$C_{\text{scat},q} = \frac{h_{\text{scat},q}}{e^{-\text{j}2\pi f r_{\text{scat},q}}} \tag{4.15}$$

The expression for the multipath propagation channel can be defined in terms of excess delays $\Delta\tau_{\text{refl},p}$ and $\Delta\tau_{\text{scat},q}$ in reference to the time delay of the LoS signal component.

$$\mathbf{h}_{\text{propagation}} = e^{-\text{j}2\pi f \tau_{\text{LoS}}} \left(C_{\text{LoS}} \mathbf{a}_{\text{LoS}} + \sum_{p=1}^{P} C_{\text{refl},p} \mathbf{a}_{\text{refl},p} e^{-\text{j}2\pi f \Delta\tau_{\text{refl},p}} + \sum_{q=1}^{Q} C_{\text{scat},q} \mathbf{a}_{\text{scat},q} e^{-\text{j}2\pi f \Delta\tau_{\text{scat},q}} \right) \tag{4.16}$$

$$\Delta\tau_{\text{refl},p} = \tau_{\text{LoS}} - \tau_{\text{refl},p} \tag{4.17}$$

$$\Delta\tau_{\text{scat},q} = \tau_{\text{LoS}} - \tau_{\text{scat},q} \tag{4.18}$$

For further brevity, the multipath propagation channel can be simply defined in terms of the LoS signal component, shown in Equation 4.16.

$$\mathbf{h}_{\text{propagation}} = C_{\text{LoS}} e^{-\text{j}2\pi f \tau_{\text{LoS}}} \mathbf{a}_{\text{LoS}} \odot (\mathbf{1} + \boldsymbol{\Gamma}(f)) \tag{4.19}$$

Here, $\boldsymbol{\Gamma}(f)$ is effectively the multipath interference ratio. It summarizes the vector sum response due to all scattered paths in terms of a ratio to the LoS signal component. This is shown in Equation 4.20. Meanwhile, The $\mathbf{1}$ term is simply the all-ones vector representing the LoS signal component.

$$\boldsymbol{\Gamma}(f) = C_{\text{LoS}}^{-1} \mathbf{a}_{\text{LoS}}^{\circ -1} \odot \left(\sum_{p=1}^{P} C_{\text{refl},p} \mathbf{a}_{\text{refl},p} e^{-\text{j}2\pi f \Delta\tau_{\text{refl},p}} + \sum_{q=1}^{Q} C_{\text{scat},q} \mathbf{a}_{\text{scat},q} e^{-\text{j}2\pi f \Delta\tau_{\text{scat},q}} \mathbf{a}_{\text{LoS}} \right) \tag{4.20}$$

At last, gathering from Equations 4.1 and 4.19, field vectors present in the array can be summarized as shown in Equation 4.21.

$$\mathbf{E} = s_{\text{tx}} C_{\text{LoS}} e^{-\text{j}2\pi f \tau_{\text{LoS}}} \mathbf{a}_{\text{LoS}} \odot (\mathbf{1} + \boldsymbol{\Gamma}(f)) \odot \mathbf{w}_{\text{err}} \tag{4.21}$$

In its current form, if the field vectors are sampled, recovering the LoS signal component through IFT is theoretically *possible*, but it won't be *feasible*. This is because exact information of the LoS signal time delay τ_{LoS}, or equivalently, the exact distance $r_{\text{rx,tx}}$, must be known. In fact, given the signal frequency of around 10 GHz where picoseconds or submilimeter level of offset is equivalent to tens of degrees in phase offset, the level of information accuracy needed to recover the LoS signal component is impossible to obtain in practice.

To overcome this problem, a simple procedure involving normalization and Maclaurin series simplification is used. First, any measurement of the field vector $\mathbf{E}$ should be normalized to field vector measurement of the reference channel. For simplicity, the reference channel is arbitrarily chosen as the first channel, $n_{\text{ref}} = 1$. In doing so, the evaluated field vector is no longer a function of the bulk time delay due to LoS propagation, as seen in Equation 4.22. Rather, it is now a function of the excess delays $\Delta\tau$.

$$\mathbf{E}_{\text{norm}} = \frac{\mathbf{E}}{E_1} = \frac{1}{a_{\text{LoS},1}(1+\Gamma_1(f))w_{\text{err},1}}\left(\mathbf{a}_{\text{LoS}} \odot (\mathbf{1}+\mathbf{\Gamma}(f)) \odot \mathbf{w}_{\text{err}}\right) \tag{4.22}$$

Now, it is important to evaluate conditions and parameters so that the IFT approach will converge to the correct solution. The expression in 4.22 can be reorganized as in Equation 4.23, or alternatively Equation 4.24, which defines $\mathbf{E}_{\text{norm}}$ for each n-th channel.

$$\mathbf{E}_{\text{norm}} = \frac{1}{1+\Gamma_1(f)}\frac{1}{a_{\text{LoS},1}w_{\text{err},1}}\left(\mathbf{a}_{\text{LoS}} \odot (\mathbf{1}+\mathbf{\Gamma}(f)) \odot \mathbf{w}_{\text{err}}\right) \tag{4.23}$$

$$E_{\text{norm},n} = \frac{1}{1+\Gamma_1(f)}(1+\Gamma_n(f))\frac{a_{\text{LoS},1}w_{\text{err},n}}{a_{\text{LoS},n}w_{\text{err},1}}, \quad n = 1,2,...,N \tag{4.24}$$

The Maclaurin series expansion, shown in Equation 4.25, can be applied to the normalized field vector expression.

$$\frac{1}{1+x} = 1 - x + x^2 - x^3 + ... \tag{4.25}$$

$$E_{\text{norm},n} = (1-\Gamma_1(f)+\Gamma_1^2(f)-\Gamma_1^3(f)+...)(1+\Gamma_n(f))\frac{a_{\text{LoS},1}w_{\text{err},n}}{a_{\text{LoS},n}w_{\text{err},1}}, \quad n = 1,2,...,N \tag{4.26}$$

From 4.26, it is clear that the expression for the normalized field vector of the n-th channel $E_{\text{norm},n}$ will not be stable for $|\Gamma_1(f)| > 1$. In other words, the definition found in Equation 4.22 is only valid for scenarios where the scattered path signal components sum are weaker than the LoS signal component, $|\Gamma_1(f)| < 1$.

Now, to build the frequency diversity information, frequency diversity measurements are done. The field vectors $\mathbf{E}_{\text{norm}}$ is sampled – using phaseless techniques – at a set of frequencies f_k. The resulting discrete samples are defined by Equations 4.27 and 4.28.

$$E_n[k] = E_{\text{norm},n}(f_k) \tag{4.27}$$

$$f_k = f_{\text{min}} + k\Delta f, \quad k = 0,1,2,...,L-1 \tag{4.28}$$

Naturally, careful selection of the frequency sampling parameters is required. First, the frequency resolution Δf directly affects the unambiguous excess delay $\Delta\tau_{\text{u,max}}$, shown in Equation 4.29. A sufficiently small resolution should be selected to avoid aliasing of scattered path signal components into the 0-th time bin, thereby smearing the LoS signal component.

$$\Delta\tau_{\text{u,max}} = \frac{1}{\Delta f} \tag{4.29}$$

The sampled bandwidth $B = (L-1)\Delta f$ is also another important parameter. Similar to any other FT/IFT operation, together with the windowing, the bandwidth defines the time resolution of the resulting time domain signal. As such, ample bandwidth should be selected such that the earliest scattered path is outside of the 0-th time bin.

$$\Delta\tau \approx \frac{1}{B} \tag{4.30}$$

Since the selection frequency parameters Δf and B are dependent on the existing scattered path excess delays present in the environment, PDP measurements can be done prior to frequency diversity measurements to identify this. Otherwise, oversampling of the field vectors $E_{\text{norm},n}$ can be done by undershooting Δf and overshooting B to widen the span of allowed excess delays τ.

However, it is important to choose a narrow enough bandwidth such that the channel response parameters not related to excess delay $\Delta\tau$ can be assumed to be quasi-static, i.e. C_{LoS}, $C_{\mathrm{refl},p}$, $C_{\mathrm{scat},q}$, $\mathbf{a}_{\mathrm{LoS}}$, $\mathbf{a}_{\mathrm{refl},p}$, $\mathbf{a}_{\mathrm{scat},q}$. In doing so, frequency dependency of the measurements can be singly attributed to the excess delay of scattered paths $\Delta\tau$, which vastly simplify the signal model. This is a plausible assumption, since the bandwidth is much smaller than the center frequency, $B \ll f_{\mathrm{min}} + \frac{B}{2}$.

Next, the LoS signal component can be obtained by applying, discrete IFT to the sampled frequency-domain signal $E_n[k]$.

$$e_n[d] = \frac{1}{L}\sum_{k=0}^{L-1} E_{\mathrm{norm},n}[k]e^{\mathrm{j}\frac{2\pi}{L}2kd} \tag{4.31}$$

However, thanks to the normalization step, the LoS signal component can be obtained by simply observing the 0-th time bin ($d = 0$), which is associated to $\Delta\tau = 0$. The resulting expression, shown in Equation 4.32, is now reduced to simple a frequency-domain averaging, hence the name, FDA.

$$e_n[0] = \frac{1}{L}\sum_{k=0}^{L-1} E_{\mathrm{norm},n}[k] \tag{4.32}$$

Given appropriate selections of frequency resolution Δf and bandwidth B, the result of averaging from Equation 4.32 can be easily predicted. From Equation 4.20, it has been established that variable $\Gamma_n(f)$ is simply the frequency response of the many *true* scattered paths. As such, the expression for $E_n[k]$ in Equation 4.26 can be seen as the sum response of the LoS path, and the many scattered – both true and *harmonic* – paths. All scattered paths contain phase rotation variables $e^{-\mathrm{j}2\pi f[\dots]}$, which, if taken the frequency-domain average, will yield to zero. Therefore, the result of the averaging will also be equivalent to the expression shown in Equation 4.33.

$$e_n[0] = \frac{a_{\mathrm{LoS},1}w_{\mathrm{err},n}}{a_{\mathrm{LoS},n}w_{\mathrm{err},1}} \tag{4.33}$$

At last, calibration weights can be derived from the normalized excitation error $w_{\mathrm{err},n}/w_{\mathrm{err},1}$. This is done by solving Equation 4.32 through measurement data, and Equation 4.33, where $a_{\mathrm{LoS},n}$ can be easily derived.

4.3. Geometry-informed echo de-embedding (GIED)

While the IFT-equivalent method of FDA might be attractive due to its straightforwardness, it also suffers due to its simplicity. There, the method assumes many frequency dependent variables to be quasi-static within the evaluated bandwidth. Simply put, when this assumption is stretched, the calibration performance suffers.

In this section, a geometry-informed method is used to enable de-embedding of scattered paths. The basic principle of this approach is as follows. If the equivalent geometry of the multipath environment can be identified and modelled, then the spatial aspect of the multipath channel response can be simulated. In doing so, only the coefficients $c_{\mathrm{refl},p}$ and $c_{\mathrm{scat},q}$ for all P and Q number of reflectors and point scatterers remain unknown of the multipath channel response. Expression of the multipath channel response is shown again in Equations 4.34 - 4.37 for the convenience of the readers. Moreover, since these coefficients represent variables with bounded values in magnitude and phase, then an optimization approach can be used to solve for these coefficients. If this is successful, the measured field vector data can be de-embedded from multipath effects to the yield excitation error of the APAA.

$$\mathbf{h}_{\mathrm{propagation}} = h_{\mathrm{LoS}}\mathbf{a}_{\mathrm{LoS}} + \sum_{p=1}^{P} h_{\mathrm{refl},p}\mathbf{a}_{\mathrm{refl},p} + \sum_{q=1}^{Q} h_{\mathrm{scat},q}\mathbf{a}_{\mathrm{scat},q} \tag{4.34}$$

$$h_{\text{LoS}} = h_{\text{fs}} = \frac{c}{f}\frac{1}{4\pi r_{\text{rx,tx}}} e^{-\mathrm{j}\frac{2\pi f r_{\text{rx,tx}}}{c}} \tag{4.35}$$

$$h_{\text{refl},p} = c_{\text{refl},p}\left(\frac{c}{f}\frac{1}{4\pi r_{\text{refl},p}} e^{-\mathrm{j}\frac{2\pi f r_{\text{refl},p}}{c}}\right) \tag{4.36}$$

$$h_{\text{scat},q} = c_{\text{scat},q}\left(\frac{c}{f}\frac{1}{(4\pi)^{\frac{3}{2}} r_{\text{scat-}q\text{,tx}} r_{\text{rx,scat-}q}} e^{-\mathrm{j}\frac{2\pi f r_{\text{scat},q}}{c}}\right) \tag{4.37}$$

Flow diagram of this method is shown in Figure 4.3. Overall, the method can be split into two parts. In the first part, initialization, objects are defined based on the known measurement geometry. This includes not only information of the array dimensions and the position of the beacon, but also the scatterers of interest, which are modeled as either specular reflectors or point scatterers. The following bulleted list summarizes the defined objects and their parameters, corresponding to geometric or EM properties.

- Antenna array: coordinates; array size; inter-element distance; orientation; element radiation pattern, approximated as $\cos\phi$;
- Beacon: coordinates; radiation pattern (modeled as isotropic radiator);
- Specular reflector: coordinates; length; width; orientation; coefficient (modeled as a variable, $c_{\text{refl},p}$);
- Point scatterer: coordinates; coefficient (modeled as a variable, $c_{\text{scat},q}$);

From these geometric and EM parameters, the objects within the ray-tracing physics model can be generated, shown in Figure 4.4. First, using image theory, "image" beacons are generated based on the planar geometry of the specular reflectors. Next, the "visibility" of these image beacons to array elements and point scatterers are checked through ray-tracing vector operations. Based on the visibility, an appropriate mask – with value of 0 or 1 – is applied for each signal path. With all beacons – true or imaginary – accounted for, the channel response of the model are calculated. First, signal path distances r are evaluated through vector operation of object coordinates. This includes paths that go directly from beacons to the array and scattered paths which interact with the point scatterers. Based on these signal path distances, the the frequency-dependent multipath channel response can be calculated using Equations 4.34 - 4.37. As seen in Table **??**, the radiation patterns of the array elements are modeled the q-th power of a cosine function as a simplification to the radiation characteristic of a patch antenna element. Meanwhile, the calibration beacon is modeled simply as an isotropic radiator. Finally, an initial guess of the coefficients $c_{\text{refl},p}$ and $c_{\text{scat},q}$ are used. These coefficients, which will be later used as the optimization variables, are modeled as static coefficients that are frequency independent. Clearly, the simplified nature of some of the aforementioned properties represent a room for improvement for future works.

With regards to the geometry information, of course, it is impossible to have a satisfactory accuracy of the exact positions of the objects, especially when considering the phase rotation factors $e^{-\mathrm{j}2\pi f[\dots]}$. Conveniently, compensation of these initial guess errors can be lumped into the optimization of the $c_{\text{refl},p}$ and $c_{\text{scat},q}$ coefficients later in the optimization part.

Next, to validate the modeled echoic environment, measurement of the PDP of the environment can be done. To make the most comparable assessment, the measurement setup of the PDP measurement should be as identical as possible to the frequency diversity measurements. The resulting PDP data can be directly compared to the extracted impulse response of the multipath channel. Based on this comparison, small adjustment can be made to the object parameters of the model. For example, adjusting the positions of the objects to align the excess delay of scattered path signal components, or adjusting the magnitude of the

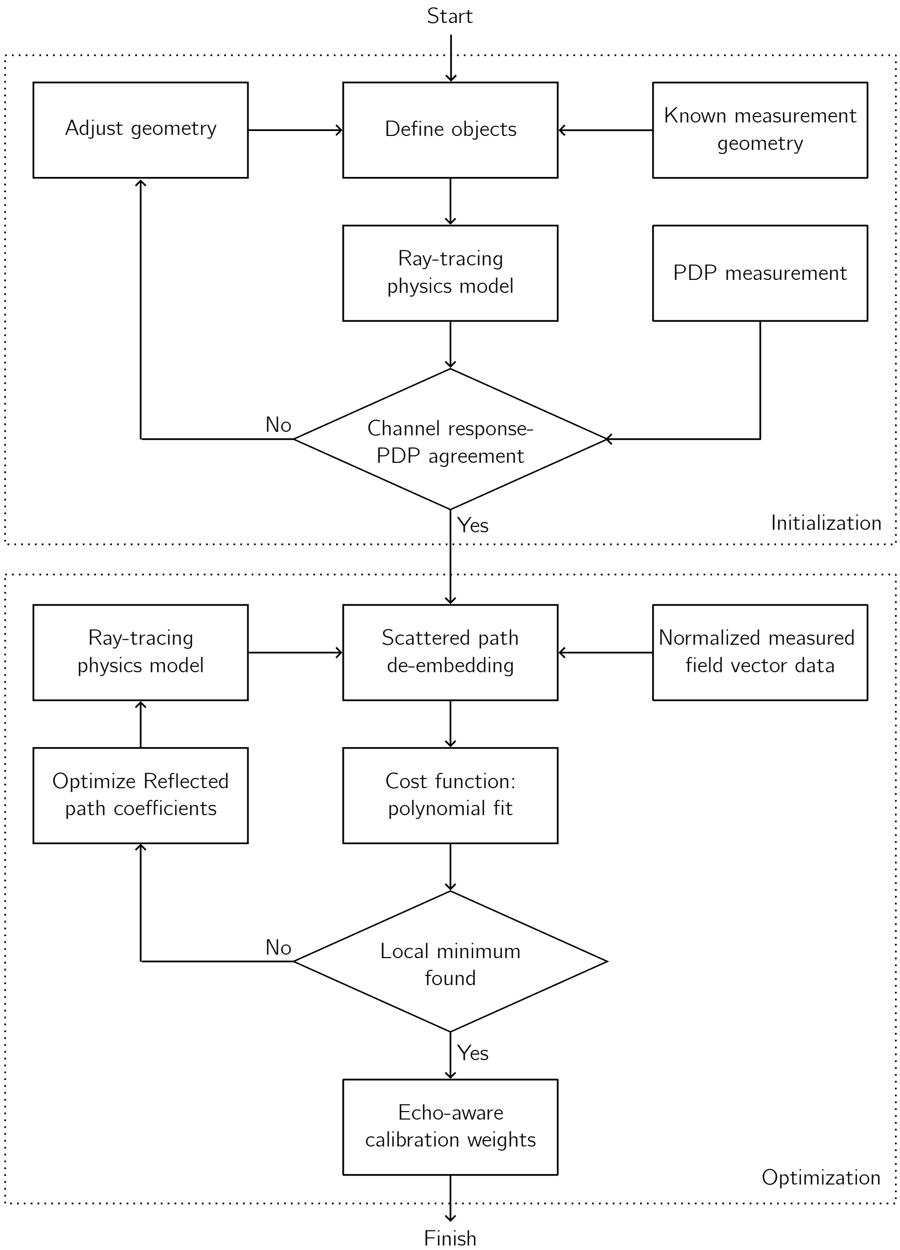

Figure 4.3: Step-by-step procedure of the proposed GIED method.

$c_{\text{refl},p}$ and $c_{\text{scat},q}$ coefficients to better align their magnitudes. These adjustments are illustrated in Figure 4.5.

As seen in Figure 4.3, the optimization part of this method begins with the de-embedding of the scattered paths. In principle, the de-embedding process is simply an element-wise division of the measured field vector by the multipath channel response, all normalized to the reference channel. Deriving from Equation 4.1, rewritten in Equation 4.38 in normalized terms for the n-th channel, the de-embedded excitation error can

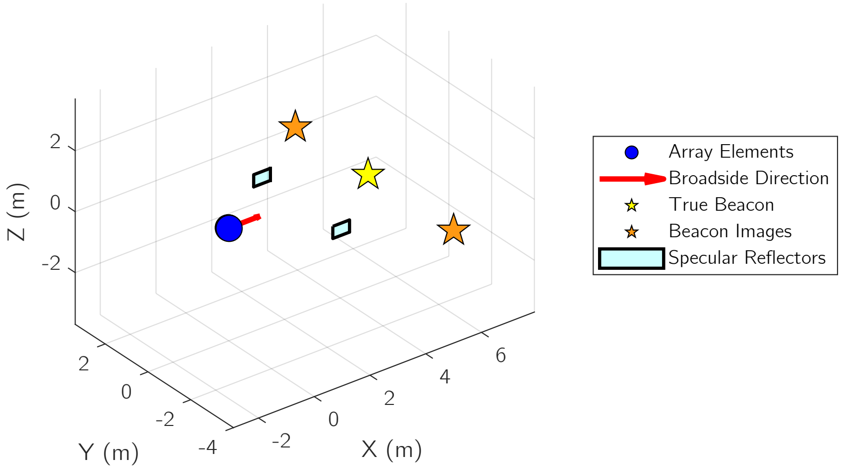

Figure 4.4: Illustration of a ray-tracing model to generate the multipath channel response. In this case, the multipath behavior is introduced by two specular reflectors on either side of the LoS signal path.

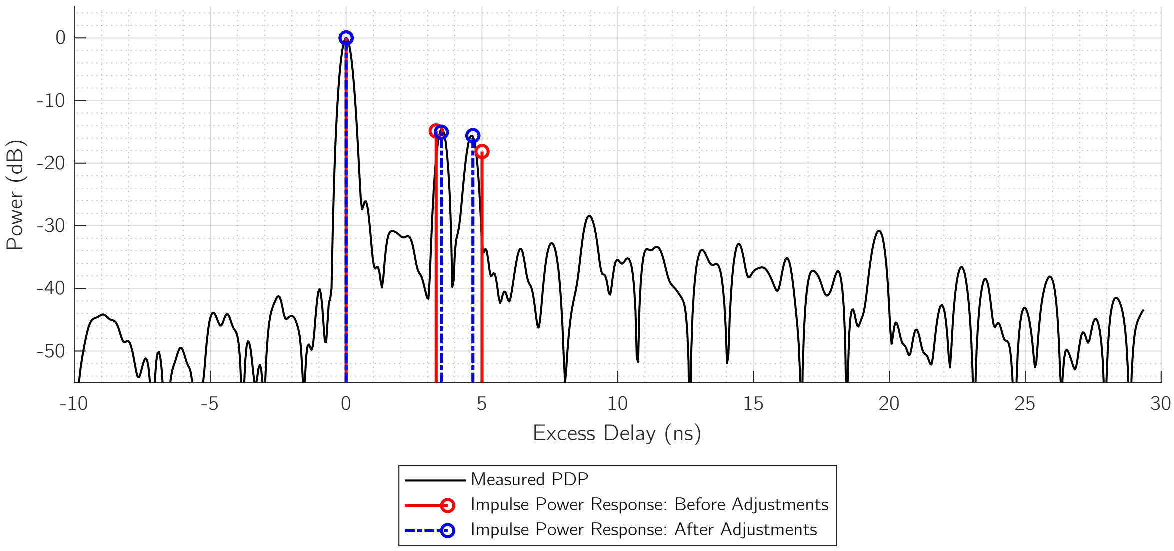

Figure 4.5: Comparison between the impulse response of the generated model to the measured PDP measurement of the echoic environment. Adjustments in the signal component excess delay and the magnitude can be made by modifying the geometries and coefficients used in the model.

easily be retrieved. Again, normalization is done to the 1-st channel as the reference. As the multipath channel response is an estimate, the element-wise ratio represents an unrefined approximation of the excitation error. The tilde notation $\widetilde{[...]}$ is used in Equation 4.39 to show this distinction.

$$E_{\text{norm},n} = \frac{E_n}{E_1} = \frac{h_{\text{propagation},n} w_{\text{err},n}}{h_{\text{propagation},1} w_{\text{err},1}} \tag{4.38}$$

$$\tilde{w}_{\text{err,norm},n} = \frac{\tilde{w}_{\text{err},n}}{\tilde{w}_{\text{err},1}} = E_{\text{norm},n} \frac{\tilde{h}_{\text{propagation},1}}{\tilde{h}_{\text{propagation},n}} \tag{4.39}$$

The variable $E_{\text{norm}n}$ again represents the frequency diversity information, measured according to frequency resolution Δf and bandwidth $B = (L-1)\Delta f$, identical to that found in Section 4.2. As a result, $E_{\text{norm}n}$ will have a dimension of $N \times L$, where N and L are the number of channels in the array and the number frequencies measured for frequency diversity.

In order to evaluate the approximation of the excitation error, a cost function is chosen. The key to choosing the best cost function is to choose that which provides the best distinction of frequency dependent behavior due to multipath and that due to the typical RF channel behavior. As discussed in earlier chapters, the excitation error is directly linked to nonideal effects present in the signal path. Of course, in this context, its frequency-dependent behavior is the most relevant.

Considering the narrow operational fractional bandwidth of around 5%, from 10.0 - 10.5 GHz, the chosen cost function shall be the polynomial fit of the estimated excitation error: 1st order in phase; 2nd order in magnitude. The explanation of these choices follow the underlying physics of the RF signal path. Firstly, the frequency behavior of the phase response must be affected by the time τ needed for the signal to traverse the physical length of the signal path, a phenomena referred to as the group delay. The mathematical expression is shown in Equation 4.40, which is a linear equation, hence the 1st order polynomial fitting.

$$\Phi(f) = -2\pi f \tau + \Phi_0 \tag{4.40}$$

The 2nd order polynomial is deemed a good fit for the frequency behavior of the magnitude response due to the hardware makeup of the RF channel, which includes an RF amplifiers, band-pass filters, patch antennas, etc. Over the narrow 500 MHz operational bandwidth, the pass-band responses of these devices typically assume a smooth, arc-like curve shape.

Overall, the cost function and the master objective function of the proposed method are expressed in mathematical notations in Equations 4.41 and 4.42. The optimal parameter $\mathbf{x}^*$ is found by optimizing the ℓ_1-norm of the difference between the raw estimated excitation error $\tilde{\mathbf{w}}_{\text{err,norm}}$ and the polynomial-smoothed excitation error $\hat{\mathbf{w}}_{\text{err,norm}}$ across frequencies. The ℓ_1-norm is used for the cost function to avoid excess distortion from quantization noise.

$$\mathcal{J}(\mathbf{x}) = \sum_{n=1}^{N} \sum_{m=1}^{L} |\tilde{w}_{\text{err,norm},n}(f_m; \mathbf{x}) - \hat{w}_{\text{err,norm},n}(f_m; \mathbf{x})| \tag{4.41}$$

$$\mathbf{x}^* = \arg\min_{\mathbf{x}\in\Omega} \mathcal{J}(\mathbf{x}) \tag{4.42}$$

While 0-based indexing ($k \in \{0, ..., L-1\}$) was used in Section 4.2 to denote discrete FT bins, here, 1-based indexing ($m \in \{1, ..., L\}$) is adopted to represent discrete measurement points along the frequency sweep for least-squares regression.

As discussed previously, the state vector $\mathbf{x}$ corresponds to the physics-related $c_{\text{refl},p}$ and $c_{\text{scat},q}$ coefficients, but is de-coupled into their magnitude and phase components. In total, the state vector $\mathbf{x}$ has a length of

$2(P+Q)$, where P and Q are the total number of specular reflectors and point scatterers in the modeled echoic environment.

$$\mathbf{x} = [\ldots, |c_{\text{refl},p}|_{\text{dB}}, \angle|c_{\text{refl},p}, \ldots, |c_{\text{scat},q}|_{\text{dB}}, \angle|c_{\text{scat},q}, \ldots]^T \tag{4.43}$$

As seen in Equation 4.42, the optimization vector $\mathbf{x}$ is bounded to the parameter space Ω. Equation 4.44 describes the box-like bounds. Every complex coefficient's magnitude and phase are strictly enforced as $|c|_{\text{dB}} \in [-40, 0]$ and $\angle c \in [-180°, 180°]$. While the phase bounds are self-explanatory, the magnitude bounds assume all reflectors and scatterers as passive, non-focusing objects, thus the upper bound of 0 dB.

$$\Omega = \left\{ \mathbf{x} \in \mathbb{R}^{2(P+Q)} \;\middle|\; \mathbf{x}_{\text{lb}} \leq \mathbf{x} \leq \mathbf{x}_{\text{ub}} \right\} \tag{4.44}$$

To calculate the cost function, as mentioned previously, the raw excitation error is decoupled into its magnitude and phase components. Then, polynomial regression is applied to both components to obtain $\hat{w}_{\text{err,norm},n}$. This process is shown in Equations 4.45 - 4.49.

$$\tilde{A}_n(f_m; \mathbf{x}) = |\tilde{w}_{\text{err,norm},n}(f_m; \mathbf{x})| \tag{4.45}$$

$$\tilde{\Phi}_n(f_m; \mathbf{x}) = \mathcal{U}\{\angle \tilde{w}_{\text{err,norm},n}(f_m; \mathbf{x})\} \tag{4.46}$$

where $\mathcal{U}\{\ldots\}$ is the 2π unwrapping operator.

$$\hat{A}_n(f_m; \mathbf{x}) = \mathcal{P}_2\{\{\tilde{A}_n(f_i; \mathbf{x})_{i=1}^{L}\}\}(f_m) \tag{4.47}$$

$$\hat{\Phi}_n(f_m; \mathbf{x}) = \mathcal{P}_1\{\{\tilde{\Phi}_n(f_i; \mathbf{x})_{i=1}^{L}\}\}(f_m) \tag{4.48}$$

where $\mathcal{P}_d\{\{y_i\}\}(f)$ denotes the evaluation of the d-th order least-squares polynomial fitted to data sequence $\{y_i\}$ at frequency f.

The magnitude and phase components are recombined to form the polynomial-fitted excitation error.

$$\hat{w}_{\text{err,norm},n}(f_m; \mathbf{x}) = \hat{A}_n(f_m; \mathbf{x}) \cdot e^{j\hat{\Phi}_n(f_m; \mathbf{x})} \tag{4.49}$$

The bounded objective function found in Equation 4.42 is solved numerically using the `fmincon` solver from the MATLAB Optimization Toolbox. The sequential quadratic programming (SQP) is used as the optimization algorithm. When the objective function is non-decreasing to within the value of optimality tolerance, the optimization is completed. The best estimation of the excitation error, $\tilde{w}_{\text{err,norm},n}(f_m; \mathbf{x}^*)$, is obtained.

To give an idea of the optimization performance, the optimization done for experiments in Section 4.4.3, which optimizes for two specular reflector objects (4 variables in total), needed 40 iterations to converge with a total runtime of around 3 seconds.

4.4. Proof-of-concept experiments

To prove that the proposed frequency diversity methods are capable of combating the multipath effects of the echoic environment, some proof-of-concept experiments are in order. Several scenarios are prepared. In the first scenario, the APAA is measured in an anechoic chamber to obtain a reference set of data. Next, a metal reflector panel introduced to simulate the simplest echoic environment. Finally, in the third scenario, two reflector panels are introduced to increase the multipath complexity. However, due to schedule conflicts regarding the anechoic chamber and lack of time, two-reflector scenario was done in a typical echoic lab.

For all measurements, the SCSNS technique is used. This includes measurements used to collect data on which the FDA and GIED methods are apllied. Selection of this technique is for its measurement speed and calibration performance, as demonstrated in Section 2.1 and 3.2 respectively. Since all methods evaluated here utilize the same basic calibration technique, this is a special case whereby comparison of calibration through statistical description (in this case SD) of calibration error remain valid. That being said, pattern-derived metrics results remain shown where additional insights can be obtained.

4.4.1. Reference scenario

As in conventional APAA calibration literature, the DUT is measured in a reference scenario where conventional techniques are used. In this case, the reference scenario refers to calibration in an anechoic environment. The measurement setup is that of a typical setup involving phaseless techniques, identical to that shown in Figure 2.1, presented again for convenience in Figure 4.6. Photograph of the measurement setup can be seen in Figure A.2.

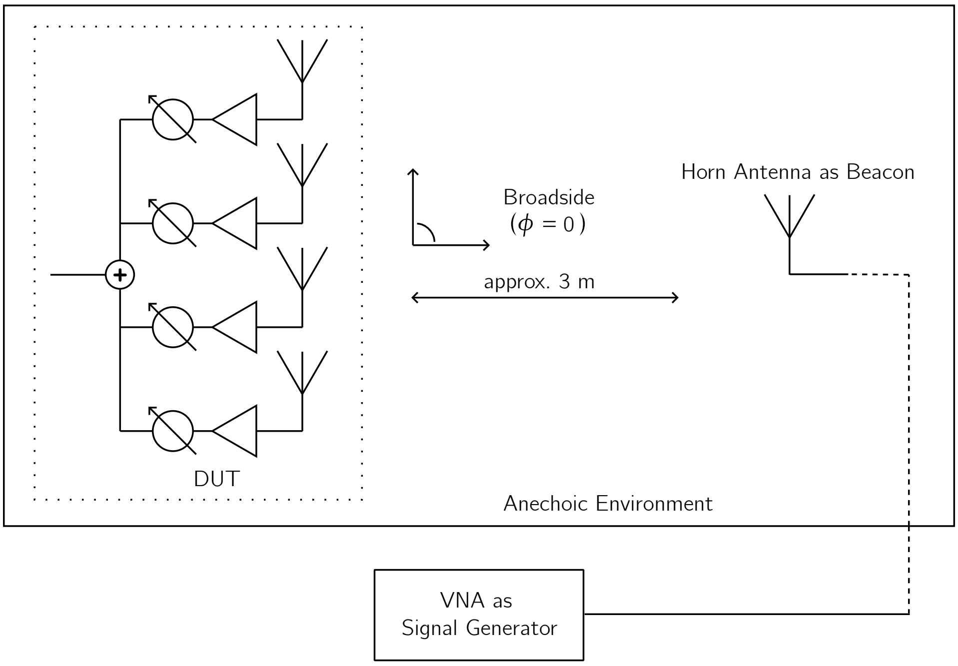

Figure 4.6: Measurement setup for the proof-of-concept experiment in the reference scenario.

The purpose of this reference scenario measurement is two fold. First, it allows direct comparison of channel response, which is what is typically found in the literature when calibration performance is being compared. The second – and main purpose of this measurement – is to estimate the excitation error of each channel so that AF patterns can be derived from the obtained measurement data in the following subsections. This information is needed since EQ pattern measurements cannot be performed due to schedule conflicts and lack of time to make those measurements. As such, pattern-derived metrics are obtained through AF patterns instead.

Due to the conventional nature of the measurement setup, the DUT's excitation error can be measured by simply recording the normalized field vectors $\mathbf{E}_{\text{norm}}$ present on each channel due to the calibration beacon. Here, this process is done by utilizing the SCSNS technique without further treatment. To obtain the maximum available frequency diversity information while limiting the measurement time to a reasonable duration, measurements are done for the entirety of the DUT's operating frequencies, 10.0 - 10.5 GHz, with 10 MHz spacing. In total, this yields 51 frequency data points and 4×2 spatial data points – one for each channel from the DUT's two subarrays. Figures 4.7 and 4.8 shows the measured excitation error for each channel. As seen in the figures, the DUT's 2nd channels are used as the reference channel due to it being closer to the subarray's center.

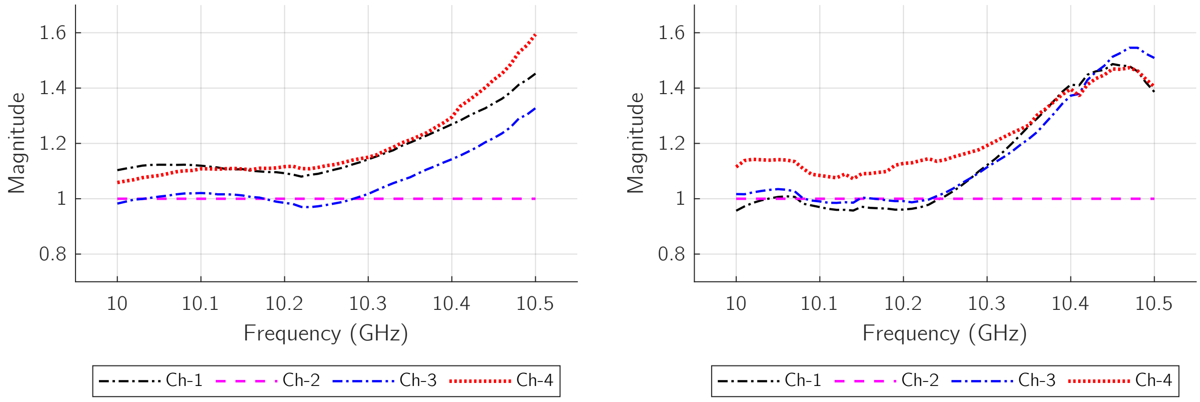

(a) Subarray-1. **(b)** Subarray-2.

Figure 4.7: Magnitude of the excitation error when measured in the reference scenario.

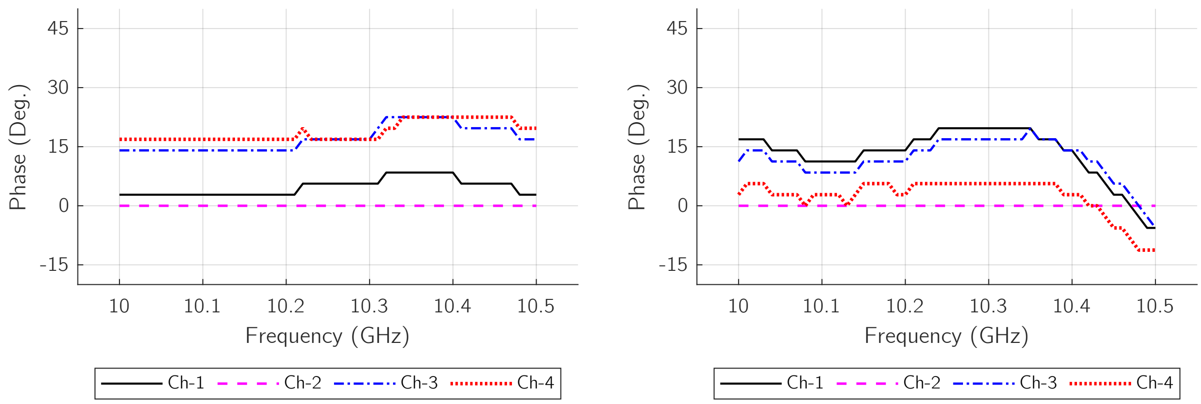

(a) Subarray-1. **(b)** Subarray-2.

Figure 4.8: Phase of the excitation error when measured in the reference scenario.

4.4.2. Single-reflector scenario

In this scenario, the simplest multipath scenario is evaluated by adding a metal reflector panel to the anechoic chamber, the photograph of which can be seen in Figure A.2b. First, the reflector panel position and alignment are adjusted to ensure a scattered path is created. An online PDP measurement using a VNA are kept running as the reflector panel is adjusted as validation. A surrogate antenna is used in place of the DUT to simplify the VNA interfacing. This setup is shown in Figure 4.9a and the resulting PDP measurement is shown in Figure 4.10 – where the scattered path signal component can be observed at 13.24 ns, around 3.17 ns after the LoS signal component.

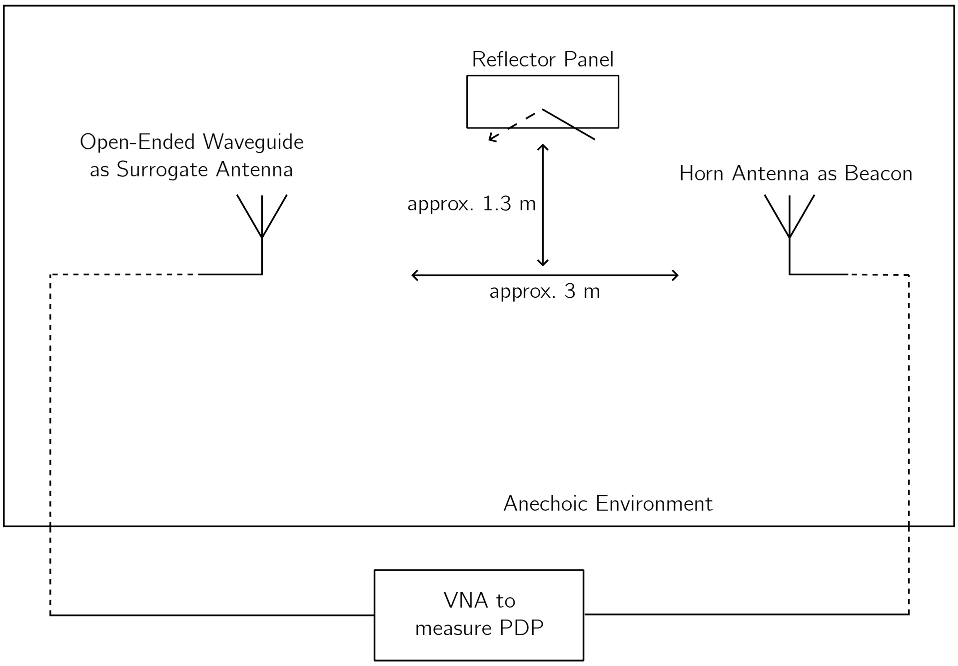

(a)

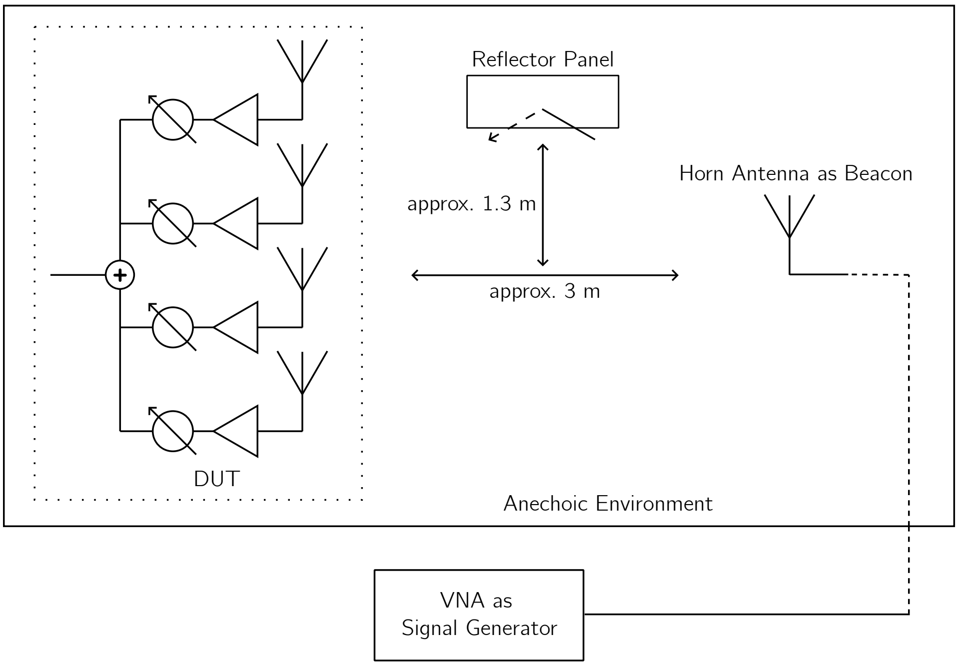

(b)

Figure 4.9: Measurement setup for the proof-of-concept experiment in the single-reflector scenario: (a) PDP measurement to ensure existence of the scattered path due to the reflector panel; (b) the surrogate antenna is replaced for the DUT to do calibration. The horn antenna is kept at the broadside direction of the surrogate antenna/DUT, and the reflector panel is placed halfway between the beacon and the surrogate antenna/DUT.

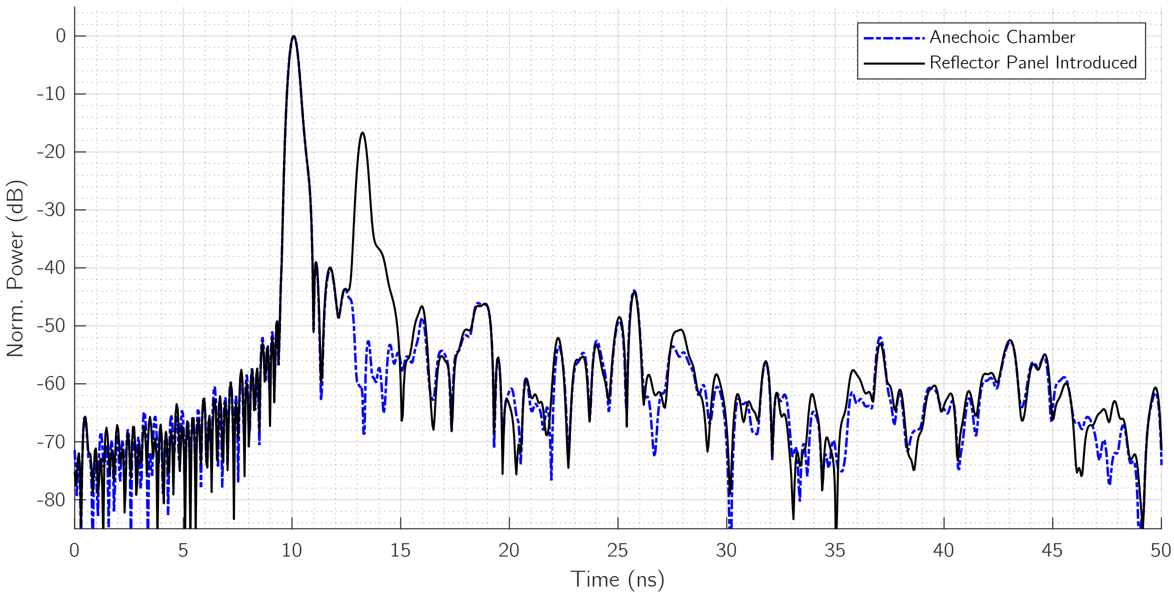

Figure 4.10: The PDP measurement obtained from the proof-of-concept experiment in the single-reflector scenario.

Next, the frequency diversity information is recorded through measurement using the DUT. So, after the PDP measurement shows a scattered path signal component, the surrogate antenna is switched out with the DUT and the VNA is now utilized as a signal generator of the calibration beacon. The measurement setup is shown in Figure 4.9b. With the switch, multipath channel response experienced by the DUT will not be identical to that of the surrogate antenna, since there is discrepancy in the antenna radiation pattern. However, since the DUT is placed in exact same location as the surrogate antenna, the existence of the scattered path will persist for the DUT.

From the obtained data, through post-processing, the proposed frequency diversity methods are applied to all 51 frequency data points. Figures 4.11 and 4.12 compares the results obtained from the proposed methods as well as results obtained from the conventional method – that is the SCSNS technique without any additional steps. Mathematically, these plots show calibration error $\mathbf{w}_{\text{cal,err}}$, which are simply the product of the excitation error – obtained from Subsection 4.4.1 – and the calibration weights – obtained through application of the proposed frequency diversity methods. A perfect calibration would correspond to a calibration error $w_{\text{cal,err},n}$ of 1.

$$\mathbf{w}_{\text{cal,err}} = \mathbf{w}_{\text{cal}} \odot \mathbf{w}_{\text{err}} \tag{4.50}$$

As seen from Figures 4.11 and 4.12, applying calibration weights obtained from a conventional method in an echoic environment would yield a wildly erroneous calibration. In comparison, **the proposed methods are able to greatly improve on the conventional method**. Statistically, the conventional method yields 2.088 dB and 9.85° in magnitude and phase SD. In comparison, FDA yields 0.989 dB and 3.36°, while GIED yields 0.363 dB and 3.19°. Statistically, the GIED outperforms all its competitors here.

To better contextualize the results, the acquired calibration weights are used to derive AF patterns, from which pattern-derived metrics are obtained. However, as is known, the DUT are built in a hybrid architecture which requires calibration between the two subarrays to equalize their weights. However, due to time constraints, this routine has not been implemented and the corresponding data has not been measured. As an alternative,

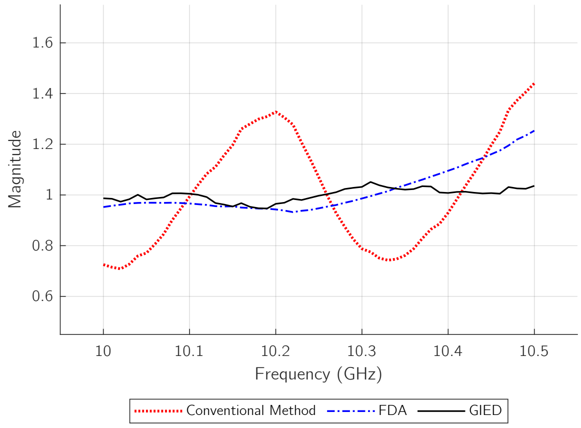

(a) Subarray-1, channel-1.

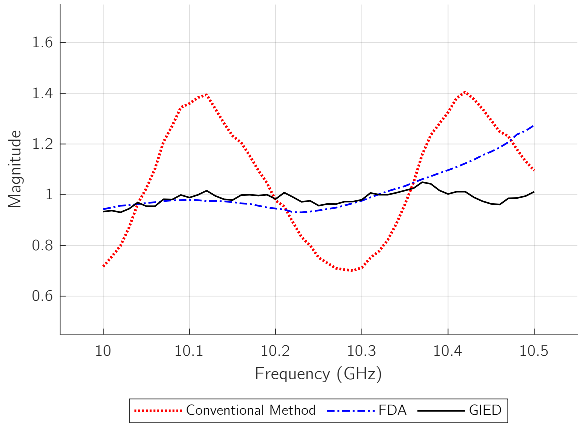

(b) Subarray-1, channel-3.

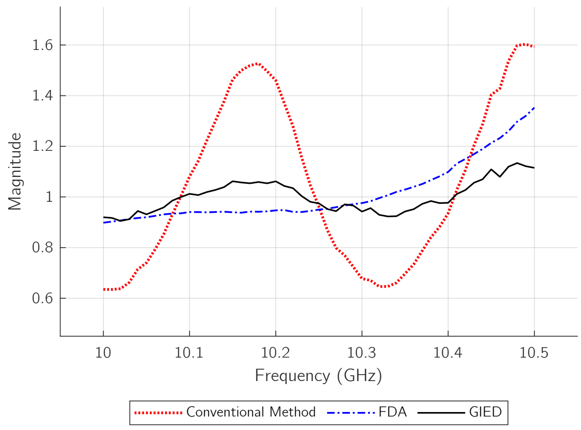

(c) Subarray-1, channel-4.

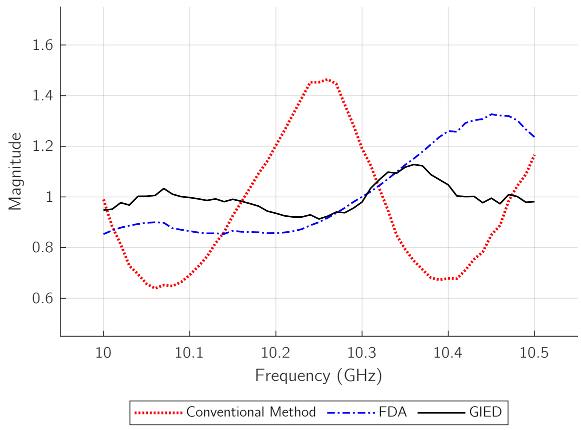

(d) Subarray-2, channel-1.

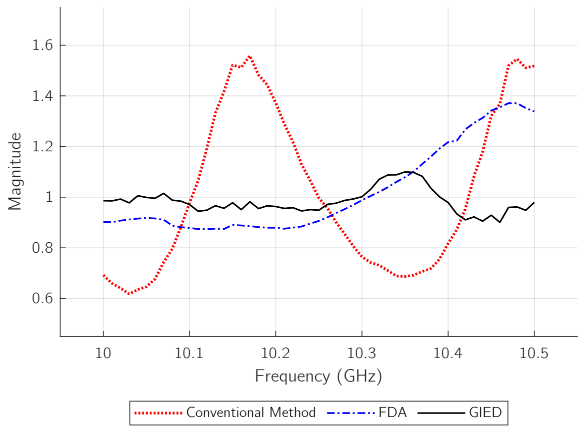

(e) Subarray-2, channel-3.

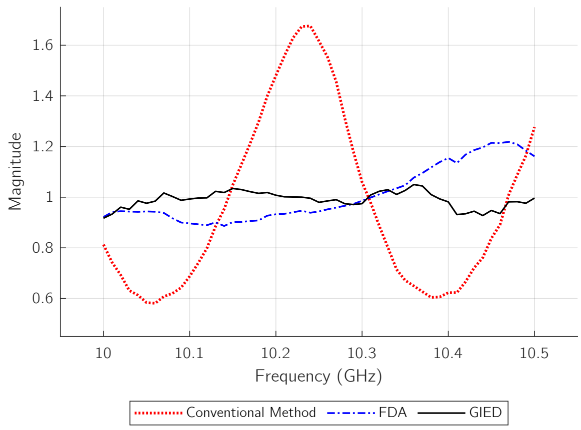

(f) Subarray-2, channel-4.

Figure 4.11: Magnitude of the calibration error when the proposed frequency diversity methods are applied in the 1-reflector scenario.

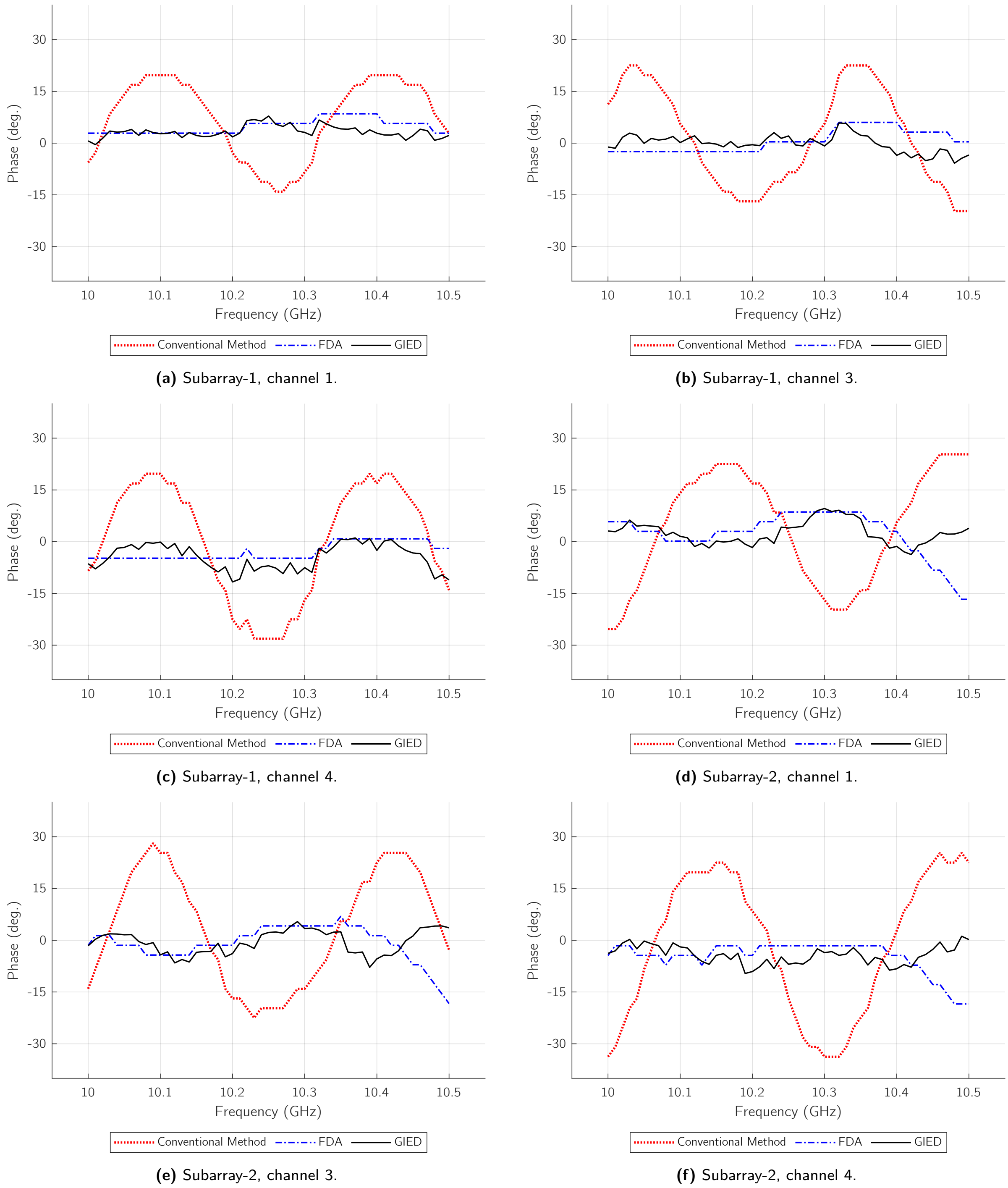

(a) Subarray-1, channel 1.

(b) Subarray-1, channel 3.

(c) Subarray-1, channel 4.

(d) Subarray-2, channel 1.

(e) Subarray-2, channel 3.

(f) Subarray-2, channel 4.

Figure 4.12: Phase of the calibration error when the proposed frequency diversity methods are applied in the single-reflector scenario.

an idealized simplification is applied. Calibrating coefficients are derived such that the vector sum of the two subarray's magnitude and phase are equalized. Mathematically, the calibrating coefficients are derived and applied as in Equations 4.51 - 4.53, where the (m) superscript denotes the m-th subarray. As an analogy, this idealization assumes perfect calibration between the two subarrays, disregarding any measurement error or multipath effects.

$$\mathbf{c}_{\text{err}} = \begin{bmatrix} \sum_{n=1}^{4} w_{\text{err},n}^{(1)} \\ \sum_{n=2}^{4} w_{\text{err},n}^{(2)} \end{bmatrix} \tag{4.51}$$

$$\mathbf{c}_{\text{cal}} = \max\left(|c_{\text{err},1}|, |c_{\text{err},2}|\right) \cdot \mathbf{c}_{\text{err}}^{\circ -1} \tag{4.52}$$

$$\mathbf{w}_{\text{cal}} = \begin{bmatrix} c_{\text{cal},1}\mathbf{w}_{\text{cal}}^{(1)} \\ c_{\text{cal},2}\mathbf{w}_{\text{cal}}^{(2)} \end{bmatrix} \tag{4.53}$$

With the calibration weights across the subarrays are artificially equalized, AF patterns can be synthesized. As excitation of the n-th channel, the calibration error $w_{\text{cal,err},n}$ is applied. Ideally, the pattern will result in a steered beam at broadside direction with no magnitude tapering. Then, repeating the method used in Chapter 3, pattern-derived metrics are obtained. The resulting metrics are plotted in Figures 4.13 - 4.15.

Again, a recurring theme is observed, where the pattern-metrics obtained from the proposed methods outperforms those obtained from the conventional method. Furthermore, **in terms of the pattern RMSE, the GIED method also appears to outperform other methods here, consistent with the previous calibration SD comparison**, even if its advantage is marginal. **Such results is expected, since the GIED method applied here possesses information on all (of one) scattered paths**. Therefore, de-embedding of all multipath effects is expected.

Lastly, the uncalibrated method, where no calibration routine is applied at all, appears to be competitive here. This is because the DUT's channels already have an acceptable excitation offsets within the subarray, whilst the inter-subarray calibration is assumed to be perfect. In practice, there is significant mis-alignment between the two subarrays. Clearly, this reality has been heavily under-represented in these evaluations.

4.4.3. Two-reflector scenario

Next, the complexity of the multipath effect is increased by introducing an additional reflector panel. Moreover, now, the calibration is performed not in an anechoic chamber, which means the environment is much richer in terms of scattered paths. The measurement setup in this experiment is shown in Figure 4.16 and photographs from the experiment can be seen in Figure A.3. Overall, the experiment procedure and hardware follows that demonstrated in the single-reflector scenario of Subsection 4.4.3: PDP measurement followed by frequency diversity measurements. Later, the proposed frequency methods are applied in post-processing.

Figure 4.17 shows the resulting PDP measurement for the two-reflector scenario. As seen in the plot, the "floor" of the PDP is significantly raised. This is due to the inherently echoic nature of the environment, in contrast with the PDP of the anechoic chamber found in Figure 4.10. From the figure, the LoS signal can be identified at 70.64 ns, while the scattered path signal components due to the placed reflector panels make up the most significant echo of the PDP, identifiable at 74.16 ns and 75.28 ns – corresponding to excess delays of around 3.52 ns and 4.64 ns.

Next, frequency diversity information is gathered through measurement and the proposed methods are applied. Additionally, for further reference, measurement is also done for when the reflector panels are removed – this measurement corresponds to the multipath effect inherent to the environment. The resulting calibration error obtained are shown in Figures 4.18 and 4.19, from which several observations can be made.

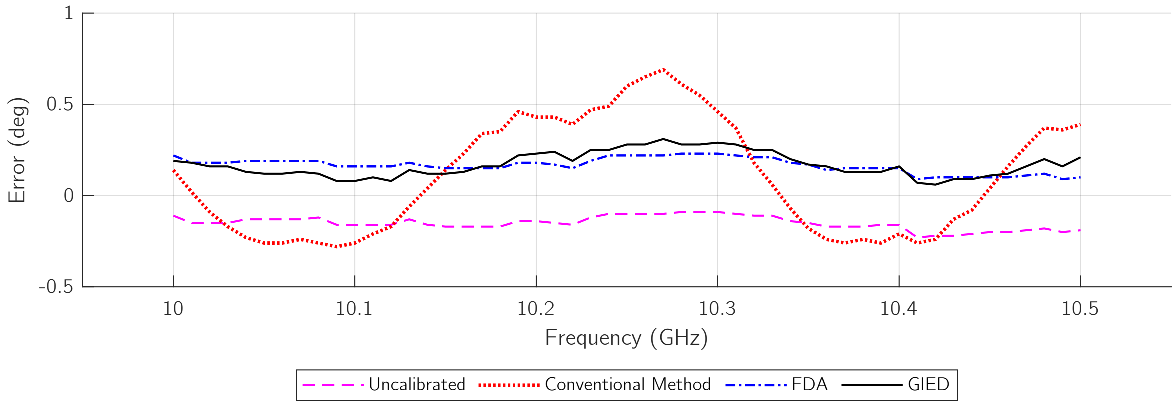

Figure 4.13: Steering angle error found from the AF pattern derived from calibrated excitation weights. Calibration was done in the single-reflector scenario.

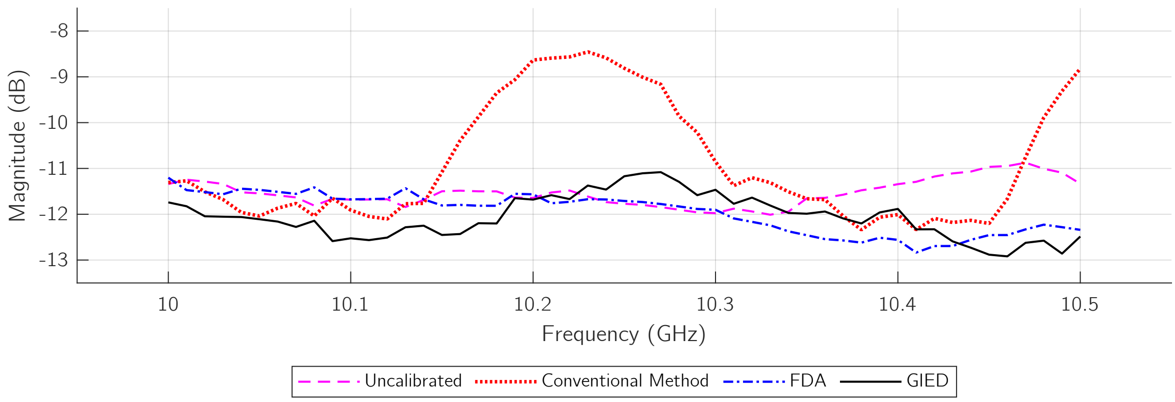

Figure 4.14: Maximum SLL found from the AF pattern derived from calibrated excitation weights. Calibration was done in the single-reflector scenario.

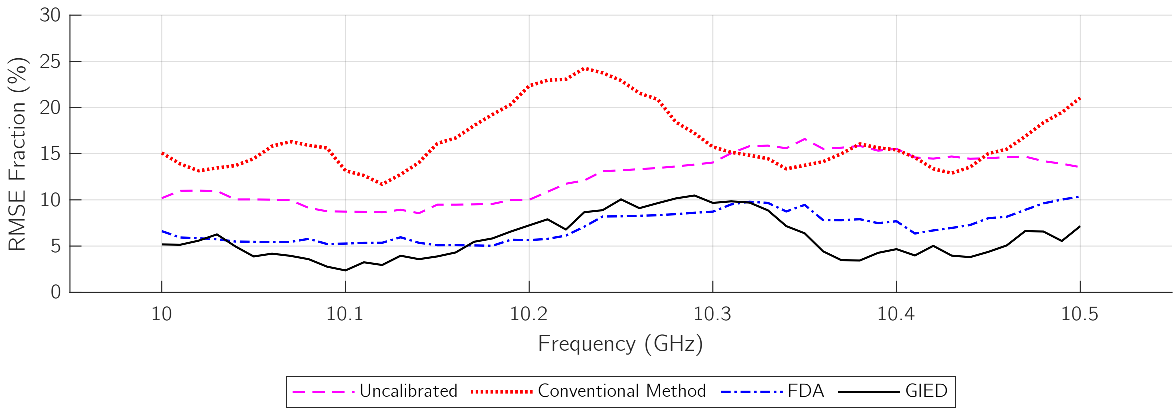

Figure 4.15: Pattern RMSE of the AF pattern derived from calibrated excitation weights. Calibration was done in the single-reflector scenario.

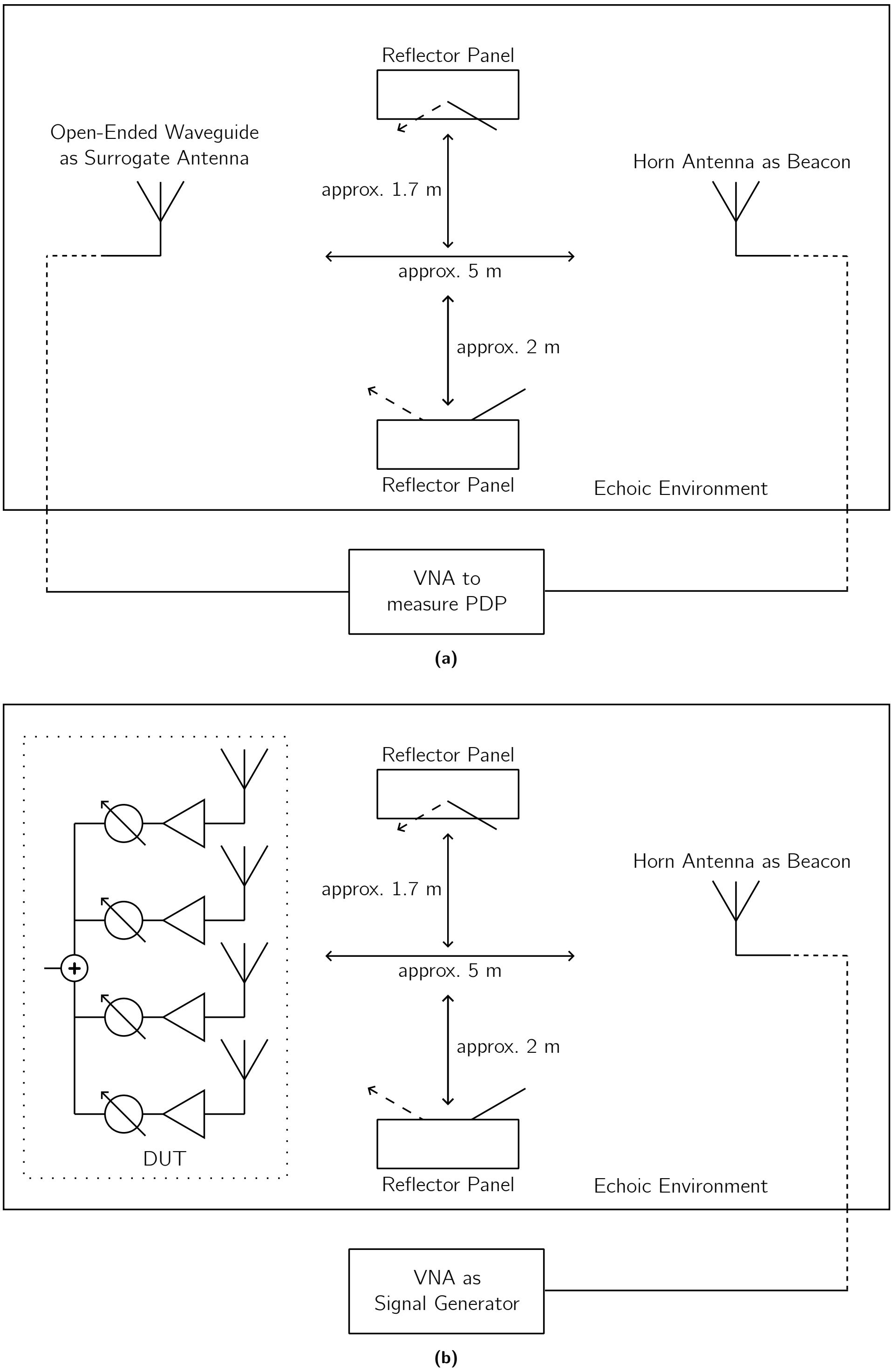

Figure 4.16: Measurement setup for the proof-of-concept experiment in the two-reflector scenario: (a) PDP measurement; (b) frequency diversity measurement of the multipath response to do calibration. The horn antenna is kept at the broadside direction of the surrogate antenna/DUT, and the reflector panels are placed halfway between the beacon and the surrogate antenna/DUT.

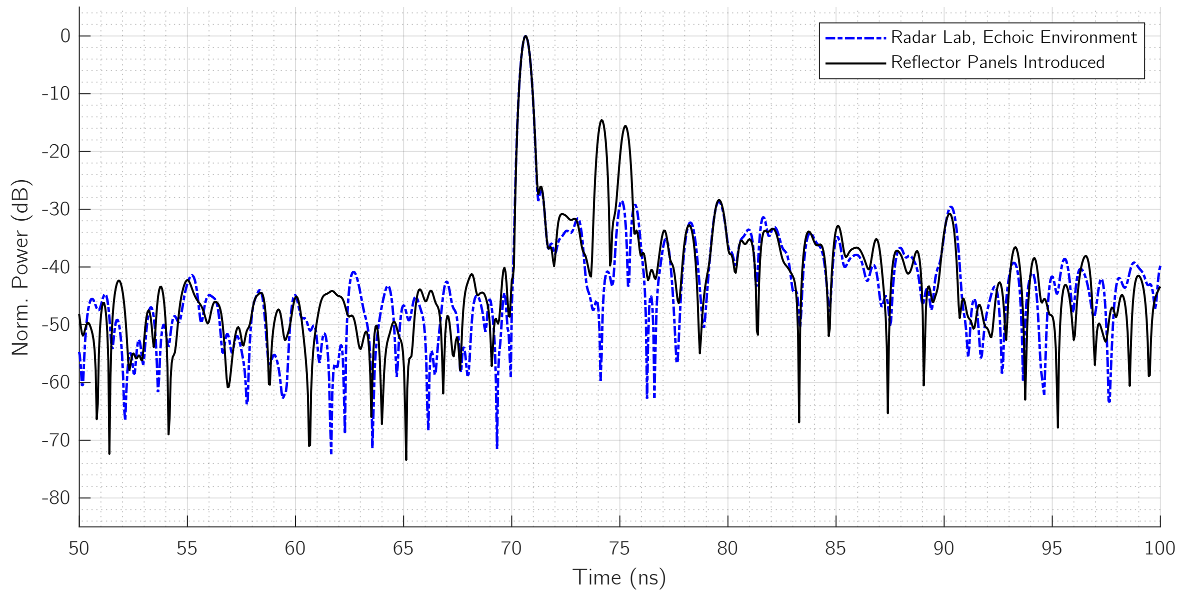

Figure 4.17: The PDP measurement obtained from the proof-of-concept experiment in the two-reflector scenario.

First, it is clear that even without the addition of the reflector panels, the inherently echoic environment has already caused ripples on the calibration weights. By further adding the two reflector panels, without utilizing frequency diversity information, even heavier distortions are observed. On the other hand, when the FDA or GIED methods are applied, the heavy distortions are no longer evident. **For the GIED method, since only the two reflector panels are modeled in the ray-tracing model, the best calibration result can only compensate for the scattered paths created by those two reflector panels**. Meanwhile, the scattered paths created due to the echoic environment itself are uncompensated. This is why similar results are obtained from the GIED method and from the no reflector panel case are very similar.

Conversely, the FDA method require no information of the environment geometry. Its performance are completely determined by its frequency diversity parameters, i.e. bandwidth, frequency resolution, and whether the quasi-static behavior assumption of the channel and the DUT holds. In terms of the magnitude and phase component SDs, the FDA and GIED methods perform very similarly: 0.998 dB and 5.92° compared to 0.592 dB and 6.22°. As comparison, the conventional method in the no reflector and two-reflector scenarios yield 0.447 dB and 2.004 dB in magnitude, and 5.49° and 13.02° in phase SD.

Next, calibration performance is evaluated in terms of pattern-derived metrics, obtained as in Subsection 4.4.2 for the single-reflector scenario. Figures 4.20 - 4.22. These plots confirm that the proposed methods are able to greatly improve the beamforming capabilities of the DUT when compared to conventional methods, compensating for the effect of the most significant scattered paths. **Overall, both proposed methods achieve similar steering angle error and pattern RMSE performance. However, the FDA method performs more stably in terms of maximum SLL than the GIED**, which varies wildly at 10.10 and 10.32 GHz with around -10 dB and -9.5 dB in maximum SLL. On the other hand, the FDA yields larger pattern RMSE at higher frequencies.

Several factors may be at play. First, since the FDA provide a single set of calibration weights across frequencies, the frequency dependency of the calibration performance will depend on how the RF channel's excitation error changes with frequency – which is fairly smooth in this case. Meanwhile, the GIED provides

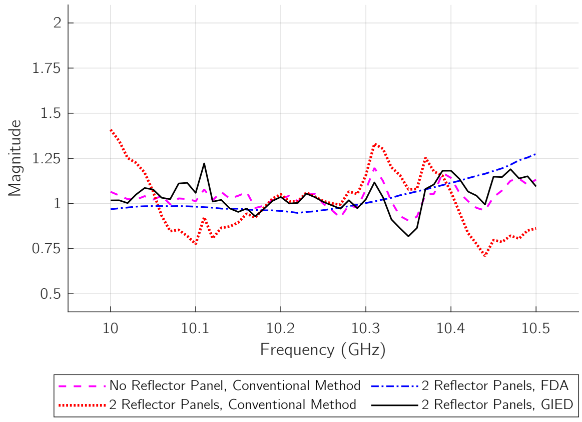

(a) Subarray-1, channel-1.

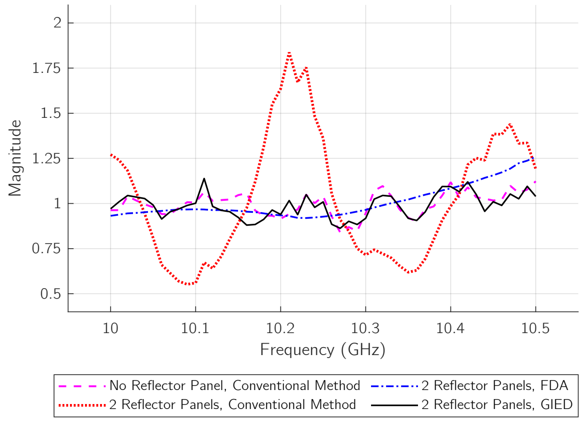

(b) Subarray-1, channel-3.

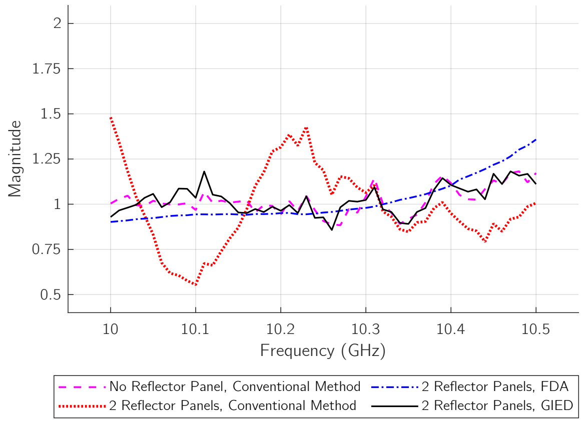

(c) Subarray-1, channel-4.

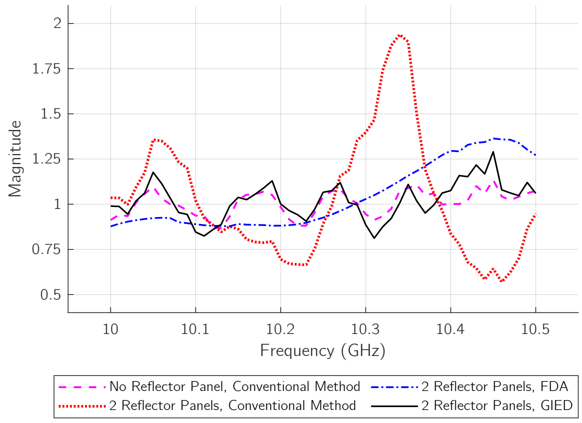

(d) Subarray-2, channel-1.

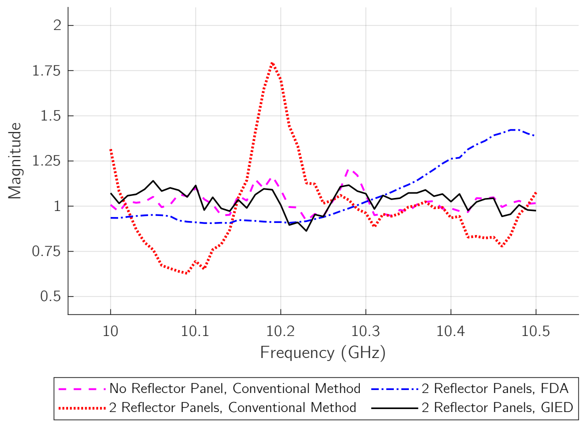

(e) Subarray-2, channel-3.

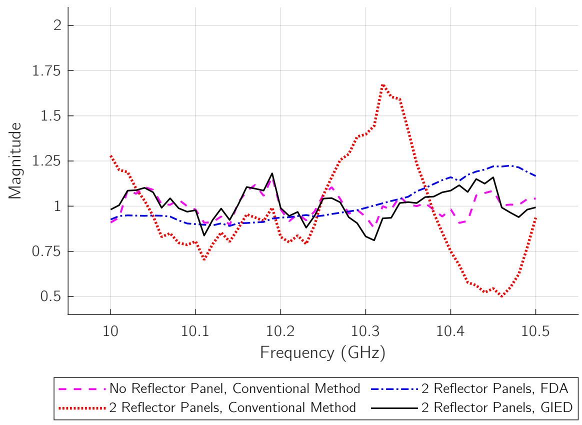

(f) Subarray-2, channel-4.

Figure 4.18: Magnitude of the calibration error when the proposed frequency diversity methods are applied in the two-reflector scenario.

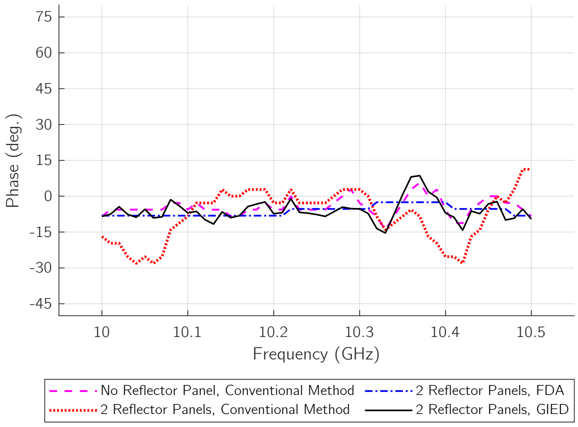

(a) Subarray-1, channel 1.

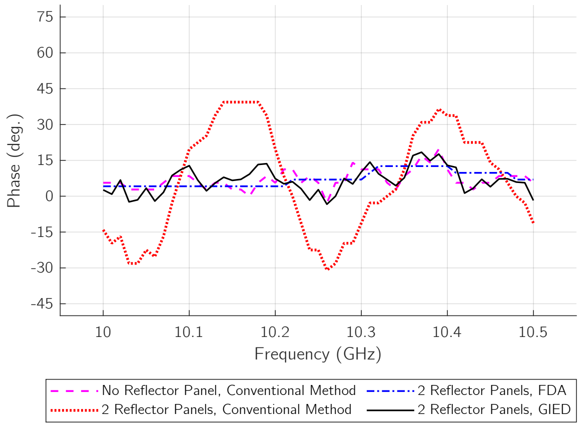

(b) Subarray-1, channel 3.

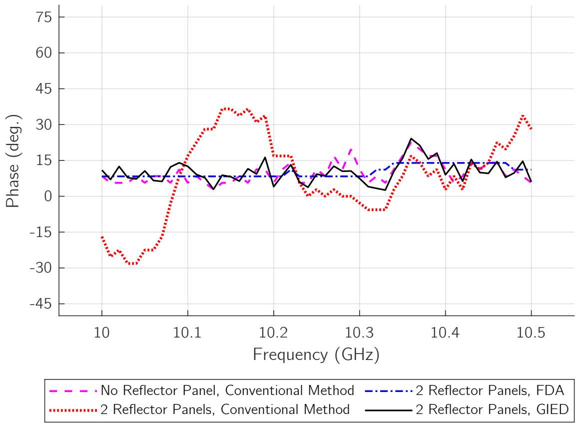

(c) Subarray-1, channel 4.

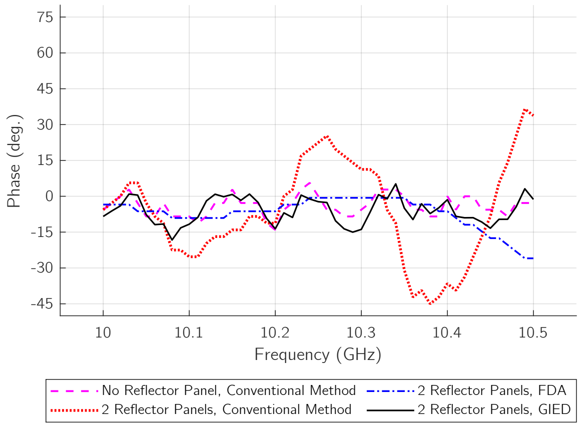

(d) Subarray-2, channel 1.

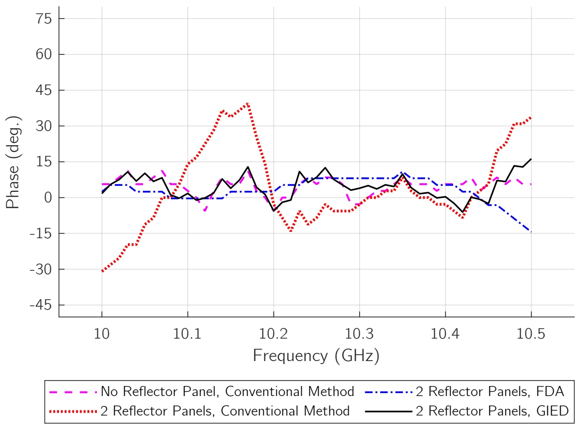

(e) Subarray-2, channel 3.

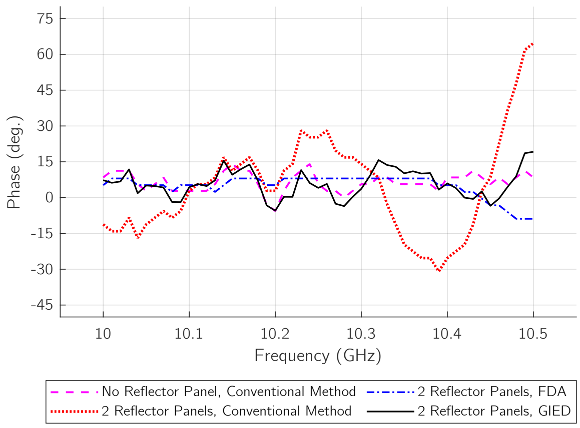

(f) Subarray-2, channel 4.

Figure 4.19: Phase of the calibration error when the proposed frequency diversity methods are applied in the two-reflector scenario.

an optimized matrix of frequency-dependent calibration weights, informed by the environment geometry. However, in this scenario, the implemented GIED method does not account for *all* scattered paths. Moreover, since the de-embedding process is optimized statistically using ℓ_1-norm, the cost function only slightly "punish" the significant offset of a small number of frequency data points. These then translate into deteriorated performance in those data points. **All-in-all, when variability of the frequency behavior is prioritized, the FDA should be preferred to the GIED when insufficient geometry information is known**.

4.5. Frequency diversity parameters

After validating the efficacy of the proposed method, it is interesting to evaluate how frequency diversity parameters affect their performance. Behavior of the FDA method, which is equivalent to taking the 0-th time bin of a frequency domain signal's IFT, is much more predictable in this regard. The relation between frequency parameters and FT/IFT operations are well studied, some of which are described in Section 4.2. On the other hand, how the same parameters affect the GIED method is not known. In this section, post-processing on data collected from proof-of-concept experiments of Section 4.4 are extended by varying the amount and selection of the frequency diversity information used for the proposed methods. In doing so, the effect of frequency parameters on calibration performance of the proposed methods can be evaluated.

4.5.1. Frequency resolution and bandwidth

Consider the measured frequency diversity information with frequency resolution Δf_{meas} with L_{meas} number of data, accumulating a total bandwidth $B_{\text{meas}} = (L_{\text{meas}} - 1)\Delta f_{\text{meas}}$. The frequency diversity parameters to be evaluated in this section are k and L, which corresponds to the data sampling interval and the number of frequency data points actually utilized in the proposed methods. Their relations to the frequency diversity parameters Δf and B are described as in Equations 4.54 and 4.55.

$$\Delta f = k\Delta f_{\text{meas}} \tag{4.54}$$

$$B = (L-1)\Delta f = (L-1)k\Delta f_{\text{meas}} \tag{4.55}$$

In other words, the results obtained in the proof-of-concept experiments of Section 4.4 utilizes the entirety of the frequency diversity information, where k and L are 1 and 51 respectively, i.e. $\Delta f = \Delta f_{\text{meas}}$ and $B = B_{\text{meas}}$. Next, the variables k, L will be varied.

In order to analyze the results more easily, data obtained from the simplest echo environment scenario is chosen, in this case the single-reflector scenario of Subsection 4.4.2. Then, the data are sampled according to valid k, L parameters. The requirements for valid k, L parameters are as follows.

- k, L are positive integers;
- The set of utilized data points governed by k, L must be a subset of the measured data points, i.e. $k(L-1) \leq L_{\text{meas}}$;
- The utilized bandwidth center is always at 10.25 GHz. In other words, the median of all the utilized data points' indexes are always 26 – which corresponds to data at 10.25 GHz.

While the first and second items of the above requirements are trivial, the third are enforced for the convenience of the analysis. Since the center frequency being evaluated is kept constant, comparison between results from different k, L is much more relevant.

Next, the FDA and GIED methods are applied to frequency data sets administered by the valid k, L values, thereby obtaining their corresponding calibration weights and their corresponding calibration error. The SD

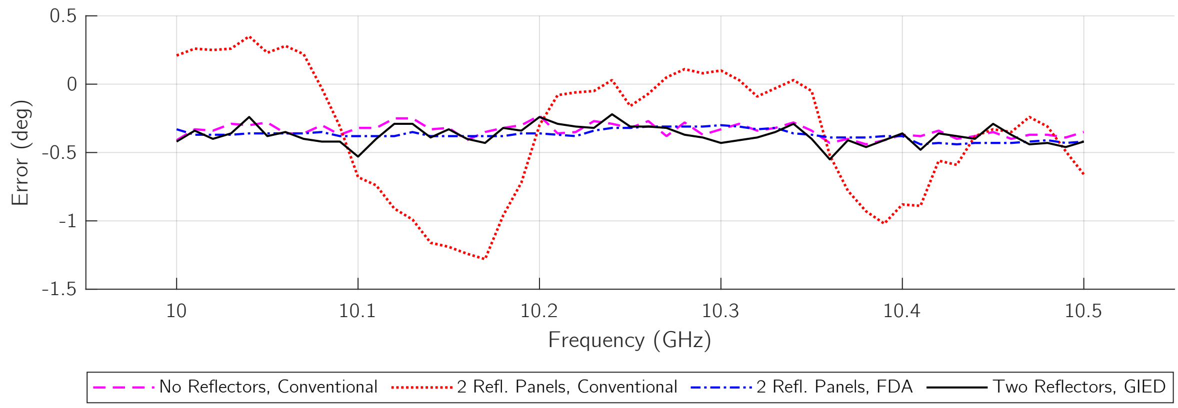

Figure 4.20: Steering angle error found from the AF pattern derived from calibrated excitation weights. Calibration was done in the single-reflector scenario.

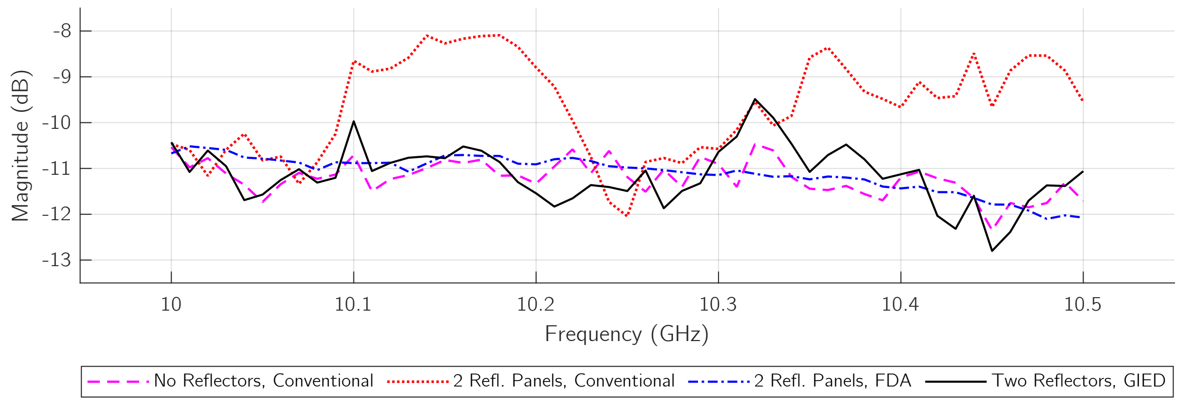

Figure 4.21: Maximum SLL found from the AF pattern derived from calibrated excitation weights. Calibration was done in the single-reflector scenario.

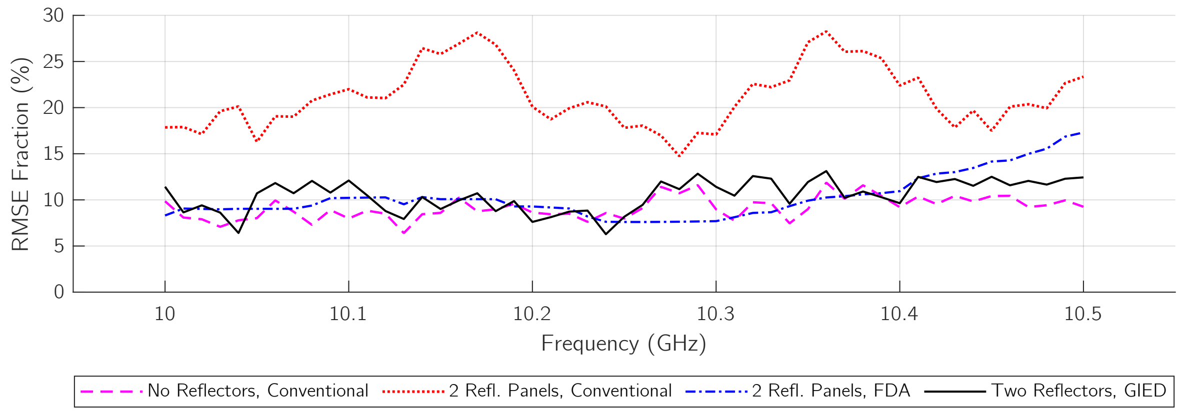

Figure 4.22: Pattern RMSE of the AF pattern derived from calibrated excitation weights. Calibration was done in the single-reflector scenario.

statistics of the calibration error are shown in Figures 4.23 and 4.24. In the plots, some guiding traces are provided. They correspond to the utilized bandwidth B, starting from the maximum bandwidth of 500 MHz on the top rightmost and decreasing incrementally by 100 MHz for each trace further down/leftwards.

The key takeaway from these plots is that the GIED method is able to achieve better calibration performance with less frequency diversity information, both in magnitude and frequency. Roughly speaking, the GIED will quickly converge to a good calibration performance (< 0.5 dB and $< 5°$ in magnitude and phase calibration weight error SD) with only 100 MHz bandwidth, before improving more slowly with added bandwidth. Meanwhile, whereas the FDA will slowly improve its performance with added bandwidth, requiring the entire 500 MHz data to achieve best performance. Clearly, **when all scattered path information is available, the GIED will obtain the best performance, including in terms of frequency information needed**.

4.5.2. Windowing

Lastly, the role of windowing for the FDA method is to be evaluated. Until now, the implemented FDA has utilized Taylor window with weights designed to produce four side lobes with SLL of -30 dB. Next, square window is used to see the effect of applying different windowing to the calibration performance. Additionally, results of the GIED method are also plotted as additional comparison, all-in-all shown in Figure 4.25. As is expected, **the application of windowing in this context provides similar trade-off behavior found in other applications of FT/IFT**. When a square window is used, the "null" which corresponds to the best calibration performance is achieved with fewer bandwidth, from 500 MHz to around 300 MHz. However, this comes at a cost of higher "ripple" as the utilized bandwidth B is increased. Meanwhile, this visualization further reaffirms the excellent bandwidth performance of the GIED method in comparison.

4.6. Chapter conclusions

In this chapter, the calibration in echoic environment problem is further elaborated. Crucially, two methods are proposed and experiments are done as proof-of-concept. The key points are summarized below.

1. Calibration in echoic environment is problematic because multiple copies of the reference signal arrives at the APAA and combine as a vector sum. For the first time, methods designed to intentionally compensate for multipath effects – dubbed echo-aware calibration – has been proposed and validated through proof-of-concept experiments.
2. The first of the two proposed methods is the FDA method. Here, the average of the frequency-domain information is taken. This process is equivalent to taking the IFT of the frequency domain signal and, conveniently, evaluating for the time domain signal at the 0-th time bin, which is the exact location of the desired LoS signal component.
3. In the GIED method, known geometry information of the echoic environment are modeled into a ray-tracing engine, which simulates the resulting multipath channel response. Through optimization, the best estimate of coefficients corresponding to each scattered path are chosen. In doing so, the best fitting multipath response can be de-embedded from the frequency diversity information to recover the excitation error of the array channels.
4. When all geometry information of scattered paths are accounted for, the GIED outperforms the FDA method. This is demonstrated in the single-reflector scenario, where GIED yields 0.363 dB and 3.19° in calibration weight error SD, while FDA yields 0.989 dB and 3.36°. That being said, both greatly improved on the multipath ridden results recorded by conventional results, with 2.088 dB and 9.85° in magnitude and phase SD. These results are further confirmed in terms of pattern-derived metrics, as

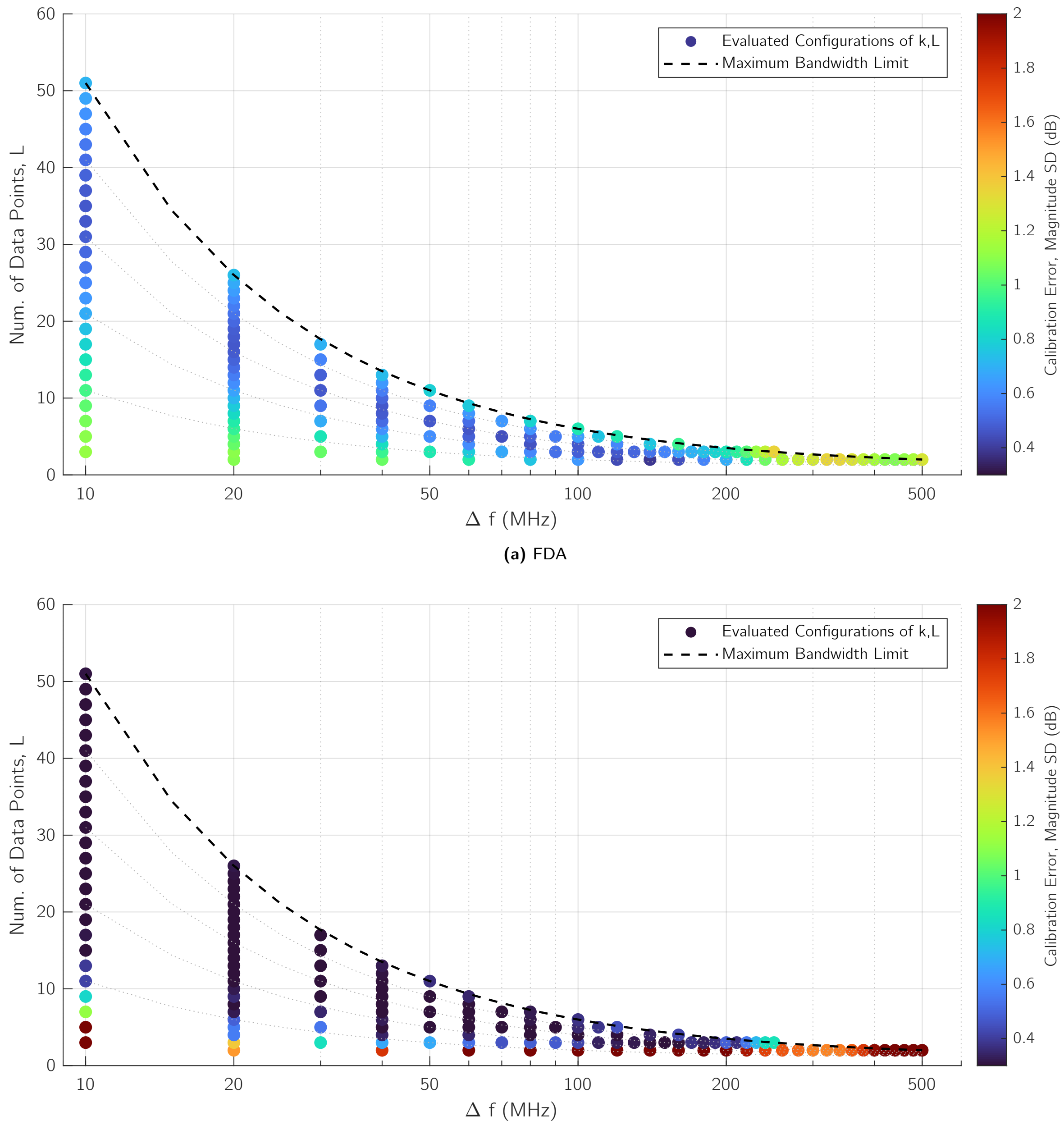

(a) FDA

(b) GIED

Figure 4.23: The SD of calibration error magnitude when the proposed methods (a) FDA and (b) GIED are applied to different configurations of frequency diversity information. The horizontal axis is shown in log-scale to improve readability.

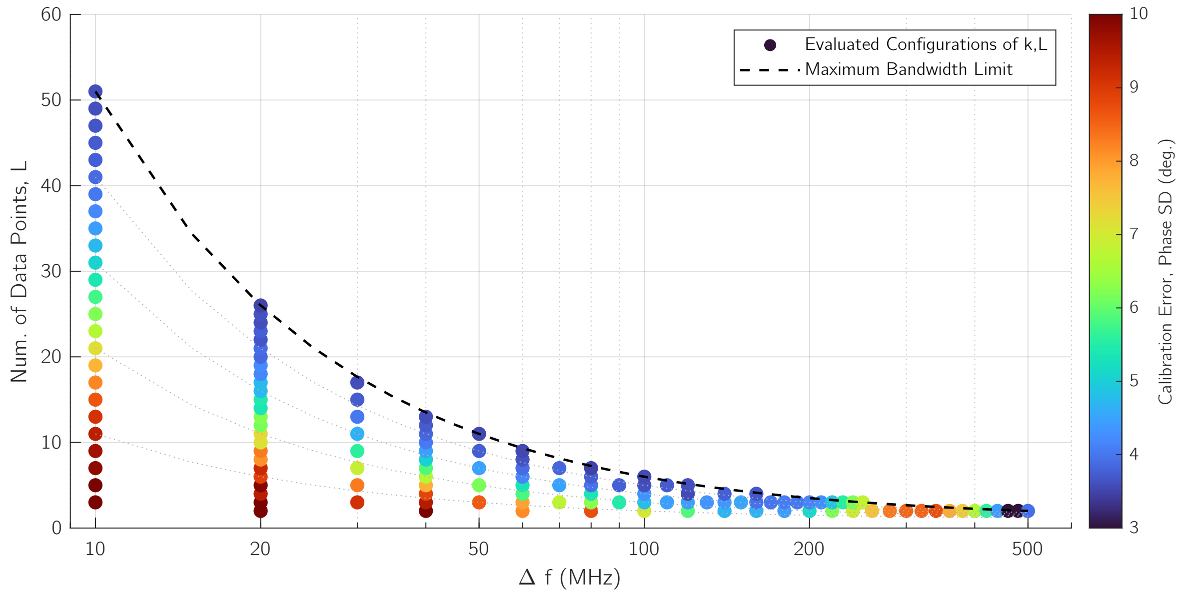

(a) FDA

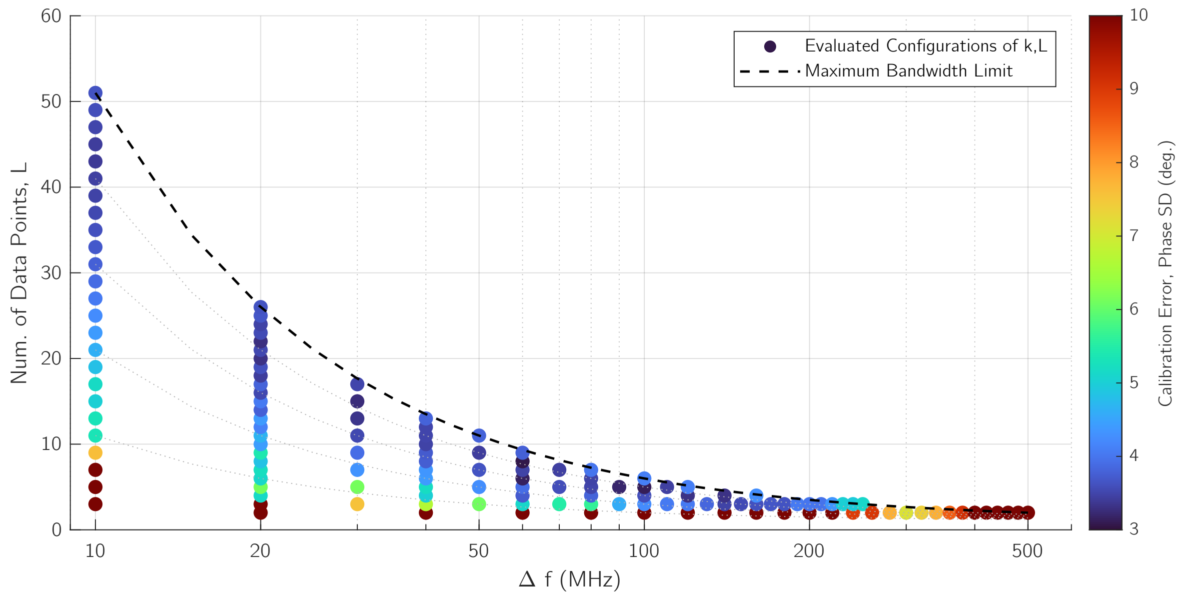

(b) GIED

Figure 4.24: The SD of calibration error phase component when the proposed methods (a) FDA and (b) GIED are applied to different configurations of frequency diversity information. The horizontal axis is shown in log-scale to improve readability.

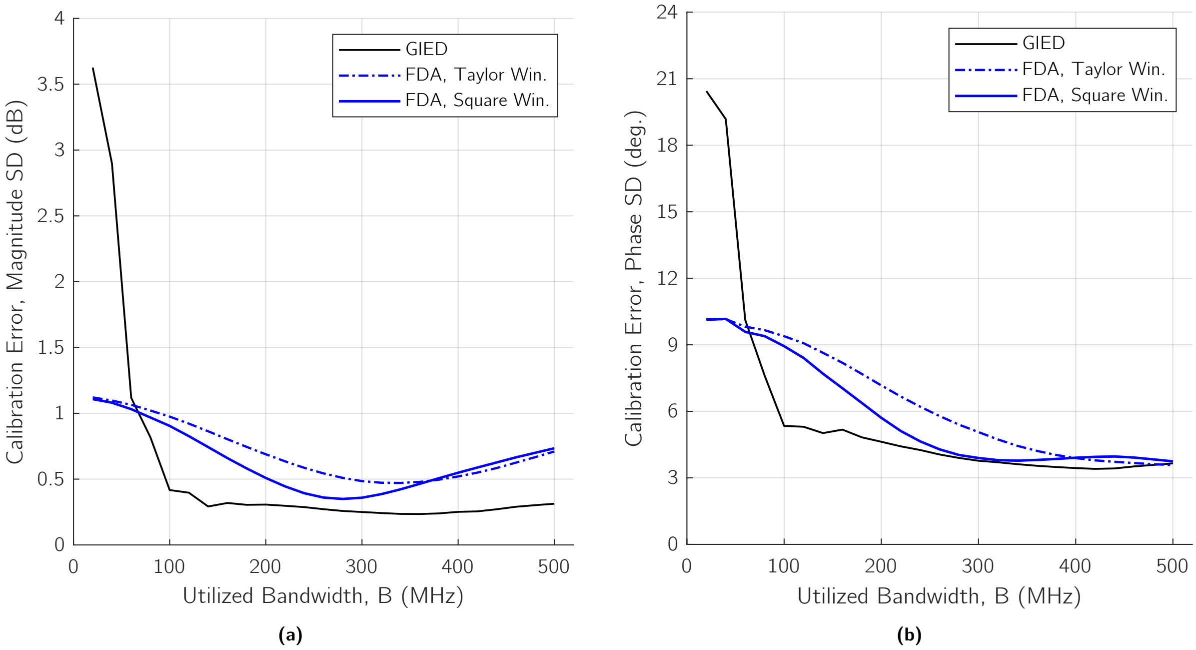

Figure 4.25: Calibration error SD for different bandwidth, with frequency resolution Δf kept constant at 10 MHz: (a) magnitude and (b) phase.

shown in Figures 4.13 - 4.15.

5. When geometry information is only partial, the FDA method is shown to be more robust to multipath effects than the GIED. In the two-reflector scenario experiments, the FDA and GIED methods demonstrate similar calibration performance in terms of calibration weights error SD: 0.998 dB and 5.92° compared to 0.592 dB and 6.22°. These values represent great improvement on the the conventional method, which obtained 2.004 dB and 13.02° of error SD in comparison. Despite these nominal descriptions, as shown in Figures 4.20 - 4.22, the FDA was able to demonstrated much better stability of pattern-derived metrics across frequencies. In contrast, the GIED demonstrates good performance in some frequencies, but vary wildly in other frequencies. This phenomena reflects the danger of forcing an optimization/fitting approach when geometry information insufficiently represent the echoic environment as a whole.

6. The GIED is demonstrated to achieve better calibration performance with less frequency diversity information. With 100 MHz in bandwidth, the GIED was able to yield better than 0.5 dB and 5° in magnitude and phase calibration weights error SD. In comparison, the FDA needs 200 and 300 MHz of bandwidth, when using square and Taylor windowing, respectively.

5 Conclusions and Recommendations for Future Work

5.1. Conclusions

This work discussed the calibration of APAA in constrained scenarios with several objectives. First, to select new metrics to quantify calibration performance. Secondly, to quantify and propose practical approaches when performing calibration with finite sampling of calibration angles and varied SNR level. Lastly, to propose methods to achieve echo-aware calibration. Key take-aways and conclusions from this thesis project is as follows.

In order to make fair comparison of calibration performance with no bias from any reference technique, pattern-derived metrics are used comprehensively for the first time, with the ideal – in this case AF – pattern is used as the ground truth. In addition to conventional beam steering metrics, such as steering angle error and maximum SLL, a more flexible and quantitative approach can be taken to evaluate the likeness of the obtained radiation pattern to the ideal, with pattern RMSE being defined and used in this work. Moreover, by switching to pattern-derived metrics, evaluation of calibration performance can be better contextualized to practical pattern characteristics, moving away from purely statistical descriptions of calibration weight errors.

To obtain optimum performance when beam steering, calibration should be done for all steering angles. However, in the interest of time, only a finite amount calibration angles can be done, which consequently dictates the span of absolute angle difference of steering angles and calibration angles $|\phi_{\text{cal}} - \phi_{\text{steer}}|$. Summary of the results can be seen in Table 5.1. As seen in the table, increases in the pattern-derived metrics are observed with increased angle difference. Despite the small numbers of these increases, without sufficient sampling of calibration angles these errors will build up. For example, if calibration is only done at broadside, a wide-angle steered beam at 50° will have around 1.5° added steering error due to insufficient calibration angles. Moreover, these added error represent only the average values, with variations possibly causing larger errors. As such, finite sampling of steering angles used for calibration should be chosen with these trade-offs in mind and contextualized by pattern-derived metrics obtained from system requirements.

When calibration is performed with varied SNR figures, a threshold-like phenomena is observed. Above this threshold, a good calibration performance is observed, although with no significant performance improvement

Table 5.1: Summary of calibration performance of different techniques under constraints.

Experiment	Metric	SCSNS	SCSLS	REV
Finite calibration angle sampling	Overall steering angle error and pattern RMSE performance	Joint best	Worst	Joint best
	Avg. increase of steering angle*	0.360°	0.341°	0.305°
	Avg. increase of pattern RMSE*	1.41%	1.67%	1.69%
Varied SNR	SNR threshold	-13.45 dB (Best)	-10.42 dB	-8.87 dB (Worst)

* Defined for each 10° increase of angle difference $|\phi_{\text{cal}} - \phi_{\text{steer}}|$.

with excess SNR. To be specific, when the SNR is above the threshold, around 20% or less pattern RMSE is observed. and maximum SLL of around -13 dB is found, which is the expected value for radiation patterns of arrays without amplitude tapering. On the other hand, the same metrics explode wildly when the calibration SNR dips below the threshold, indicating calibration failure. Since different calibration techniques demonstrate different thresholds, the robustness of each technique to noise can be ranked accordingly, as seen again in Table 5.1.

To compensate for multipath effects found in calibration in echoic environments, two "echo-aware calibration" methods are proposed. The FDA method implements an IFT and time-gating procedure by simply taking the average of the frequency information. Doing so collects the time-domain information at the 0-th time bin, corresponding to the LoS signal component. The GIED method feeds geometry information of the echoic environment to a ray-tracing simulation to estimate the multipath channel response. Through an optimization process, the best estimate of coefficients corresponding to each scattered path are chosen. In doing so, the best fitting multipath response can be de-embedded from the frequency diversity information to recover the excitation error of the array channels.

Overall, when either FDA or GIED methods are applied, the resulting calibration performance represent major improvement on the conventional method, which effectively fails under significant multipath effects. Summary of results when echo-aware calibration methods are used are shown in Table 5.2. Based on the experiments done, it was concluded that, if all relevant geometry information is known, the GIED method is the best method. This was demonstrated in the single-reflector scenario, results of which can be seen in the table. Moreover, the GIED was able to converge to a good calibration performance with much less information than the FDA, even when the window used is changed.

However, when geometry information is only partial, the FDA is the better alternative. This is because the FDA yields smooth frequency behavior, in contrast to the GIED which demonstrates some peaks in maximum SLL, as shown in 5.2. The smooth behavior of FDA is because it reuses a single calibration set for the entire calibration bandwidth. As such, the calibration performance over frequency is completely dependent on how the frequency behavior of RF channel response, i.e. excitation error $\mathbf{w}_{\text{err}}(f)$. That being said, the frequency behavior of RF components are typically smooth inside their frequency of operation. In contrast, with the GIED, if insufficient geometry information is fed, at best, the calibration will successfully compensate for the accounted scattered paths, while ignoring the rest. At worst, there is possibility of the optimization process forcing false convergence. All-in-all, selection of the optimum method hinges on several important information regarding the calibration scenario. They are presented in Table 5.3.

Table 5.2: Summary of results obtained by echo-aware calibration methods.

Experiment	**Metric**	**FDA**	**GIED**	**Conv.***
Single-reflector scenario	SD of calibration weights error, magnitude	0.989 dB	0.363 dB	2.088 dB
	SD of calibration weights error, Phase	3.36°	3.19°	9.85°
	Pattern-derived metrics (steering angle error, maximum SLL, pattern RMSE)	Good	Marginal best	Calibration fails
Single-reflector scenario, frequency diversity parameters analysis	Bandwidth needed to get < 0.5 dB and 5° in magnitude and phase SD of calibration weights error	$>$ 200 MHz, depends on window	100 MHz	-
Two-reflector scenario	SD of calibration weights error, magnitude	0.998 dB	0.592 dB	2.004 dB
	SD of calibration weights error, Phase	5.92°	6.22°	13.02°
	Steering angle error	Around -0.4°	Around -0.4°	Swerves across frequencies
	Maximum SLL	Smooth, always under -10.5 dB	Varies, with peaks up to -9.5 dB	Calibration fails
	Pattern RMSE	Smooth, but worsen to 17% at higher frequencies	Sharp variations, but below 14%	Calibration fails

* Conventional, i.e. the SCSNS technique without compensation for multipath effects.

Table 5.3: Summary of how different aspects of the calibration scenario affects performance of the proposed echo-aware calibration methods.

Aspect	FDA	GIED
Geometry/scattered paths	Does not utilize geometry information.	Will only compensate scattered paths accounted by fed the geometry information.
Frequency information	Calibration performance hinges on the amount of frequency information.	Requires significantly less frequency information to converge.
Frequency behavior of RF channel/excitation error	Perform better when behavior is smooth and relatively static over frequency	Agnostic as long as modeled well in the cost function.

5.2. Recommendations for Future Work

From Section 3.2, it has been demonstrated that by performing calibration at a given steering angle, better steered beam metrics are obtained, i.e. steering angle error. However, it would be interesting to extend the question for more complex beam shapes. For example, when the placing of nulls are important in the intended beam shape, does performing calibration in that angle yield better results. What of flat-top beam patterns, or multi-beam patterns? Ultimately, when considering these different patterns, is adapting the calibration procedure worth the time-performance trade-off?

Still on the topic of calibration angle, the possibility of smart interpolation techniques is worth exploring. In doing so, the number of measurements done to achieve optimum calibration at multiple steering angles can represented by a subset of measurements.

In Chapter 4, pattern-derived metrics were synthesized through AF patterns, derived from calibration weights information. In doing so, simplification of the inter-subarray calibration is applied Equations 4.51 -4.53. Measurements must be done to validate these simulated results when applied to a physical APAA.

As significant disadvantage to the GIED is the fact that geometry information must be manually input as objects in the ray-tracing engine. Not only inference of this information difficult to obtain manually, such an approach will only work in a static calibration environment. As such, a joint sensing-calibration problem arise. To overcome this, an iterative approach can be explored. The FDA, which requires no geometry information, can be used as to obtain the initial calibration weights.

Furthermore, a natural progression to echo-aware calibration is echo-enhanced calibration. That is to say, calibration that not only compensate, but utilize scattered paths to their advantage. For example, scattered pathh signal components can be used to increase the overall calibration SNR as spatial diversity, or as an additional calibration angle.

References

[1] A. J. Fenn, D. H. Temme, W. P. Delaney, and W. E. Courtney, "The development of phased-array radar technology," *Lincoln Laboratory Journal*, vol. 12, no. 2, pp. 321–430, 2000.

[2] K. Temir, M. S. Akyüz, and Y. K. Alp, "Consideration of environmental and functional factors in calibration of antenna integrated active phased array transmitters," in *2016 IEEE International Symposium on Phased Array Systems and Technology (PAST)*, 2016, pp. 1–5. DOI: 10.1109/ARRAY.2016.7832558.

[3] V. Lakshminarayanan and N. Sriraam, "The effect of temperature on the reliability of electronic components," in *2014 IEEE International Conference on Electronics, Computing and Communication Technologies (CONECCT)*, 2014, pp. 1–6. DOI: 10.1109/CONECCT.2014.6740182.

[4] K. Kibaroglu, M. Sayginer, T. Phelps, and G. M. Rebeiz, "A 64-element 28-ghz phased-array transceiver with 52-dbm eirp and 8–12-gb/s 5g link at 300 meters without any calibration," *IEEE Transactions on Microwave Theory and Techniques*, vol. 66, no. 12, pp. 5796–5811, 2018. DOI: 10.1109/TMTT.2018.2854174.

[5] R. X. F. Budé, K. A. P. van Hastenberg, U. Johannsen, and A. B. Smolders, "Near-field calibration methods for integrated analog beamforming arrays and focal plane array feeds," English, *IEEE Open Journal of Antennas and Propagation*, vol. 4, pp. 860–870, 2023, ISSN: 2637-6431. DOI: 10.1109/OJAP.2023.3304371.

[6] Y. Aslan, P. Aubry, N. B. Onat, J. Janssen, M. Geurts, and A. Yarovoy, "Heuristic over-the-air calibration of beamformer ics in active mm-wave phased arrays," in *2023 IEEE Conference on Antenna Measurements and Applications (CAMA)*, 2023, pp. 840–845. DOI: 10.1109/CAMA57522.2023.10352655.

[7] D. Schvartzman, J. D. D. Díaz, D. Zrnić, M. Herndon, M. B. Yeary, and R. D. Palmer, "Holographic back-projection method for calibration of fully digital polarimetric phased array radar," *IEEE Transactions on Radar Systems*, vol. 1, pp. 295–307, 2023. DOI: 10.1109/TRS.2023.3286849.

[8] R. M. Lebrón, P.-S. Tsai, J. M. Emmett, C. Fulton, and J. L. Salazar-Cerreno, "Validation and testing of initial and in-situ mutual coupling-based calibration of a dual-polarized active phased array antenna," *IEEE Access*, vol. 8, pp. 78 315–78 329, 2020. DOI: 10.1109/ACCESS.2020.2983523.

[9] A. Nafe, K. Kibaroglu, M. Sayginer, and G. M. Rebeiz, "An in-situ self-test and self-calibration technique utilizing antenna mutual coupling for 5g multi-beam trx phased arrays," in *2019 IEEE MTT-S International Microwave Symposium (IMS)*, 2019, pp. 1229–1232. DOI: 10.1109/MWSYM.2019.8701072.

[10] A. Nafe, A. H. Aljuhani, K. Kibaroglu, M. Sayginer, and G. M. Rebeiz, "In-situ self-test and self-calibration of dual-polarized 5g trx phased arrays leveraging orthogonal-polarization antenna couplings," in *2020 IEEE/MTT-S International Microwave Symposium (IMS)*, 2020, pp. 1081–1084. DOI: 10.1109/IMS30576.2020.9224039.

[11] E. Lier, M. Zemlyansky, D. Purdy, and D. Farina, "Phased array calibration and characterization based on orthogonal coding: Theory and experimental validation," in *2010 IEEE International Symposium on Phased Array Systems and Technology*, 2010, pp. 271–278. DOI: 10.1109/ARRAY.2010.5613357.

[12] T. Phelps, Z. Zhang, and G. Rebeiz, "Simultaneous channel phased-array calibration using orthogonal codes and post-coding," in *2021 IEEE MTT-S International Microwave Symposium (IMS)*, 2021, pp. 397–399. DOI: 10.1109/IMS19712.2021.9575031.

[13] R. Long, J. Ouyang, F. Yang, W. Han, and L. Zhou, "Multi-element phased array calibration method by solving linear equations," *IEEE Transactions on Antennas and Propagation*, vol. 65, no. 6, pp. 2931–2939, 2017. DOI: 10.1109/TAP.2017.2694767.

[14] F. Zhang, W. Fan, Z. Wang, Y. Zhang, and G. F. Pedersen, "Improved over-the-air phased array calibration based on measured complex array signals," *IEEE Antennas and Wireless Propagation Letters*, vol. 18, no. 6, pp. 1174–1178, 2019. DOI: 10.1109/LAWP.2019.2911725.

[15] S. Tang, Z. Wang, C. Pan, R. Su, W. Fan, and S. Gao, "A fast and efficient calibration method for phased array antennas using fourier-structured excitation matrix," *IEEE Transactions on Antennas and Propagation*, vol. 71, no. 3, pp. 2290–2299, 2023. DOI: 10.1109/TAP.2023.3234814.

[16] Z. Wang, F. Zhang, H. Gao, O. Franek, G. F. Pedersen, and W. Fan, "Over-the-air array calibration of mmwave phased array in beam-steering mode based on measured complex signals," *IEEE Transactions on Antennas and Propagation*, vol. 69, no. 11, pp. 7876–7888, 2021. DOI: 10.1109/TAP.2021.3076349.

[17] S. Mano and T. Katagi, "A method for measuring amplitude and phase of each radiating element of a phased array antenna," *Electronics and Communications in Japan (Part I: Communications)*, vol. 65, no. 5, pp. 58–64, 1982. DOI: https://doi-org.tudelft.idm.oclc.org/10.1002/ecja.4410650508. eprint: https://onlinelibrary-wiley-com.tudelft.idm.oclc.org/doi/pdf/10.1002/ecja.4410650508. [Online]. Available: https://onlinelibrary-wiley-com.tudelft.idm.oclc.org/doi/abs/10.1002/ecja.4410650508.

[18] R. Sorace, "Phased array calibration," *IEEE Transactions on Antennas and Propagation*, vol. 49, no. 4, pp. 517–525, 2001. DOI: 10.1109/8.923310.

[19] R. Long, J. Ouyang, F. Yang, W. Han, and L. Zhou, "Fast amplitude-only measurement method for phased array calibration," *IEEE Transactions on Antennas and Propagation*, vol. 65, no. 4, pp. 1815–1822, 2017. DOI: 10.1109/TAP.2016.2629467.

[20] G. He, X. Gao, and H. Zhou, "Fast phased array calibration by power-only measurements twice for each antenna element," *International Journal of Antennas and Propagation*, vol. 2019, no. 1, p. 6 432 149, 2019. DOI: https://doi.org/10.1155/2019/6432149. eprint: https://onlinelibrary.wiley.com/doi/pdf/10.1155/2019/6432149. [Online]. Available: https://onlinelibrary.wiley.com/doi/abs/10.1155/2019/6432149.

[21] T. Takahashi, Y. Konishi, S. Makino, H. Ohmine, and H. Nakaguro, "Fast measurement technique for phased array calibration," *IEEE Transactions on Antennas and Propagation*, vol. 56, no. 7, pp. 1888–1899, 2008. DOI: 10.1109/TAP.2008.924682.

[22] T. Takahashi, Y. Konishi, and I. Chiba, "A novel amplitude-only measurement method to determine element fields in phased arrays," *IEEE Transactions on Antennas and Propagation*, vol. 60, no. 7, pp. 3222–3230, 2012. DOI: 10.1109/TAP.2012.2196961.

[23] H.-J. Yoon and B.-W. Min, "Improved rotating-element electric-field vector method for fast far-field phased array calibration," *IEEE Transactions on Antennas and Propagation*, vol. 69, no. 11, pp. 8021–8026, 2021. DOI: 10.1109/TAP.2021.3083796.

[24] S. Li, Z. Yu, Q. Zhang, and Y. Luo, "An improved power-only measurement strategy for calibrating phased array antennas," *International Journal of Antennas and Propagation*, vol. 2022, no. 1, p. 4 696 818, 2022. DOI: https://doi.org/10.1155/2022/4696818. eprint: https://onlinelibrary.wiley.com/doi/pdf/10.1155/2022/4696818. [Online]. Available: https://onlinelibrary.wiley.com/doi/abs/10.1155/2022/4696818.

[25] W. Fan, Y. Zhang, Z. Wang, and F. Zhang, "Large-scale phased array calibration based on amplitude-only measurement with the multiround grouped-rev method," *IEEE Transactions on Antennas and Propagation*, vol. 72, no. 1, pp. 454–465, 2024. DOI: 10.1109/TAP.2023.3333387.

[26] Z. Sarayloo, N. Masoumi, H. Shahi, E. H. Mirza Alian, S. S. Naeini, and M. N. Ahmadabadi, "A convolutional neural network approach for phased array calibration using power-only measurements," in *2020 28th Iranian Conference on Electrical Engineering (ICEE)*, 2020, pp. 1–6. DOI: 10.1109/ICEE50131.2020.9260769.

[27] S. Li, K. Liu, Y. Xie, *et al.*, "Phased array calibration based on fast rotating-element harmonic electric-field vector," *IEEE Transactions on Microwave Theory and Techniques*, vol. 74, no. 3, pp. 2599–2611, 2026. DOI: 10.1109/TMTT.2025.3645081.

[28] W. Qi, T. Feng, F. Tian, *et al.*, "Calibrating the phased array antenna in a reverberation chamber," *IEEE Transactions on Instrumentation and Measurement*, vol. 74, pp. 1–6, 2025. DOI: 10.1109/TIM.2024.3497161.

[29] "Phaser (CN0566) control with MATLAB." (2023), [Online]. Available: https://github.com/mathworks/Phaser-Control-with-MATLAB/tree/main.

[30] J. Kraft, *Adalm-phaser (cn0566) phased array exploration platform*. [Online]. Available: https://wiki.analog.com/resources/eval/user-guides/circuits-from-the-lab/cn0566 (visited on 03/27/2026).

[31] *Cn0566*. [Online]. Available: https://www.analog.com/en/resources/reference-designs/circuits-from-the-lab/cn0566.html#rd-overview (visited on 03/27/2026).

A

Photographs of Measurement Setups

Figure A.1: Photograph of the measurement setup to investigate the effects of performing calibration in an echoic environment, taken in one of the Radar Labs of the Electrical Engineering, Mathematics and Computer Science (EEMCS) building. The DUT is placed on the edge of a table. Without the use of a specialized antenna platform, the measurement procedure relies on manual positioning of the HB100 module to implement the azimuth angles, ϕ_{cal}. Moreover, a small panel of RF absorber can be seen on the floor halfway between the DUT and the beacon. This is done as an effort to suppress the scattered path due to the floor reflection.

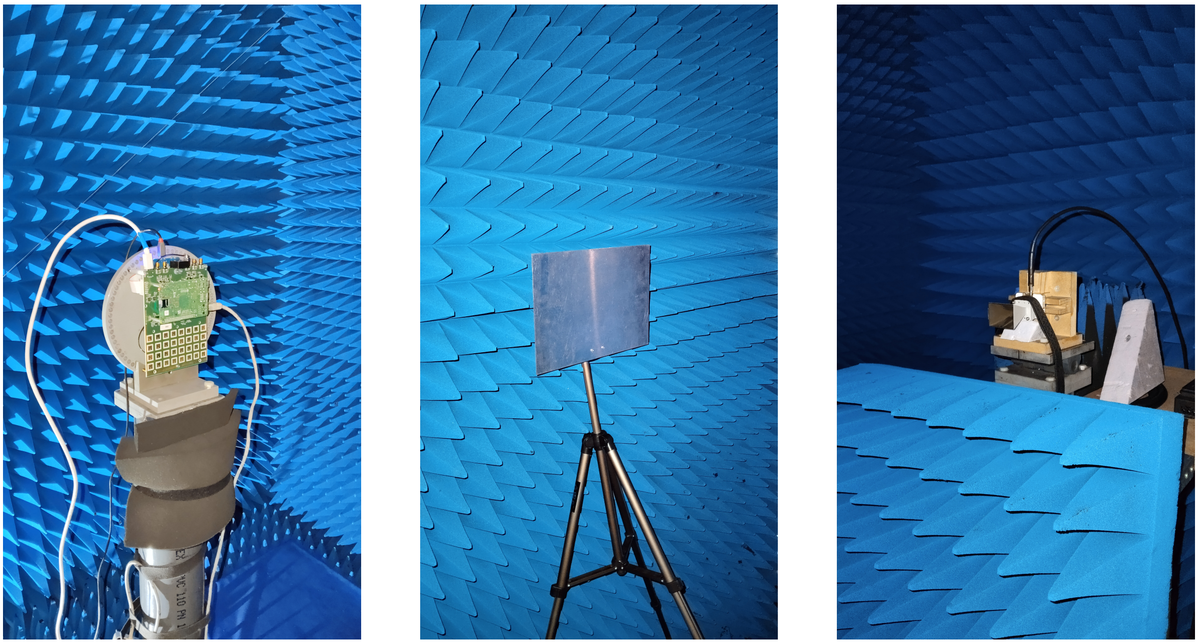

(a) **(b)** **(c)**

Figure A.2: Photographs taken from the proof-of-concept experiment for the reference and single-reflector scenario, done in the Delft University Chamber for Antenna Tests (DUCAT): (a) horn antenna, acting as the calibration beacon; (b) the metal reflector panel placed for the single-reflector scenario, thereby introducing a scattered path; (c) the DUT, fixed on a antenna platform.

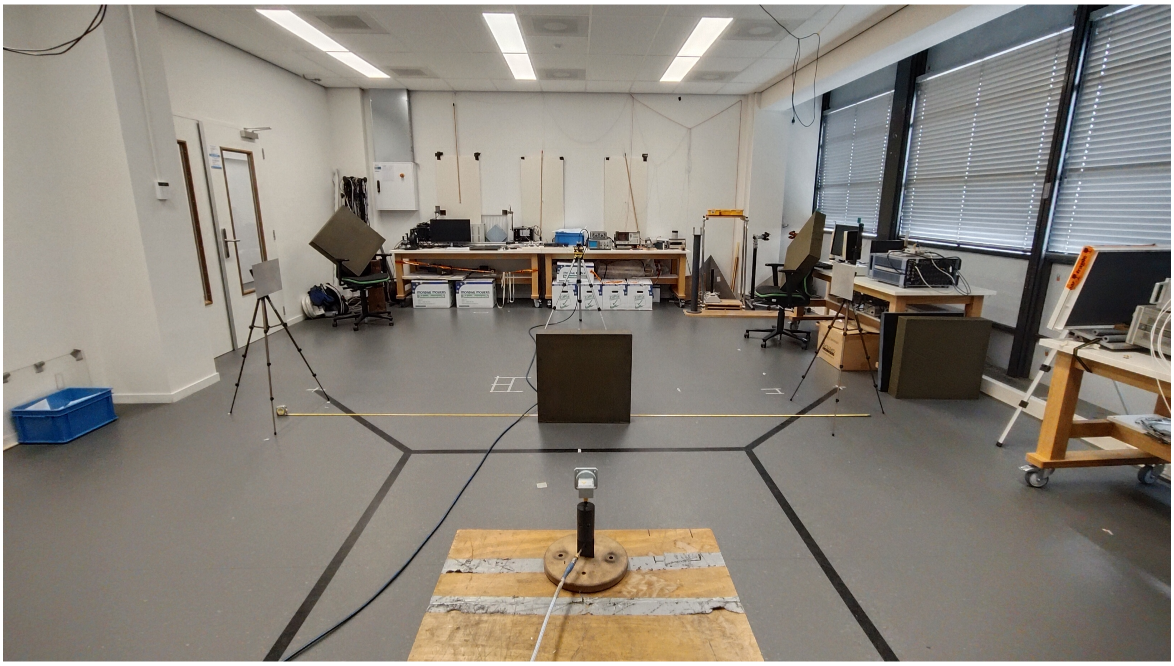

(a)

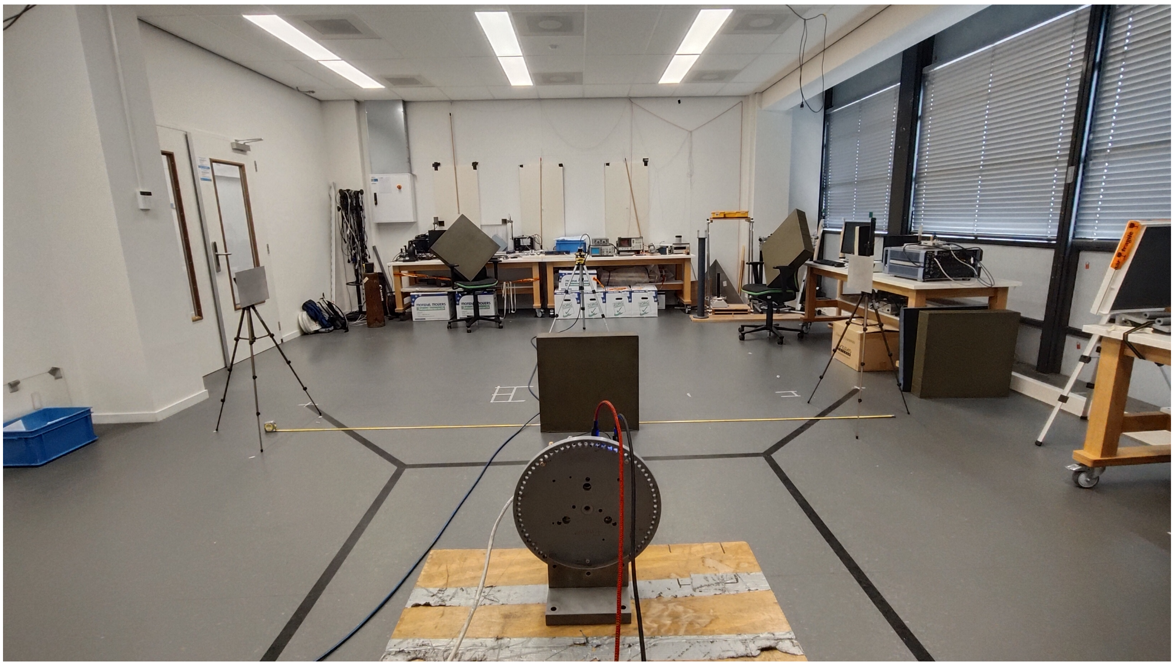

(b)

Figure A.3: Photographs taken from the proof-of-concept experiment for the two-reflector scenario, done in one of the Radar Labs of the EEMCS building: (a) PDP measurement, taken from the perspective of the surrogate antenna; (b) frequency diversity measurement, taken from the perspective of the DUT. The horn antenna, acting as the calibration beacon, is visible in the far side of the room. The two metal reflector panels can be seen to the sides of the room. An RF absorber panel can be seen set on the floor, just under the LoS path between the beacon and the surrogate antenna/DUT, to remove the scattered path due to the floor.